

Electronic Thesis and Dissertation Repository

12-11-2020 10:30 AM

Finite Element Analyses and Random Field Modeling of Naturally Corroded Underground Energy Pipelines

Ji Bao, *The University of Western Ontario*

Supervisor: Wenxing, Zhou, *The University of Western Ontario*

A thesis submitted in partial fulfillment of the requirements for the Doctor of Philosophy degree in Civil and Environmental Engineering

© Ji Bao 2020

Follow this and additional works at: <https://ir.lib.uwo.ca/etd>



Part of the [Civil Engineering Commons](#), and the [Structural Engineering Commons](#)

Recommended Citation

Bao, Ji, "Finite Element Analyses and Random Field Modeling of Naturally Corroded Underground Energy Pipelines" (2020). *Electronic Thesis and Dissertation Repository*. 7486.

<https://ir.lib.uwo.ca/etd/7486>

This Dissertation/Thesis is brought to you for free and open access by Scholarship@Western. It has been accepted for inclusion in Electronic Thesis and Dissertation Repository by an authorized administrator of Scholarship@Western. For more information, please contact wlsadmin@uwo.ca.

Abstract

Metal-loss corrosion is one of the major threats to the integrity of oil and natural gas pipelines. The Fitness-For-Service (FFS) assessment is commonly carried out to demonstrate the integrity of the corroded pipelines. Due to the geometric complexity of the natural corrosions, the research of FFS assessment in the previous studies always employed the pipe segments containing artificially induced corrosion features. However, since artificial features are in general regular-shaped, they do not capture geometric characteristics of naturally occurring corrosions. The thesis develops a finite element model and a random field based corrosion model to deal with five issues regarding the FFS assessment of pipe segments containing naturally occurring corrosion features.

The first study develops a three-dimensional finite element model to simulate the full-scale burst tests of pipe segments containing real corrosion features. The finite element model, as well as the RSTRENG model, is used to study the impact of the depth threshold and five commonly used interaction rules on the burst capacity predictions of naturally corroded pipe segments.

The second study investigates the impact of corrosion anomaly classes on the predictive accuracy of the B31G, B31G-M, Shell92, PCORRC, PCORRC-M, CSA and RSTRENG models for pin hole, axial slotting, axial grooving, circumferential slotting, circumferential grooving, pitting and general corrosion anomalies. The finite element analyses (FEA) results are used as the benchmark to evaluate the accuracies of the 7 burst capacity models for different classes of anomalies.

The third study proposed a modified RSTRENG (RSTRENG-M) model to evaluate the burst capacity of corroded pipelines by employing the riverbed profile of corrosion features. Based on 60 full-scale burst tests results, RSTRENG-M is shown to be more accurate than the RSTRENG model and comparable to the Psqr model in terms of accuracy but more advantageous in terms of computational efficiency.

The fourth study proposes a random field model to characterize the corrosion depth on the external surface of buried oil and gas pipelines. The model addresses the intermingling of corroded and corrosion-free areas on the pipe surface by using a latent homogeneous Gaussian random field and a spatial position-dependent threshold associated with the latent Gaussian field. A comparison of simulated and measured corrosion fields suggests that the proposed model is able to capture the characteristics of naturally-occurring corrosion field on the pipe surface.

The fifth study combines the FEA model developed in the second study with the random field-based corrosion model presented in the fourth study to analyze the simulated naturally occurring corrosion features (i.e. synthetic corrosion features) in large quantity to further validate the RSTRENG-M model.

Keywords

Underground pipeline, naturally occurring corrosion features, finite element analysis, random field analysis, interaction rule, corrosion anomaly class

Summary for Lay Audience

Pipeline is the most common mode for the natural gas and oil transportation. The external corrosion is one of the leading causes of the pipeline incidents. The safe operation of corroded pipelines is assured by the Fitness-for-service (FFS) assessment. To assist with the research of the FFS assessment of corroded pipelines, this thesis develops a random field-based model to simulate and a finite element analysis (FEA) model to analyze the naturally corroded pipelines.

The pipeline companies usually run inline inspection (ILI) tools to detect and size the corrosion anomalies on underground pipelines. The ILI tools report the corrosion anomalies deeper than the reporting threshold and classify the anomalies into different classes based on the geometries of anomalies, followed by grouping the corrosion anomalies into corrosion clusters using interaction rules. The burst capacities of corrosion clusters are predicted using the semi-empirical burst models, such as the ASME B31G and RSTRENG, for the subsequent mitigation decisions. This thesis investigates the impact of reporting depth thresholds and interaction rules on the burst capacity evaluation with the developed FEA model and the RSTRENG model. Besides, the effects of the corrosion anomaly class on the predictive accuracies of several commonly used semi empirical models are also investigated to facilitate the pipeline engineers to select the most suitable models for the burst capacity evaluation of corrosion anomalies.

Since all the existing semi-empirical models are associated with considerable errors, this study proposes a modified RSTRENG model (RSTRENG-M) to improve the predictive accuracy of the semi-empirical models. However, due to the high cost of obtaining the naturally corroded pipe segments, the number of pipe segments used to validate the RSTRENG-M model is limited. Hence, this study develops a random field-based corrosion model to simulate the external corrosion surfaces of the naturally corroded pipelines, which is capable of capturing the main characteristics of naturally corroded pipeline surfaces. By combining FEA with the random field-based corrosion model, the full scale burst tests of naturally occurring corrosion features are analyzed in large quantity to further validate the RSTRENG-M model.

Co-Authorship Statement

A version of Chapter 2, co-authored by Ji Bao and Wenxing Zhou is under review for possible publication in *Journal of Pipeline Science and Engineering* (revision requested).

A version of Chapter 3, co-authored by Ji Bao and Wenxing Zhou has been published in *International Journal of Geosynthetics and Ground Engineering*. 6(45). DOI: <https://doi.org/10.1007/s40891-020-00227-w>.

A version of Chapter 5, co-authored by Ji Bao and Wenxing Zhou is under review for possible publication in *Structural Safety* (revision requested).

Dedication

To my wife, parents and Tuffy who made me stronger

Acknowledgments

Throughout the writing of this dissertation, I have received a great deal of support and assistance.

First, I wish to express my sincere gratitude to my supervisor, Dr. Wenxing Zhou, for his continuous support during my Ph.D. study. His profound knowledge, versatility on different research areas and excellent writing skills inspired me to grow as a researcher. Not to mention, I was always impressed by his dedication and seriousness towards his work. His open-door policy helped me in all the time of my research and writing of the thesis; His insightful feedback brought my work to higher levels. This thesis would have not been finished without his persistent help.

I would like to thank Dr. Shenwei Zhang from TC Energy for his valuable data on my research. I would also like to extend my appreciation to members of my thesis examination committee for their advice and critical assessment on my thesis. I gratefully acknowledge the financial support provided by the Natural Sciences and Engineering Research Council of Canada (NSERC) and TC Energy Corporation.

My sincere thanks also go to Cheng Qian, Tammeeen Siraj, Changqing Gong, Wei Xiang, Shulong Zhang and all the colleagues of our research group for their encouragement and supports to help me go through all the ups and downs in my Ph.D. career.

Finally, I would like to thank my wife, who has always inspired me to give my best efforts and debugged my MATLAB algorithms. I am thankful to her for always being by my side.

Table of Contents

Abstract.....	ii
Summary for Lay Audience.....	iv
Co-Authorship Statement.....	v
Acknowledgments.....	vii
Table of Contents.....	viii
List of Tables.....	xii
List of Figures.....	xiv
List of Appendices.....	xviii
List of Abbreviations and Symbols.....	xix
1 Introduction.....	1
1.1 Background.....	1
1.2 Objective.....	8
1.3 Scope of the study.....	9
1.4 Thesis format.....	10
References.....	11
2 Influence of Depth Thresholds and Interaction Rules on the Burst Capacity Evaluation of Naturally Corroded Pipelines.....	14
2.1 Introduction.....	14
2.2 Naturally corroded pipe specimens.....	16
2.3 Corrosion anomaly and cluster identification.....	18
2.3.1 Anomaly identification with different depth thresholds.....	18
2.3.2 Interaction rules.....	19
2.4 Methodologies.....	20
2.4.1 General.....	20
2.4.2 FEA model.....	21

2.4.3	FEA validation	24
2.4.4	RSTRENG model	25
2.5	Results and Discussions	26
2.5.1	Impact of depth threshold	26
2.5.2	Impact of interaction rules	28
2.6	Conclusion	35
	References	35
3	Influence of the Corrosion Anomaly Class on Predictive Accuracy of Burst Capacity Models for Corroded Pipelines	38
3.1	Introduction.....	38
3.2	Burst capacity models	42
3.3	Corroded pipe specimens	44
3.4	Finite element analysis.....	47
3.4.1	FEA model	47
3.4.2	Validation of FEA model.....	48
3.5	Influence of anomaly classification on the accuracy of burst capacity models....	53
3.6	Conclusions.....	57
	References	57
4	A Modified RSTRENG Model for Evaluating the Burst Capacity of Corroded Pipelines	61
4.1	Introduction.....	61
4.2	RSTRENG and effective area.....	64
4.3	Full scale burst tests	65
4.4	RSTRENG-M model	69
4.4.1	Model description	69
4.4.2	Model validation	71
4.4.3	Impact of resolution of riverbed profile.....	74

4.5	Application to inline inspection data	75
4.6	Conclusion	81
	References	82
5	A Random Field Model of External Metal-loss Corrosion on Buried Pipelines	84
5.1	Introduction.....	84
5.2	Literature review	86
5.3	Corrosion measurement data.....	87
5.4	Random field model of corrosion on pipelines.....	89
5.4.1	Fundamentals	89
5.4.2	Parameter estimation.....	93
5.4.3	Simulated corrosion on pipe surface.....	98
5.4.4	Impact of correlation length.....	104
5.5	Conclusion	106
	References	106
6	Predictive Accuracy Investigation of Burst Models for Corroded Pipelines Using Finite Element Analysis and Random Field-based Corrosion Simulation Model	110
6.1	Introduction.....	110
6.2	Semi-empirical burst capacity models for corroded pipelines.....	112
6.2.1	DNV model.....	113
6.2.2	CPS model	115
6.2.3	Psqr model	116
6.3	Generation and FEA of synthetic corrosion features	117
6.3.1	Generation of synthetic corrosion features	117
6.3.2	FEA of synthetic corrosion clusters	120
6.4	Investigation of the predictive accuracy based on FEA results	121
6.5	Conclusions.....	126

References	127
7 Summary, Conclusions and Recommendations for Future Study	130
7.1 General	130
7.2 Influence of depth threshold and interaction rule on the burst capacity evaluation of naturally corroded pipelines by using FEA and RSTRENG model	130
7.3 Impact of corrosion anomaly class on the predictive accuracy of burst capacity models for corroded pipelines.....	131
7.4 A modified RSTRENG model to predict the burst capacity for corroded pipelines	131
7.5 A random field model to simulate the naturally corroded external surface of buried pipelines	132
7.6 Predictive accuracy investigation of burst models for corroded pipelines based on FEA of synthetic corrosion features generated by the random field-based corrosion model	133
7.7 Research significance and novelty.....	134
7.8 Recommendations for future study	135
Appendices.....	137
Curriculum Vitae	143

List of Tables

Table 1.1 Definitions of the shape idealizations, SF, flow stress and the bulging factors for different models	5
Table 2.1 Summary of 14 naturally corroded test specimens (Zhang et al. 2018)	17
Table 2.2 Interaction limits for five commonly used interaction rules.....	20
Table 2.3 Impact of the depth threshold on the predicted burst capacity based on FEA.....	27
Table 2.4 Impact of the depth threshold on the predicted burst capacity based on the RSTRENG	28
Table 2.5 Impact of the interaction rule on the FEA-predicted burst capacities	32
Table 2.6 Impact of the interaction rule on the RSTRENG-predicted burst capacities.....	33
Table 3.1 POF classification criteria for corrosion anomalies.....	40
Table 3.2 Summary of the 16 test specimens in Zhang et al. (2018, 2020).....	46
Table 3.3 Number of individual anomalies in different POF classes identified on the 16 pipe specimens	46
Table 3.4 Geometric characteristics of the critical corrosion clusters on 16 specimens in Zhang et al. (2018, 2020).....	50
Table 3.5 Geometric characteristics of 14 specimens and the critical corrosion clusters on the 14 specimens in Chouchaoui (1993).....	50
Table 3.6 Statistics of the FEA-to-model predicted burst capacity ratios for different classes of corrosion anomalies	56
Table 4.1 Summary of full-scale burst test data collected in the present study.....	68
Table 4.2 Mean and COV of Test-to-predicted ratios for different burst test datasets.....	74

Table 4.3 Impact of riverbed resolution on the RSTRENG-M model in terms of naturally occurring and artificial corrosion features	75
Table 4.4 Mean and COV of Test-to-predicted ratios for 14 specimens containing naturally occurring corrosion features in the context of ILI data.....	78
Table 5.1 Relevant information of the pipe segments in the analysis	88
Table 5.2 Parameters of the random field corrosion model for the five pipe segments	96
Table 5.3 Comparison between the numbers of corrosion anomalies and clusters contained in the simulated and measured fields of segment #1 and #2.....	101
Table 6.1 The ranges of the model parameters for the random field corrosion model presented in Chapter 5	118
Table 6.2 Summary of the material and geometrical properties of the corrosion clusters simulated in this study	119
Table 6.3 Summary of the basic statistics of the FEA-to-predicted ratios of corrosion clusters on the pipe segments made by different materials.....	124
Table C.1 Values of c_{ij} in Eq. (C.1)	142

List of Figures

Figure 1.1 Corrosion anomaly identification by ILI tools	2
Figure 1.2 Illustration of typical ILI results.....	3
Figure 1.3 Illustration of a naturally occurring corrosion anomaly on the pipe segment.....	7
Figure 2.1 2D and 3D images of the scanned surface of specimen 16-1	18
Figure 2.2 Corrosion anomalies on specimen 16-1 after applying the different depth thresholds	19
Figure 2.3 Illustration of the interaction rule and interaction limits	20
Figure 2.4 Comparison between the actual true stress - strain curves with the fitted ones for specimens 16-1 and 24-1	22
Figure 2.5 Finite element generation strategy in the corrosion region	23
Figure 2.6 FEA model of pipe segment containing the scan surface of specimen 16-1.....	24
Figure 2.7 Comparison between the test-based and FEA-predicted burst capacities of the 14 specimens	25
Figure 2.8 Illustration of the river bottom path and river bottom profile of a naturally occurring corrosion feature	26
Figure 2.9 Corroded areas on specimen 16-1 and critical corrosion clusters identified based on different interaction rules.....	29
Figure 2.10 Distribution of longitudinal and circumferential separation distances between interacting corrosion anomalies in CA1 in terms of different interaction rules	31
Figure 3.1 Illustration of a naturally occurring corrosion anomaly on a corroded pipeline ...	40
Figure 3.2 Scanned surface and representative corrosion anomalies on specimen 16-1	45

Figure 3.3 Lengths and widths of the 897 corrosion anomalies collected in the present study	47
Figure 3.4 True stress σ - true strain ε curves for specimens 16-1 and 30-1	48
Figure 3.5 Illustration of the $1 \text{ in} \times 6t$ interaction rule.....	49
Figure 3.6 Two representative FEA models of corrosion clusters on specimens 16-1 and S1CC	51
Figure 3.7 Comparison between the test-based and FEA-based burst capacities.....	52
Figure 3.8 Comparison between the FEA and predicted burst capacities in terms of different semi-empirical models and corrosion anomaly classes	56
Figure 4.1 Illustration of a corrosion cluster, river-bottom path and river-bottom profile.....	61
Figure 4.2 Illustration of the river-bottom profile and sub-features in the RSTRENG model	65
Figure 4.3 A portion of the naturally corroded external surface of a pipe specimen in Zhang et al. (2018) and Zhang et al. (2020).....	66
Figure 4.4 Corrosion clusters on representative pipe specimens reported in Benjamin et al.(2016), Al-Owaisi et al. (2018) and Zhang et al. (2020)	67
Figure 4.5 Illustration of the circumferential and riverbed profiles in RSTRENG-M	70
Figure 4.6 Mean and COV of test-to-predicted burst capacity ratios for RSTRENG-M as a function of the weighting factor q	71
Figure 4.7 Comparison of test and predicted burst capacities for RSTRENG-M, RSTRENG and Psqr models	73
Figure 4.8 Assumed ILI-identified corrosion anomalies and cluster on specimen 16-1 in Table 4.1	76
Figure 4.9 A corrosion cluster consisting of cubic and semi-ellipsoidal individual anomalies	77

Figure 4.10 Comparison between the RSTRENG, RSTRENG-M and Psqr models based on the 14 simulated ILI measured clusters	78
Figure 4.11 Relationships between d_{avg-s} and d_{max-s} , and d_{rep} and d_{max-s} , based on 30,763 circumferential profiles obtained from 667 clusters on 16 naturally corrode pipe specimens	79
Figure 4.12 Comparisons of predicted burst capacities and the riverbed profiles when the riverbed profile is obtained by Eq. (4.6) or by assuming the corrosion anomalies as cubic and semi-ellipsoidal metal losses.....	80
Figure 5.1 2D and 3D images of a corroded surface measured by the laser scanner	85
Figure 5.2 Corrosion depths on segment #1 with the corrosion threshold $z_{th}= 5\%t$ imposed	89
Figure 5.3 Illustration of the correspondence between Z and G	91
Figure 5.4 Empirical $f_c(x, y)$ values for pipe segment #1	93
Figure 5.5 Empirical CDFs at different separation distances versus the fitted CDF for the five pipe segments in Table 5.1.....	95
Figure 5.6 Lognormal probability papers for the corrosion depths measured with $\Delta x \geq 60$ mm and $\Delta y \geq 60$ mm on the five pipe segments in Table 5.1	96
Figure 5.7 Values of \tilde{r}_G for the five pipe segments	97
Figure 5.8 Fitting accuracy of Eq. (5.8) for the five pipe segments	98
Figure 5.9 Comparisons between the simulated and scanned corrosion surfaces of pipe segments #1 and #2.....	100
Figure 5.10 Illustration of the 1 inch \times $6t$ interaction rule.....	101
Figure 5.11 Geometric characteristics comparison between the real and simulated corrosion anomalies on pipe segments #1 and #2.....	103
Figure 5.12 Geometric characteristics comparison between the real and simulated corrosion clusters on the pipe segments #1 and #2.....	103

Figure 5.13 Comparison between the empirical CDFs of the burst capacities corresponding to the real and simulated corrosion clusters on pipe segments #1 and #2	104
Figure 5.14 Empirical CDF of the burst capacities of critical corrosion clusters corresponding to 100 realizations of simulated corrosion fields for pipe segments #1 and #2.....	104
Figure 5.15 Impact of correlation length on the simulated corrosion field for pipe segment #1	105
Figure 6.1 Illustration of corrosion anomaly, corrosion cluster, river-bottom path and river-bottom profile.....	110
Figure 6.2 Illustration of the DNV model and combined corrosion anomaly	114
Figure 6.3 Illustration of the CPS model and the determination of the parameter g	116
Figure 6.4 Illustration of the plausible profiles and Psqr model.....	117
Figure 6.5 A realization of the random corrosion field with $m_H = 8.6 \%t$, $v_H = 39.8\%$ and $\Delta_c = 35$ mm	119
Figure 6.6 Lengths and widths of the 120 corrosion clusters on the pipe segments made by X52, X60 and X70 steels	119
Figure 6.7 Configuration of the FEA model containing a synthetic corrosion cluster	120
Figure 6.8 Comparison between the FEA and predicted burst capacities in terms of different semi-empirical models based on the 120 synthetic corrosion clusters	123
Figure 6.9 Impact of the maximum depths of corrosion clusters on the model accuracy	125
Figure 6.10 Impact of the lengths of corrosion clusters on the model accuracy	126
Figure A.1 Corroded areas on specimens #2 - #14 in Table 2.2 and critical corrosion clusters identified based on different interaction rules	140

List of Appendices

Appendix A Corroded areas and critical corrosion clusters on specimens #2 - #14	137
Appendix B Derivation of Eq. (5.4).....	141
Appendix C Parametric expression of f_c for pipe segment #1	141

List of Abbreviations and Symbols

Abbreviations

ASME	American Society of Mechanical Engineers
AXGR	axial grooving
AXSL	axial slotting
CDF	cumulative distribution function
CIGR	circumferential grooving
CISL	circumferential slotting
COV	coefficient of variation
CSA	Canadian Standards Association
DNV	Det Norske Veritas
FEA	finite element analysis
FFS	fitness-for-service
GEN	general corrosion
ILI	inline inspection
MFL	magnetic flux leakage
ML	maximum likelihood
PDF	probability density function
PHMSA	Pipeline and Hazardous Material Safety Administration
PINH	pin hole
PITT	pitting
POF	pipeline operators forum
SMYS	specified minimum yield strength
SMTS	specified minimum tensile strength
2D	two dimensional
3D	three dimensional

Symbols

Chapter 1

D	pipe outside diameter
M	Folias factor
P_{b-CPS}	burst capacity predicted by CPS model
P_{b-PCO}	burst capacity predicted by PCORRC model
P_{b-PCOM}	burst capacity predicted by PCORRC-M model
P_{PP}	burst capacity of a plain pipe
P_{LG}	burst capacity of a pipe containing an axially-oriented infinitely-long groove
V	metal loss volume of a corrosion anomaly
d_{ave}	average corrosion depth of the river bottom profile
$d_{eff-DNV}$	effective depth in the DNV model
$d_{ave-Psqr-eff}$	average depth of the effective areas in the Psqr model
$d_{ave-RST-eff}$	average depth of the effective areas in the RSTRENG model
d_{eqv}	equivalent depth
$d_{max,1}, d_{max,2}$	maximum corrosion depths of two plausible profiles in Psqr model
d_{max}	maximum corrosion depth of the corrosion feature
g	interpolation parameter in CPS model
l	length of a corrosion feature
l_e	length of an effective portion of a river bottom profile
t	pipe wall thickness
w	width of a corrosion feature
σ_f	flow stress
σ_u	tensile strength of the pipe steel
σ_y	yield strength of the pipe steel

Chapter 2

A_i	area of the portion of the river-bottom profile occupied by the i^{th} sub-feature
E	Young's modulus

D	pipe outside diameter
K	strength coefficient
L	length of the scanned area
M_i	Folias factor
P_{FEA}	burst pressure of the i^{th} sub-feature by using the FEA model
P_{FEA-b}	burst capacity of the corrosion area predicted by FEA
$P_{FEA}(d_{th})$	FEA-predicted burst capacities by imposing d_{th}
$P_{FEA-\bullet}$	FEA-predicted burst capacities of the critical corrosion clusters generated according to interaction rule •
P_{RST}	burst pressure of the corrosion feature by using the RSTRENG model
P_{RST-b}	burst capacity of the corrosion area predicted by RSTRENG
$P_{RST,i}$	burst pressure of the i^{th} sub-feature by using the RSTRENG model
$P_{RST}(d_{th})$	RSTRENG-predicted burst capacities by imposing d_{th} .
$P_{RST-\bullet}$	RSTRENG-predicted burst capacities of the critical corrosion clusters generated according to interaction rule •
P_{test}	burst capacity observed in the tests
W	width of the scanned area
d_{max}	maximum corrosion depth within the scanned area
d_{th}	depth threshold value
e	base of natural logarithm
$e_{FEA-\bullet}$	percentage increase of the FEA prediction of the critical corrosion clusters generated according to interaction rule •
$e_{RST-\bullet}$	percentage increase of the RSTRENG prediction of the critical corrosion clusters generated according to interaction rule •
l_i	length of the i^{th} sub-feature
l_1	length of the 1 st corrosion anomaly
l_2	length of the 2 nd corrosion anomaly
n	strain hardening exponent
s_c	circumferential separation distance
$(s_c)_{lim}$	circumferential interaction limit
s_l	longitudinal separation distance

$(sl)_{lim}$	longitudinal interaction limit
t	pipe wall thickness
w_1	width of the 1 st corrosion anomaly
w_2	width of the 2 nd corrosion anomaly
x	spatial coordinates along the x direction
y	spatial coordinates along the y direction
z	spatial coordinates along the z direction
ε	true strain
$\varepsilon_{FEA}(d_{th})$	percentage increase of the FEA prediction corresponding to d_{th}
$\varepsilon_{RST}(d_{th})$	percentage increase of the RSTRENG prediction corresponding to d_{th}
σ	true stress
σ_u	tensile strength of the pipe steel
σ_y	yield strength of the pipe steel

Chapter 3

A_e	effective area of the corrosion anomaly
A_i	area of the portion of the river-bottom profile occupied by the i^{th} sub-feature
A_r	effective area
D	pipe outside diameter
E	Young's modulus
K	strength coefficient
M_i	Folias factor
P_{b-CSA}	burst capacity predicted by using CSA
P_{b-PCO}	burst capacity predicted by using PCORRC
P_{b-PCOM}	burst capacity predicted by using PCORRC-M
P_{b-RST}	burst capacity predicted by using RSTRENG
P_{b-S92}	burst capacity predicted by using Shell92
P_{b-31G}	burst capacity predicted by using B31G
P_{b-31GM}	burst capacity predicted by using B31G-M
$P_{b-\bullet}$	burst capacity evaluated using the model \bullet
P_{FEA}	FEA-predicted burst capacities

P_{test}	burst capacities observed from full-scale burst tests
V	metal loss volume of a corrosion anomaly
d_a	maximum depth of corrosion anomalies
d_{ave}	the average depth of the river-bottom profile
d_{equiv}	equivalent depth
d_{max}	maximum depth of corrosion features
e	base of natural logarithm
l	length of corrosion features
l_a	length of corrosion anomalies
l_e	effective length of the corrosion anomaly
l_r	effective length
n	strain hardening exponent
t	pipe wall thickness
w_a	width of corrosion anomalies
ε	true strain
σ	true stress
σ_f	flow stress
σ_u	tensile strength of the pipe steel
σ_y	yield strength of the pipe steel

Chapter 4

A_i	area of the portion of the river-bottom profile occupied by the i^{th} sub-feature
A_r	effective area of the corrosion feature
D	pipe outside diameter
M_i	Folias factor
$P_{b,i}$	burst capacity for the i^{th} sub-feature
P_{b-PSQR}	predicted burst capacity by using the Psqr model
P_{b-RST}	predicted burst capacity by using the RSTRENG model
P_{b-RSM}	predicted burst capacity by using the RSTRENG-M model
P_{test}	burst capacities observed from full-scale burst tests

S_j	j^{th} circumferential profile
$d_{avg,j}$	average depth of the portion of S_j that is deeper than $0.1t$
d_{avg-s}	average depth of a given circumferential profile S
d_{max}	maximum depth of corrosion features
$d_{max,j}$	maximum depth of the portion of S_j that is deeper than $0.1t$
d_{max-s}	maximum depth of a given circumferential profile S
$d_{rep,j}$	representative depth of S_j
l	length of corrosion features
l_i	length of the i^{th} sub-feature
l_r	effective length of the corrosion feature
m	total number of circumferential planes
n	total number of sub features
q	a weighting factor for RSTRENG-M model
t	pipe wall thickness
Δl	longitudinal resolution of the riverbed profile
Δw	circumferential resolution of the riverbed profile
σ_y	yield strength of the pipe steel

Chapter 5

D	pipe outside diameter
$F_Z(z)$	cumulative distribution function of z
G	latent Gaussian random field
H	an unknown cumulative distribution function
L	longitudinal length of the scanned pipe surface
L_1, L_2, L_3, L_4	likelihood functions belong to scenarios 1), 2), 3) and 4)
S_C	circumferential separation distance between two anomalies
S_L	longitudinal separation distance between two anomalies
W	circumferential length of the scanned pipe surface
Z	the random field of corrosion depths
c_{ij}	coefficients of the Fourier sine series
f_c	probability of nonzero corrosion depth

g_0	threshold value of the latent Gaussian random field
$g^{\bullet}_{0,1}, g^{\bullet}_{0,2}$	values of g_0 at z_1 and z_2
l_a	length of corrosion anomalies
l_c	length of corrosion clusters
m_H	mean value of the shifted lognormal distribution
n	total number of pairs of grid points at a certain separation distance
n_1, n_2, n_3, n_4	numbers of pairs of grid points belong to the scenarios 1), 2), 3) and 4)
r_G	correlation coefficient
\tilde{r}_G	correlation coefficient estimated by maximum likelihood method
t	pipe wall thickness
v_H	COV of the shifted lognormal distribution
w_a	width of corrosion anomalies
w_c	width of corrosion clusters
x	spatial coordinates along the x direction
y	spatial coordinates along the y direction
z	corrosion depth
z_a	depth of corrosion anomalies
z_c	depth of corrosion clusters
z_{max}	maximum corrosion depth of the scan surface recorded by the laser scan
z_{th}	threshold depth
Δ_c	correlation length
Δ_{cx}	correlation length along the longitudinal direction
Δ_{cy}	correlation length along the circumferential direction
Δx	longitudinal separation distance between two points
Δy	circumferential separation distance between two points
Φ	cumulative distribution function of standard Gaussian distribution
$\Phi_2(\bullet, \bullet, r_G)$	CDF of a standard bivariate Gaussian distribution with a correlation coefficient of r_G
ϕ	PDF of a standard Gaussian distribution
$\phi_2(\bullet, \bullet, r_G)$	PDF of a standard bivariate Gaussian distribution with a correlation coefficient of r_G

Chapter 6

E	Young's modulus
D	pipe outside diameter
K	strength coefficient
L	length of the random field
P_{b-CPS}	burst capacity of the corrosion feature predicted by CPS model
P_{b-CSA}	burst capacity of the corrosion feature predicted by CSA model
P_{b-DNV}	burst capacity of the corrosion feature predicted by DNV model
P_{b-DNV}^i	predicted burst capacity of anomaly i by using the DNV model
P_{b-DNV}^{12}	predicted burst capacity of combined anomaly 1-2 by using the DNV model
P_{b-Psqr}	burst capacity of the corrosion feature predicted by Psqr model
P_{b-RSM}	burst capacity of the corrosion feature predicted by RSTRENG-M model
P_{FEA}	FEA predicted burst capacity of corrosion features
P_{LG}	burst capacity of a pipe containing an axially-oriented infinitely-long groove
P_{PP}	burst capacity of a plain pipe
W	width of the random field
c_{ij}	coefficients of the Fourier sine series
$d_{eff,12}$	effective depth of combined anomaly 1-2
d_{eva}	corrosion depths of the evaluation point
d_i	corrosion depths of the i^{th} measurement point
d_{max}	maximum depth of corrosion features
$d_{max,i}$	maximum corrosion depth of the i^{th} corrosion anomaly
e	base of natural logarithm
$f_c(x,y)$	probability of nonzero corrosion depth at point (x,y)
g	interpolation parameter in CPS model
g_{eva}	interpolation parameter at the evaluation point
l	length of corrosion features
l_{12}	length of combined anomaly 1-2

l_i	length of the i^{th} corrosion anomaly
m_H	mean of the shifted lognormal distribution
n	strain hardening exponent
$s_{l,1}$	longitudinal spacing between anomalies 1 and 2
t	pipe wall thickness
v_H	COV of the shifted lognormal distribution
w	width of the corrosion feature
x	spatial coordinates along the x direction
x_i	longitudinal coordinates of the i^{th} measurement point
x_{eva}	longitudinal coordinates of the evaluation point
y	spatial coordinates along the y direction
z_{max}	maximum corrosion depths of the simulated corrosion surfaces
Δ_c	correlation length
Δx	longitudinal measurement resolution
ϵ_{crit}	true strain at the point of necking
σ_{crit}	true stress at the point of necking
σ_y	yield strength of the pipe steel
σ_u	tensile strength of the pipe steel

1 Introduction

1.1 Background

Canada has a vast network of interprovincial and international pipelines that serve a vital role in transporting oil and natural gas. Although historical statistics show that pipelines are safe, efficient and reliable, failures can still occur for a variety of reasons such as corrosion, third-party interference, material defects and ground movement. The metal loss corrosion is one of the main reasons for the damages and failures in pipelines (Cosham et al. 2007). According to the Pipeline and Hazardous Material Safety Administration (PHMSA) in the United States, corrosion caused 32% of reported incidents on the gas transmission pipelines in the US between 2002 and 2013 (Lam and Zhou 2016).

Pipelines are usually protected by coatings and cathodic protection systems. However, the effectiveness of the protective systems diminishes over time, resulting in the development of metal loss corruptions on the external surfaces of pipelines. The Fitness-For-Service (FFS) assessment is commonly carried out by pipeline engineers to demonstrate the integrity of a pipeline that whether a corroded pipe joint is fit for continued service (Anderson 2007). The FFS assessment of a corroded pipeline involves corrosion anomaly detection and identification, obtaining anomaly information through inspection, combing anomalies into clusters based on interaction rules and applying practical assessment models to evaluate the remaining strengths of the pipeline at the corrosion clusters (ASME 2018; Xie and Tian 2018).

The in-line inspection (ILI) tool is the most common practice throughout the pipe industry to detect the metal loss anomalies on the pipelines. The ILI tools identify and size the metal loss anomalies through a data analysis process. A metal loss reporting threshold (depth threshold) is determined that only metal losses with the maximum corrosion depth above the threshold will be identified (POF 2016). As shown in Fig. 1.1, when a metal loss anomaly is detected by the ILI tools, the anomaly is identified by the ILI tool as a box with ILI-measured length and width. As mentioned by Pipeline Operators Forum (POF 2016), the measurement capabilities of ILI inspection tool depend on the geometry of the

metal loss anomalies. The POF system categorizes a given corrosion anomaly into one of seven classes depending on the length and width of corrosion anomaly, namely general (GEN), pitting (PITT), axial grooving (AXGR), circumferential grooving (CIGR), pin hole (PINH), axial slotting (AXSL) and circumferential slotting (CISL).

The burst capacity of a colony of corrosion anomalies is lower than the burst capacities of the individual anomalies in the colony, which is known as the interacting behavior of corrosion anomalies. The closely spaced metal loss anomalies will be combined into corrosion clusters based on the interaction rules (Lamontagne 2002). The commonly used interaction rules are DNV (DNV 2017), B31.4 (ASME 2019), B31G (ASME 2018), CSA (CSA 2019) and CW (Coulson and Worthingham 1990). After the data analysis, the ILI inspection results are reported in a spreadsheet format, which includes the maximum depths, lengths, widths, identifications, longitudinal locations and circumferential orientations for both corrosion clusters and the corrosion anomalies contained in the corrosion clusters (Fig. 1.2).

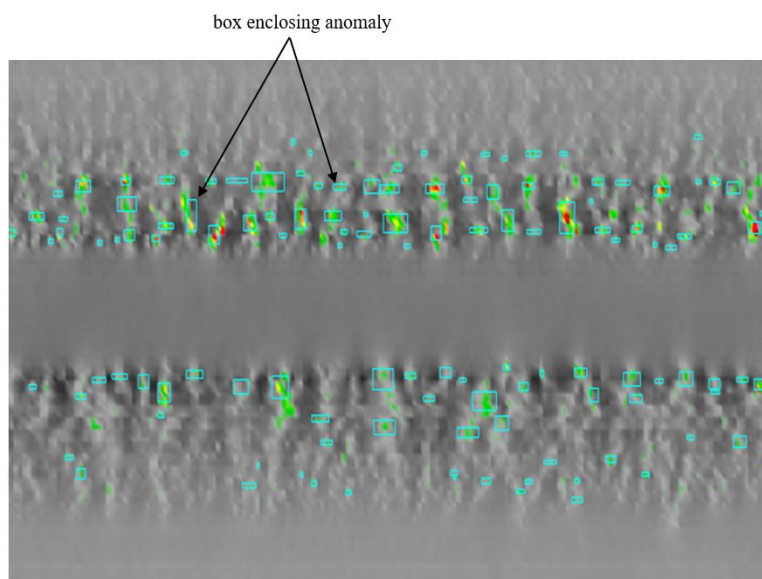


Figure 1.1 Corrosion anomaly identification by ILI tools

BJ Identifier	BJ Parent Cluster ID	Cluster Method	BJ Chainage (m)	Clock Position (h:mm)	Wall Thick. (cm)	Peak Depth (%)	Avg. Depth (%)	Length (cm)	Width (cm)
GWD 10			1.2		0.953				
GWD 20			1.5		0.953				
GWD 30			7.6		0.953				
GWD 40			7.9		0.953				
GWD 50			9.8		0.953				
GWD 60			11.0		0.714				
DMA 1	-		12.8	05:15	0.714	6		1.45	1.60
GWD 70			14.2		0.714				
TEE 1			15.0	12:00	0.714			22.68	32.00
GWD 80			16.5		0.714				
TEE 2			16.9	12:00	0.714			40.69	59.39
GWD 90			17.3		0.714				
GWD 100			17.9		0.714				
VLV 1			19.0		0.714			18.24	10.90
GWD 110			20.0		0.714				
GWD 120			20.6		0.714				
TEE 3			21.0	12:00	0.714			40.75	52.80
GWD 130			21.4		0.714				
SLV 1			22.3		0.714			31.51	147.07
TEE 4			22.9	12:00	0.714			23.50	32.00
GWD 140			23.7		0.714				
GWD 150			23.7		0.714				
DMA 2	-		25.2	08:15	0.714	7		0.84	0.81
GWD 160			25.4		0.714				
DMA 3	-		25.5	06:30	0.714	7		1.27	1.36
DMA 4	CLS 1		26.2	08:00	0.714	6		0.88	1.02
CLS 1		3t x 3t	26.2	08:00	0.714	6	4	3.05	1.02
DMA 5	CLS 1		26.2	08:00	0.714	6		1.29	0.82
DMA 6	-		26.7	08:15	0.714	9		1.29	1.48
DMA 7	-		27.1	05:15	0.714	6		3.33	1.32

Figure 1.2 Illustration of typical ILI results

A multi-level FFS assessment philosophy is widely used by the pipeline industry to evaluate the burst capacity of corroded pipelines according to the data available to pipeline operators (Chouchaoui 1993; Cronin 2000; ASME 2016; ASME 2018). Each successive level (e.g. Levels 1, 2 and 3 of the ASME B31G standard (ASME 2018)) requires the greater amount of data and more computational effort to achieve more accurate outcomes. The Level 1 and Level 2 models employ the semi-empirical burst capacity models to evaluate the burst capacity of a corroded pipeline (ASME 2018). The Level 1 semi empirical models require only the maximum corrosion depth and length of a corrosion cluster to calculate the burst capacity, while the Level 2 models include greater details of the corrosion profile than Level 1 models to account for the actual geometry of the metal loss.

This thesis includes four existing Level 1 models, i.e. ASME B31G (ASME 2018), B31G Modified (B31G-M) (Kiefner and Vieth 1989), Shell92 (Ritchie and Last 1995) and PCORRC (Leis and Stephens 1997; Stephens and Leis 2000) models, and six existing Level 2 semi-empirical burst capacity models, i.e. RSTRENG (Kiefner and Vieth 1989), CSA (CSA 2019), DNV (DNV 2017), CPS (Cronin and Pick 2002), PCORRC Modified (PCORRC-M) (Mokhtari and Melchers (2019)) and Psqr (Zhang et al. 2018) models. The

B31G, B31G-M, Shell92, RSTRENG, CSA, DNV and Psqr are derived from the NG-18 equation (Maxey et al. 1972), in which the burst capacity P_b is calculated by:

$$P_b = \frac{2\sigma_f t}{D} \times \frac{1 - SF \times \frac{d_{max}}{t}}{SF \times \frac{d_{max}}{t} / M} \quad (1.1)$$

where σ_f denotes the flow stress and is differently defined by different models; SF denotes the shape factor characterizing the shape idealization and equals the ratio of the metal-loss area to the rectangular area with length and width equal to the length and maximum depth of corrosion cluster, respectively (Zhang et al. 2018), and d_{max} denotes the maximum depth. t and D are the pipe wall thickness and the outside diameter of the pipe. M is the bulging factor. In general, three bulging factors are developed.

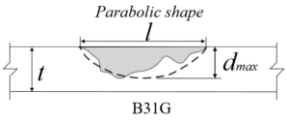
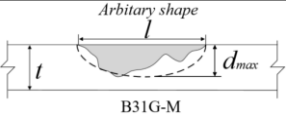
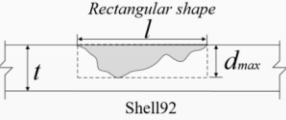
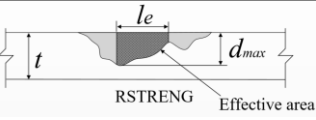
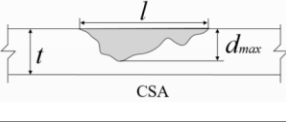
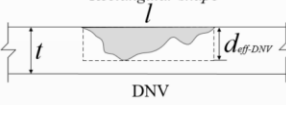
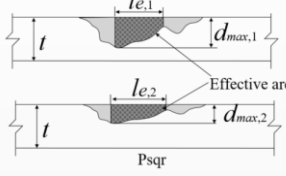
$$M_1 = \sqrt{1 + 0.8 \frac{l^2}{Dt}} \quad (1.2)$$

$$M_2 = \begin{cases} \sqrt{1 + 0.6275 \frac{l^2}{Dt} - 0.003375 \left(\frac{l^2}{Dt}\right)^2} & \frac{l^2}{Dt} \leq 50 \\ 3.3 + 0.032 \frac{l^2}{Dt} & \frac{l^2}{Dt} > 50 \end{cases} \quad (1.3)$$

$$M_3 = \sqrt{1 + 0.31 \frac{l^2}{Dt}} \quad (1.4)$$

Table 1.1 summarizes the shape idealizations, definitions of SF, flow stress and the bulging factors for different models. In Table 1.1, l_e denotes the length of the effective area used in the RSTRENG and Psqr model. d_{ave} is the average corrosion depth of the river bottom profile. $d_{ave-RST-eff}$ and $d_{ave-Psqr-eff}$ are the average depth of the effective areas in the RSTRENG and Psqr model, respective. $d_{eff-DNV}$ is the effective depth defined in the DNV model. Since Psqr model considers multiple plausible corrosion profiles, e.g. the corrosion profiles with maximum corrosion depth $d_{max,1}$ and $d_{max,2}$, to evaluate the burst capacity, multiple effective areas are figured out in the Psqr model as shown in Table 1.1.

Table 1.1 Definitions of the shape idealizations, SF, flow stress and the bulging factors for different models

Model	Shape idealization	Shape factor	Flow stress	Bulging factor
B31G		2/3	$1.1\sigma_y$	M_1
B31G-M		0.85	$\sigma_y + 10\text{ksi}$	M_2
Shell92		1	$0.9\sigma_u$	M_1
RSTRENG		$d_{ave-RST-eff}/d_{max}$	$\sigma_y + 10\text{ksi}$	M_2
CSA		d_{ave}/d_{max}	$0.9\sigma_u$	M_2
DNV		$d_{eff-DNV}/d_{max}$	σ_u	M_3
Psqr		$d_{ave-Psqr-eff}/d_{max}$	$\sigma_y + 10\text{ksi}$	M_2

The PCORRC, PCORRC-M model and CPS models were not developed from NG-18 equation. The PCORRC and PCORRC-M were based on results of parametric FEA. The prediction equations of PCORRC and PCORRC-M models are listed as follows.

PCORRC

$$P_{b-PCO} = \frac{2t\sigma_u}{D} \left[1 - \frac{d_{max}}{t} \left(1 - \exp \left(\frac{-0.157l}{\sqrt{\frac{D(1-d_{max}/t)}{2}}} \right) \right) \right] \quad l \leq 2D \text{ and } \frac{d_{max}}{t} \leq 0.8 \quad (1.5)$$

PCORRC-M

$$P_{b-PCOM} = \frac{2t\sigma_u}{D} \left[1 - \frac{d_{eqv}}{t} \left(1 - \exp \left(\frac{-0.157l}{\sqrt{\frac{D(1-d_{eqv}/t)}{2}}} \right) \right) \right] \quad l \leq 2D \text{ and } \frac{d_{max}}{t} \leq 0.8 \quad (1.6)$$

where

$$d_{eqv} = \left(\frac{V}{lw} + d_{max} \right) / 2 \quad (1.7)$$

The CPS model considers the burst capacity of a pipe segment containing a corrosion feature, P_{b-CPS} , to be bounded by the burst capacity of a plain (corrosion free) pipe, P_{PP} , as the upper limit and the burst capacity of a pipe containing an axially-oriented infinitely-long groove having the same depth as the maximum depth of the corrosion feature, P_{LG} , as the lower limit. The burst capacity of the feature is then calculated from P_{PP} and P_{LG} with an interpolation parameter g ($0 \leq g \leq 1$) depending on the pipe geometry and corrosion morphology.

$$P_{b-CPS} = P_{LG} + g(P_{PP} - P_{LG}) \quad (1.8)$$

The detailed description of CPS model will be presented in Section 6.2.2.

The Level 3 evaluation method usually refers to a numerical analysis, e.g. finite element analysis (FEA), associated with full justification for loading, boundary conditions, material properties and failure criteria (ASME 2018). Hence, the corrosion anomaly identification, interaction rules and the predictive accuracies of the semi empirical models are of great importance to the FFS assessment and the subsequent mitigation decisions.

Naturally occurring corrosion anomalies are three-dimensional metal loss flaws of irregular shapes developed on the external (internal or both) surface of pipe segments (see Fig. 1.3). However, due to the complex morphology of real corrosion anomalies, almost all the researches simplify the naturally occurring corrosion anomaly as the semi-ellipsoidal or

cubic corrosion metal loss such that full scale burst tests of the pipe segments containing artificially induced corrosion anomalies are commonly used to investigate the interaction behaviors of closely spaced corrosion anomalies and the predictive accuracies of the burst capacity models (Chouchaoui 1993; Kiefner et al. 1993; Kiefner et al. 1996; Benjamin et al. 2005; Benjamin et al. 2016; Al-Owaisi et al. 2018). Compared to the semi-empirical burst capacity models, FEA is recognized as the most accurate assessment method to determine the burst capacities of corroded pipe segments. The FEA has been widely used to improve the existing semi empirical models (Leis and Stephens 1997; Chen et al. 2015; Wang and Zarghamee 2013), as well as investigating the interaction behaviors of corrosion anomalies (Mondal and Dhar 2017; Sun and Cheng 2018), based on simulations of pipe segments containing the artificially induced corrosion anomalies.

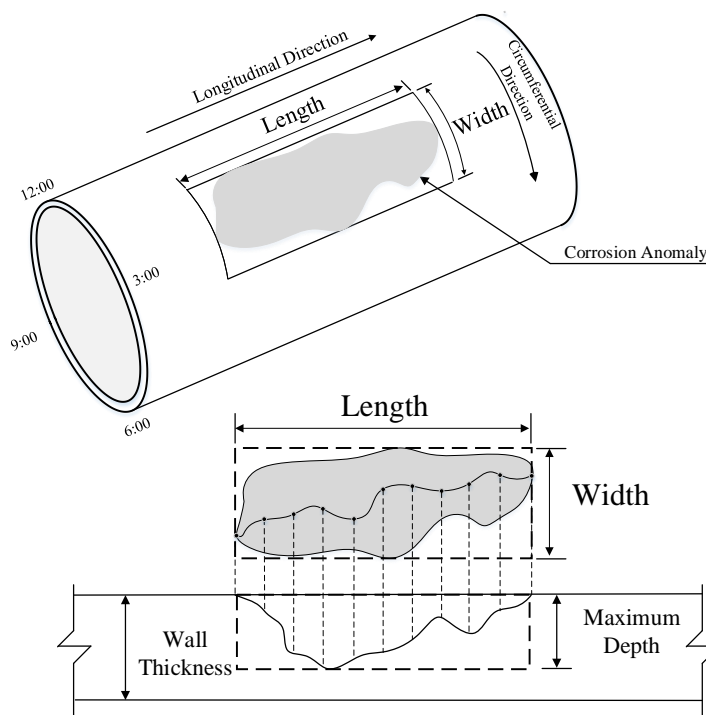


Figure 1.3 Illustration of a naturally occurring corrosion anomaly on the pipe segment

Since artificially-induced corrosion anomalies are in general regular-shaped, e.g. cubic or semi-ellipsoidal, they do not capture geometric characteristics of naturally occurring corrosions. It follows that the specimens containing artificially-induced anomalies may not be suitable for the studies of FFS assessment methodologies. Pipe segments containing

naturally occurring corrosion anomalies are ideal to investigate the interaction behaviors of corrosion anomalies and the predictive accuracies of the burst capacity models (Kiefner et al. 1996; Zhang et al. 2018). In particular, Zhou and Huang (2012) investigated the model accuracies of several well-known Level 1 and Level 2 semi empirical models and reported that all the existing models are associated with considerable model errors. However, the high cost of obtaining naturally corroded pipe segments from the in-service pipelines and executing the full-scale burst tests greatly limit the number of pipe segments that are available to the research.

1.2 Objective

The research reported in this thesis is supported by the Natural Sciences and Engineering Research Council (NSERC) of Canada and TC Energy Ltd. The objectives of this research are summarized as follows.

- 1) Investigate the impact of removing the corrosions shallower than the depth threshold and applying different interaction rules on the corrosion cluster identification and burst capacity predictions of naturally corroded pipelines by using the FEA and RSTRENG models.
- 2) Investigate the predictive accuracies of several widely used burst capacity models to help pipeline engineers select the most suitable models for different POF corrosion anomaly classes.
- 3) Develop a new burst capacity prediction model to improve the predictive accuracy of the existing semi-empirical models.
- 4) Develop a random field model to simulate the naturally corroded pipe surfaces, which can greatly facilitate the numerical (as opposed to physical) full-scale burst tests of naturally corroded pipe specimens to improve existing semi-empirical burst capacity models and develop new burst capacity models.

5) Combine the random field-based corrosion model and FEA to create a large database to validate the new burst capacity prediction model.

This research will improve the current FFS assessments by introducing the naturally occurring corrosion anomalies to the investigation of interaction rules and the predictive accuracies of the burst capacity evaluation models.

1.3 Scope of the study

This thesis consists of five main topics, which are presented in Chapters 2 to 6, respectively. Chapter 2 develops three-dimensional finite element models to simulate the full-scale burst tests of pipe segments containing naturally occurring corrosion anomalies. The finite element models are validated by comparing the burst capacities observed in the tests and the values evaluated by FEA. The FEA, as well as the RSTRENG model, is used to study the impact of different depth thresholds and five commonly used interaction rules, namely DNV, B31.4, 3WT, 6WT and CW, on the burst capacity predictions of naturally corroded pipe segments.

Chapter 3 investigates the impact of corrosion anomaly classes on the prediction accuracies of seven existing burst capacity models for corroded pipelines based on a large amount of corrosion anomalies on naturally corroded pipe specimens. The corrosion anomalies are classified into pin hole, axial slotting, axial grooving, circumferential slotting, circumferential grooving, pitting and general corrosion, based on the Pipeline Operators Forum (POF) anomaly classification system. The seven burst capacity models and finite element analyses (FEA) are employed to evaluate the burst capacities of the corrosion anomalies. The accuracies of the burst capacity models are assessed and compared based on the FEA-to-model predicted burst capacity ratios for different classes of anomalies.

Chapter 4 proposes a modified RSTRENG model, named RSTRENG-M, to evaluate the burst capacity of corroded pipelines by employing the riverbed profile (as opposed to the river-bottom profile in RSTRENG) of the corrosion feature. The predictive accuracy of the RSTRENG-M model is investigated based on full-scale burst tests of 16 naturally

corroded pipe specimens and 44 specimens containing artificially induced corrosion features. An empirical equation is also developed to estimate the representative depth for a given circumferential profile directly from the corresponding maximum depth to facilitate the application of RSTRENG-M in the context of the inline inspection data.

Chapter 5 proposes a random field model to characterize the corrosion depth on the external surface of buried oil and gas pipelines. The model addresses the intermingling nature of corroded and corrosion-free areas on the pipe surface by using a latent homogeneous Gaussian random field and a spatial position-dependent threshold associated with the latent Gaussian field. High-resolution corrosion measurement data obtained from corroded pipe segments removed from in-service pipelines are used to estimate parameters of the proposed model, including the probability of corrosion at a given point, marginal distribution of the nonzero corrosion depth and correlation structure of the latent Gaussian field.

In Chapter 6, the naturally corroded external surfaces of underground pipelines are simulated by the random field-based corrosion model. The B31.4 interaction rule is employed to group the corrosion anomalies on the simulated corrosion surfaces into corrosion clusters. The burst capacities of 120 synthetic corrosion clusters with maximum corrosion depths between 30 and $70\%t$ are evaluated by using both six existing Level 2 semi empirical models and FEA. The predictive accuracies of the six models are assessed and compared based on the FEA-to-model predicted ratios.

1.4 Thesis format

This thesis is prepared in an Integrated-Article Format as specified by the School of Graduate and Postdoctoral Studies at Western University, London, Ontario, Canada. Seven chapters are included in the thesis. Chapter 1 presents the introduction of the thesis which includes the research background, objective and research significance, scope of the study and thesis format. Chapters 2 through 6 are the main body of the thesis, of which each chapter solves an individual topic. The main conclusions and recommendations for future research regarding the topics in the thesis are provided in Chapter 7.

References

- Al-Owaisi. S., Becker. A. A., Sun. W., Al-Shabibi. A., Al-Maharbi. M., Pervez. T. and Al-Salmi. H. 2018. An experimental investigation of the effect of defect shape and orientation on the burst pressure of pressurized pipes. *Engineering Failure Analysis*. 93: 200 - 213.
- Anderson. T. L. 2007. Recent advances in fitness-for-service assessment. In: *Proceedings of the 4th Middle East Non-destructive Testing Conference and Exhibition*. Dec. 2 - 5. Kingdom of Bahrain.
- ASME. 2016. *Fitness-For-Service. API 579-1/ASME FFS-1*. June, 2016. The American Society of Mechanical Engineers, New York.
- ASME. 2018. *Manual for determining the remaining strength of corroded pipelines. Supplement to ASME B31 Code for Pressure Piping. ASME B31G - 2018*. New York, USA.
- ASME. 2019. *Pipeline transportation systems for liquids and slurries, ASME code for pressure piping, B31*. The American Society of Mechanical Engineers, New York, USA.
- Benjamin. A. C., Freire, J. L. F., Vieira. R. D., Diniz. J. L. C. and Andrade, E. Q. 2005. Burst tests on pipeline containing interacting corrosion defects. In: *Proceedings of OMAE2005 24th International Conference on Offshore Mechanics and Arctic Engineering*. Jun. 12 - 17, 2005, Halkidiki, Greece.
- Benjamin. A. C., Freire. J. L. F., Vieira. R. D. and Cunha. D. J. S. 2016. Interaction of corrosion defects in pipelines - Part 2: MTI JIP database of corroded pipe tests. *International Journal of Pressure Vessels and Piping*. 145: 41 - 59.
- Chen. Y., Zhang. H., Zhang. J., Li. X. and Zhou. J. 2015. Failure analysis of high strength pipeline with single and multiple corrossions. *Materials and Design*. 67: 552 - 557.
- Chouchaoui. B. 1993. *Evaluating the Remaining Strength of Corroded Pipelines*. Ph.D. thesis. Waterloo, Canada: Department of Mechanical Engineering, University of Waterloo.
- Cosham. A., Hopkins. P. and Macdonald. K. A. 2007. Best practice for the assessment of defects in pipelines - Corrosion. *Engineering Failure Analysis*. 14(7): 1245 - 1265.
- Coulson K. E. W. and Worthingham. R. G. 1990. Pipe corrosion-1: standard damage assessment approach is overly conservative. *Oil and Gas Journal*. 88(15): 54 - 59.
- Coulson K. E. W. and Worthingham. R. G. 1990. Pipe corrosion conclusion: new guidelines promise more accurate damage assessment. *Oil and Gas Journal*. 88(16): 41 - 44.

- Cronin, D. S. 2000. Assessment of corrosion damage in pipelines. Ph.D. thesis. Waterloo, Canada: Department of Mechanical Engineering, University of Waterloo.
- Cronin, D. S and Pick, R. J. 2002. Prediction of the failure pressure for complex corrosion defects. *International Journal of Pressure Vessels and Piping*. 79: 279 - 287.
- CSA. 2019. Oil and gas pipeline systems, CSA Standard Z662 - 19. Mississauga, Canada.
- DNV. 2017. Corroded Pipelines. DNV-RP-F101 code. Det Norske Veritas. Oslo, Norway.
- Kiefner, J. F. and Vieth, P. H. 1989. A modified criterion for evaluating the remaining strength of corroded pipe. Report prepared for American gas association. PR3 - 805. Columbus, OH, USA.
- Vieth, P. H. and Kiefner, J. F. 1993. Database of corroded pipe tests. Report prepared for the pipeline corrosion supervisory committee, Pipeline Research Committee of Pipeline Research Council International, Inc. PRCI Catalog No. L51689. Columbus, OH, USA.
- Kiefner J. F., Vieth P. H. and Roytman, I. 1996. Continued validation of RSTRENG. Report prepared for the line pipe research supervisory committee, Pipeline Research Committee of Pipeline Research Council International, Inc. PRCI. Catalog No. L51749e. Columbus, OH, USA.
- Lam, C. and Zhou, W. 2016. Statistical analyses of incidents on onshore gas transmission pipelines based on PHMSA database. *International Journal of Pressure Vessels and Piping*. 145: 29 - 40.
- Lamontagne, M. 2002. Interaction rules - an integral factor. In: *Proceedings of the NACE International Conference Corrosion*. Apr. 7 - 11. Denver, USA.
- Leis, B. N. and Stephens, D. R. 1997. An alternative approach to assess the integrity of corroded line pipe part I: current status; part II: alternative criterion. In: *Proceedings of the 7th International Offshore and Polar Engineering Conference*. May 25 - 30. Honolulu, USA.
- Maxey, W. A., Kiefner, J. F., Eiber, R. J. and Duffy, A. R. 1972. Ductile fracture initiation, propagation, and arrest in cylindrical vessels. Fracture toughness. In: *Proceedings of the 1971 National Symposium on Fracture Mechanics, Part II, ASTM STP 514*. American Society of Testing and Materials: 70 - 81.
- Mokhtari, M. and Melchers, R. E. 2019. Next generation fracture prediction models for pipes with localized corrosion defects. *Engineering Failure Analysis*. 105: 610 - 626.
- Mondal, B. C. and Dhar, A. S. 2017. Interaction of multiple corrosion defects on burst pressure of pipelines. *Canadian Journal of Civil Engineering*. 44(8): 589 - 597.

- Pipeline Operators Forum. 2016. Specifications and requirements for in-line inspection of pipelines. Version 2016.
- Ritchie. D. and Last. S. 1995. Burst criteria of corroded pipelines - defect acceptance criteria. In: Proceedings of the EPRG/RPC Biennial Joint Technical Meeting on Line Pipe Research. Apr. 18 - 21. Cambridge, UK.
- Stephens. D. R. and Leis. B. N. 2000. Development of an alternative failure criterion for residual strength of corrosion defects in moderate-to high-toughness pipe. In: Proceedings of the 2000 International Pipeline Conference. IPC2000. Oct. 1 - 5. Calgary, Canada.
- Sun. J. and Cheng. Y. F. 2018. Assessment by finite element modeling of the interaction of multiple corrosion defects and the effect on failure pressure of corroded pipelines. *Engineering Structure*. 165: 278 - 286.
- Wang. N. and Zarghamee. M. S. 2013. Evaluating Fitness-for-service of corroded metal pipelines: structural reliability bases. *Journal of Pipeline System Engineering and Practice*. 04013012: 1 - 9.
- Xie. M. and Tian. Z. 2018. A review on pipeline integrity management utilizing in-line inspection data. *Engineering Failure Analysis*. 92: 222 - 239.
- Zhou. W. and Huang. G. 2012. Model error assessments of burst capacity models for corroded pipelines. *International Journal of Pressure Vessels and Piping*. 99 - 100: 1 - 8.
- Zhang. S., Yan. J., Kariyawasam. S., Huang. T. and Al-Amin. M. 2018. A more accurate and precise method for large metal loss corrosion assessment. In: Proceedings of the 2018 International Pipeline Conference. IPC2018. Sept. 24 - 28. Calgary, Canada.

2 Influence of Depth Thresholds and Interaction Rules on the Burst Capacity Evaluation of Naturally Corroded Pipelines

2.1 Introduction

Metal-loss corrosion compromises the pressure containment capacity, i.e. burst capacity, of oil and gas pipelines and poses a direct threat to the integrity and safety of pipelines. While corrosion may occur on both the external and internal surfaces of the pipeline, the focus of the present study is the external corrosion. The fitness-for-service (FFS) assessment is commonly carried out to demonstrate the integrity of pipelines containing corrosion anomalies. The FFS assessment typically involves employing inline inspection (ILI) tools to identify and size corrosion anomalies, combining anomalies into clusters based on the so-called interaction rules and applying engineering critical assessment models to evaluate the burst capacities of the pipeline at the corrosion clusters (ASME 2016; ASME 2018).

A significant portion of the naturally corroded external surface of a pipe segment typically contains shallow corruptions, i.e. corrosion shallower than 10% of the pipe wall thickness (Bao and Zhou 2020). The shallow corrosion may not be detected or reported by ILI tools as such tools often have a minimum detectable or reportable limit for the corrosion depth (POF 2016). Even if shallow corruptions are reported by ILI, they are often ignored by pipeline integrity engineers during the process of identifying individual corrosion anomalies to simplify and facilitate the process. Implicit in this practical treatment is the assumption that ignoring shallow corruptions below a certain threshold value (d_{ih}) has a negligibly small (non-conservative) effect on the burst capacity evaluation. Such an assumption, however, has not been quantitatively validated in the literature.

A naturally corroded pipe segment usually contains multiple corrosion anomalies. The burst capacity of a colony of closely spaced corrosion anomalies is generally lower than the burst capacities of individual anomalies in the colony. This is known as the interaction effect. The so-called interaction rules (Lamontagne 2002) are used in practice to determine if multiple anomalies in proximity should be treated as a cluster to take into account the

interaction effect. In the past two decades, the FEA has proven to be a viable tool to study the interaction behaviors of closely-spaced corrosion anomalies. Mondal and Dhar (2016,2017) suggested that the maximum spacing (i.e. interaction limits) between two interacting anomalies depends on the pipe wall thickness, corrosion depth (i.e. in the pipe through-wall thickness direction) and orientation of anomalies (e.g. longitudinally or circumferentially aligned anomalies) based on the parametric FEA of pipe segments containing two idealized box-shaped corrosion anomalies. Al-Owaisi et al. (2018) carried out FEA to investigate the interactions between two corrosion anomalies on the external surface of the pipeline idealized as box- or semi-ellipsoidal-shaped. They concluded the shape of the corrosion anomaly has little influence on the interaction limits, while the orientation of anomalies has an important effect on the interaction behavior. Sun and Cheng (2018) developed FEA models to analyze the interaction behavior of multiple corrosion anomalies with varied geometries and reported that the longitudinally aligned corrosion anomalies are associated with more significant interaction effects than the circumferentially aligned anomalies. As Cronin (2000) pointed out, a key challenge of evaluating the interaction of naturally-occurring corrosion anomalies is that the number of possible permutations of geometric characteristics of adjacent anomalies is infinite. Hence, almost all the relevant literature focuses on the interaction between two idealized corrosion anomalies (Mondal and Dhar 2016; Mondal and Dhar 2018; Al-Owaisi et al. 2018; Sun and Cheng 2018) (e.g. the box-shaped and semi-ellipsoidal anomalies), whereas no work has been reported in the literature to investigate the interaction behavior of naturally-occurring, complex-shaped corrosion anomalies. Moreover, there is no study investigating the effectiveness of various commonly-used interaction rules for naturally-occurring corrosion anomalies.

Full-scale burst tests of 14 naturally corroded pipe segments were recently completed and reported by Zhang et al. (2018). The detailed digital profiles of corroded external surfaces of the pipe specimens were obtained by using high-resolution laser scanners and provided to the present study. This provides an opportunity to investigate the impact of the corrosion depth threshold and interaction rule on the burst capacity evaluation of naturally corroded pipelines. In this study, the burst capacities of the 14 pipe segments are evaluated using

FEA and the RSTRENG model (Kiefner and Vieth 1989), which is widely used in FFS assessment in practice, by considering different corrosion depth thresholds to filter out shallow corrosions on the pipe specimen. Five interaction rules are employed to generate 54 groups of significant corrosion clusters on the 14 pipe specimens. The corrosion clusters generated by different interaction rules are further compared in terms of the size and burst capacities determined by FEA and RSTRENG. The interaction rules considered in the present study include those recommended by DNV (DNV 2017), B31.4 (ASME 2019), CSA (CSA 2019), Coulson and Worthingham (1990a,b) and B31G (ASME 2018).

The rest of the chapter is organized as follows. Section 2.2 describes the 14 naturally corroded pipe specimens on which the analyses are based; Section 2.3 describes the corrosion anomaly identification based on the depth threshold and cluster identification based on the five interaction rules; Section 2.4 describes the FEA and RSTRENG model used to evaluate the burst capacity of the pipe specimens; Section 2.5 discusses the impact of the depth threshold and interaction rules on the burst capacity evaluation using the analysis results obtained from FEA and the RSTRENG model, followed by the conclusion in Section 2.6.

2.2 Naturally corroded pipe specimens

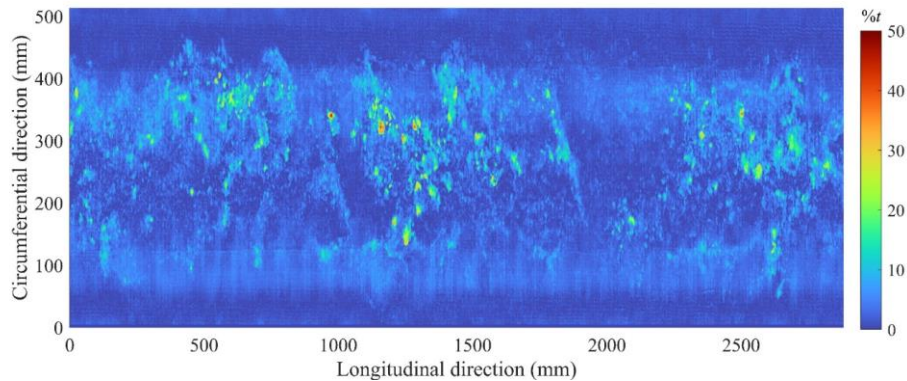
Table 2.1 summarizes geometric and material properties of the 14 naturally corroded pipe specimens mentioned in the previous section, as well as the burst capacities observed in the tests. The yield strength (σ_y), ultimate tensile strength (σ_u) and Young's modulus (E) are determined from the tensile tests of coupons extracted from the pipe bodies in the circumferential direction.

Table 2.1 Summary of 14 naturally corroded test specimens (Zhang et al. 2018)

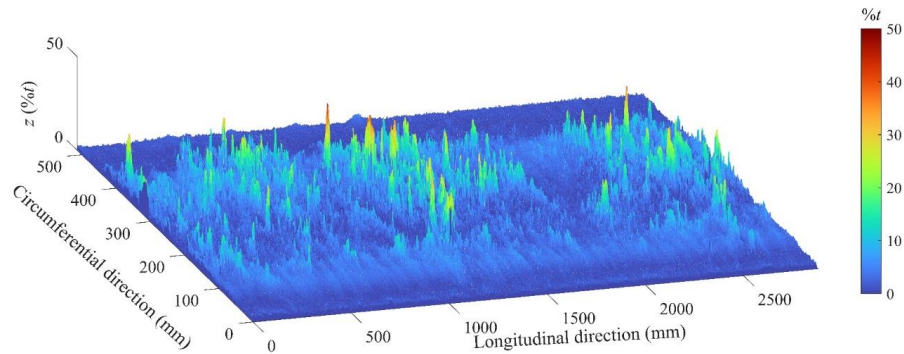
No.	Specimen ID	D (mm)	t (mm)	L (mm)	W (mm)	d_{max} (% t)	Steel grade	σ_y (MPa)	σ_u (MPa)	E (GPa)	P_{test} (MPa)
1	16-1	408.2	6.2	2880	520	42	X52	369	540	167	14.60
2	16-2	407.7	6.2	2720	563	47	X52	369	540	167	13.31
3	16-3	407.7	6.2	2400	623	43	X52	369	540	167	13.52
4	16-5	407.7	5.9	2080	556	97	X52	393	557	189	11.86
5	16-6	407.4	5.9	2080	623	87	X52	408	576	191	12.72
6	16-7	407.4	6.0	2400	616	87	X52	408	576	191	12.84
7	24-1	610.5	6.8	6387	408	32	X70	553	680	145	14.21
8	24-2	610.5	6.7	8080	497	39	X70	553	680	145	14.37
9	30-1	763.2	8.4	6147	500	68	X70	536	655	187	12.31
10	30-2	763.4	8.5	3127	461	48	X70	535	652	170	14.10
11	30-3	763.2	8.4	2467	606	73	X70	568	691	171	14.78
12	30-4	763.7	8.5	3401	456	78	X70	562	604	174	12.48
13	30-5	762.9	8.4	3520	728	87	X70	546	659	154	12.26
14	30-6	764.1	8.4	4544	630	75	X70	515	628	161	12.96

Note: D = outside diameter of the pipe segment; L = length of the scanned area; W = width of the scanned area; d_{max} = maximum corrosion depth within the scanned area; P_{test} = burst capacity observed in the tests.

The corrosion anomalies on external surfaces of the 14 specimens were measured by using a high-resolution laser scanning device. Figure 2.1 depicts the two-dimensional (2D) and three-dimensional (3D) images of the scanned external surface of specimen 16-1. The x and y coordinates are the longitudinal and circumferential positions (arclength) of a grid point on a regular scan grid of 2 (longitudinal) \times 1 (circumferential) mm with respect to a reference point (i.e. the origin). The z coordinate represents the corrosion depth, expressed as a percentage of the pipe wall thickness t , measured at the grid point. The lengths and widths of the 14 scanned areas are also included in Table 2.1.



a) 2D image



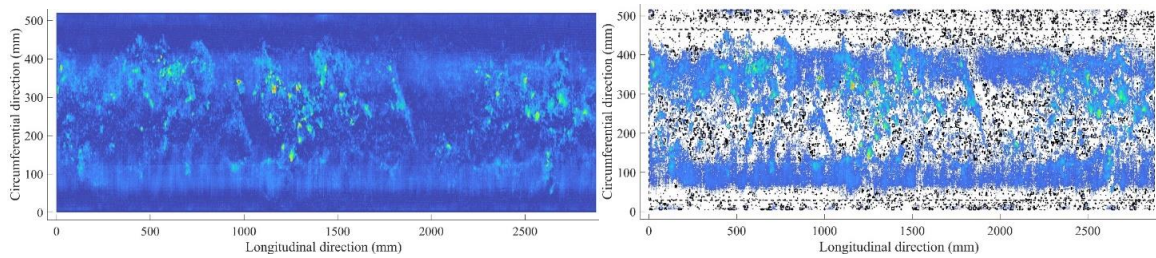
b) 3D image

Figure 2.1 2D and 3D images of the scanned surface of specimen 16-1

2.3 Corrosion anomaly and cluster identification

2.3.1 Anomaly identification with different depth thresholds

Figure 2.2 shows the corrosion anomalies identified on the external surface of specimen 16-1 after different depth thresholds (d_{th}) are used to remove the shallow corrosions, i.e. the corrosion depths are set to zero if they are less than the threshold value. The original scan results (i.e. without imposing d_{th}) is also shown in Fig. 2.2 as a reference. It is observed from Fig. 2.2 that, a higher depth threshold leads to fewer corrosion anomalies identified on the external surface: a total of 8016, 4613, 1069, 352 and 127 corrosion anomalies are identified within the scanned area, corresponding to $d_{th} = 2\%t$, $5\%t$, $10\%t$, $15\%t$ and $20\%t$, respectively. Figure 2.2 also indicates that a higher value of d_{th} leads to smaller corrosion anomalies. For example, the longest corrosion anomaly on specimen 16-1 is 2880, 334, 124, 32 and 24 mm long corresponding to $d_{th} = 2\%t$, $5\%t$, $10\%t$, $15\%t$ and $20\%t$, respectively.

a) Original scan result (i.e. without imposing d_{th})b) $d_{th} = 2\%t$

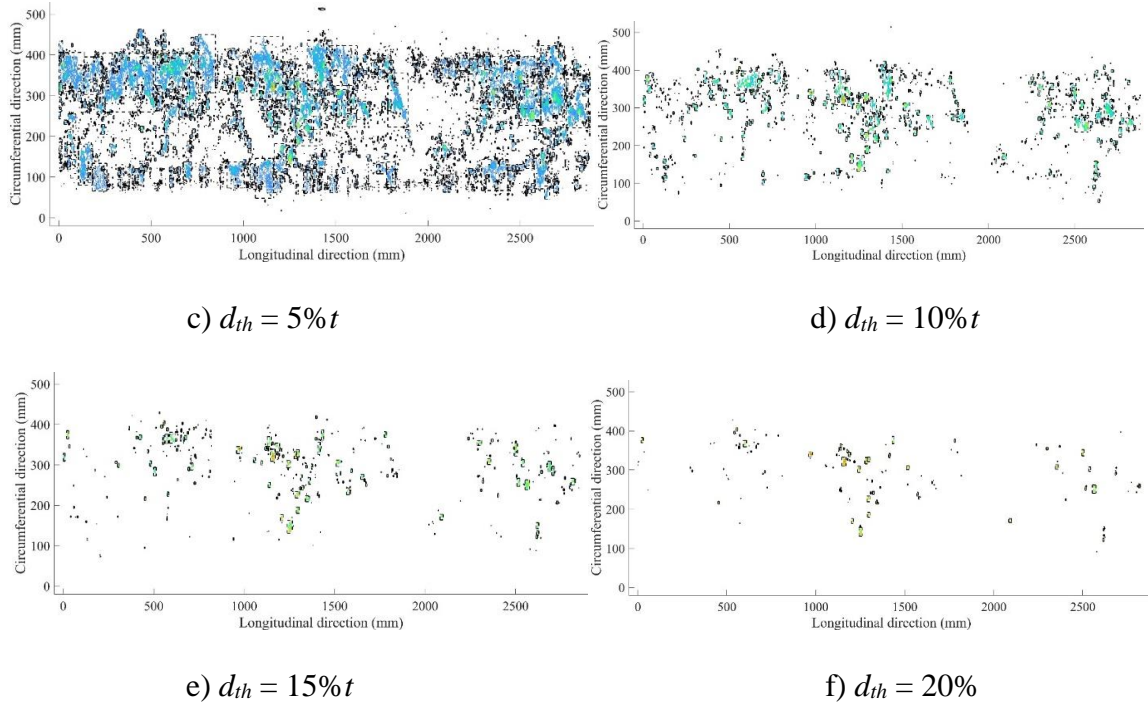


Figure 2.2 Corrosion anomalies on specimen 16-1 after applying the different depth thresholds

2.3.2 Interaction rules

Currently, most interaction rules are expressed in the following form (Benjamin et al 2016a,b):

$$s_l \leq (s_l)_{lim} \text{ and } s_c \leq (s_c)_{lim} \quad (2.1)$$

As illustrated in Fig. 2.3, two anomalies are combined into one corrosion cluster if their longitudinal separation distance s_l is less than or equal to the longitudinal interaction limit $(s_l)_{lim}$ and their circumferential separation distance s_c is less than or equal to the circumferential limit value $(s_c)_{lim}$. A corrosion cluster is defined as an area on the pipe surface with the sides parallel to the longitudinal and circumferential directions of the pipe, respectively (see Fig. 2.3). In this paper, five commonly used interaction rules are considered; the definitions of interaction limits in the five rules are summarized in Table 2.2. The $(s_l)_{lim}$ and $(s_c)_{lim}$ in DNV rule depend on the pipe diameter and wall thickness, whereas the Coulson and Worthingham (CW) rule assumes that the interaction limits are related to the lengths and widths of the two neighbouring anomalies. The CSA and B31G

rules are commonly known as the 6WT (i.e. six wall thicknesses) and 3WT rules, respectively, as their interaction limits in both directions are equal to $6t$ and $3t$, respectively. The B31.4 rule assumes that the longitudinal interaction limit is equal to a fixed value of 25.4 mm (1 in), and the circumferential limit equals $6t$; therefore the B31.4 rule is also known as the 1 in \times $6t$ rule.

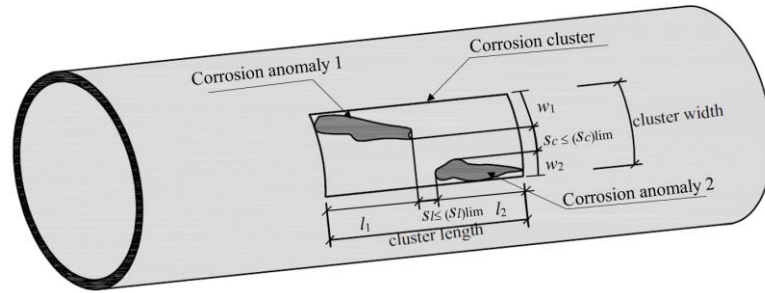


Figure 2.3 Illustration of the interaction rule and interaction limits

Table 2.2 Interaction limits for five commonly used interaction rules

Interaction limit	DNV	CW	CSA (6WT)	B31G (3WT)	B31.4
$(s_l)_{lim}$	$2\sqrt{Dt}$	$\min(l_1, l_2)$	$6t$	$3t$	25.4 mm
$(s_c)_{lim}$	$\pi\sqrt{Dt}$	$\min(w_1, w_2)$	$6t$	$3t$	$6t$

Note: l_1 and l_2 = lengths of two anomalies in close proximity; w_1 and w_2 = widths of two anomalies.

2.4 Methodologies

2.4.1 General

Although FEA predicts the burst capacity of corroded pipe segments with a high accuracy (see section 2.4.3), RSTRENG is a widely-used FFS assessment model in the pipeline industry. Therefore, we employ both FEA and RSTRENG to investigate the impacts of different depth thresholds and interaction rules on the predicted burst capacities. Five values of the depth threshold are considered: $d_{th} = 2\%t$, $5\%t$, $10\%t$, $15\%t$ and $20\%t$, respectively. For a given value of d_{th} , the corrosion data within the scanned area are modified such that the measured corrosion depths smaller than d_{th} are ignored and set to zero. The burst capacities corresponding to the modified corrosion data are then evaluated by FEA and RSTRENG, and compared with the capacities corresponding to the original

corrosion data. The results of the comparison quantify the impact of d_{th} and provide the basis for selecting a suitable d_{th} for identifying individual corrosion anomalies and clusters. To study the effectiveness of interaction rules, the significant corrosion areas on the 14 pipe specimens described in Section 2.2 are identified. A suitable d_{th} as identified in the analysis described in the previous paragraph is then applied to the corrosion areas to facilitate the identification of corrosion anomalies. The interaction rules listed in Table 2.2 are subsequently applied to the identified individual corrosion anomalies to generate the corrosion clusters. For each of the significant corrosion areas on the pipe specimens, FEA and RSTRENG are employed to evaluate the burst capacities of the entire area as well as the corrosion clusters within the areas identified based on different interaction rules. The effectiveness of interaction rules is then investigated by comparing the burst capacity of the clusters with that of the corresponding corrosion area.

2.4.2 FEA model

The FEA models are generated and analyzed in the commercial software ANSYS (version 16.1). The finite-strain, elasto-plastic formulation is employed to address the geometric and material nonlinearity in the burst capacity evaluation, and the von Mises yield criterion with the associated flow rule and isotropic hardening assumption are adopted in the material model.

The true stress (σ) - strain (ε) curve of the pipe specimen is fitted by the power-law relationship based on coupon tensile test results as follows:

$$\begin{cases} \sigma = E\varepsilon & \sigma < \sigma_y \\ \sigma = K\varepsilon^n & \sigma \geq \sigma_y \end{cases} \quad (2.2)$$

The values of n and K in Eq. (2.2) are evaluated by (Zhu and Leis 2005).

$$n = 0.224 \left(\frac{\sigma_u}{\sigma_y} - 1 \right)^{0.604} \quad (2.3)$$

$$K = \frac{\sigma_u e^n}{n^n} \quad (2.4)$$

where e is the base of natural logarithm with σ_y and σ_u presented in Table 2.1. Figure 2.4 compares the actual σ - ε curves (converted from the engineering stress- strain curve) of two representative specimens, 16-1 and 24-1, with those fitted using Eq. (2.2), which shows that Eq. (2.2) describes the true stress-strain relationship very well.

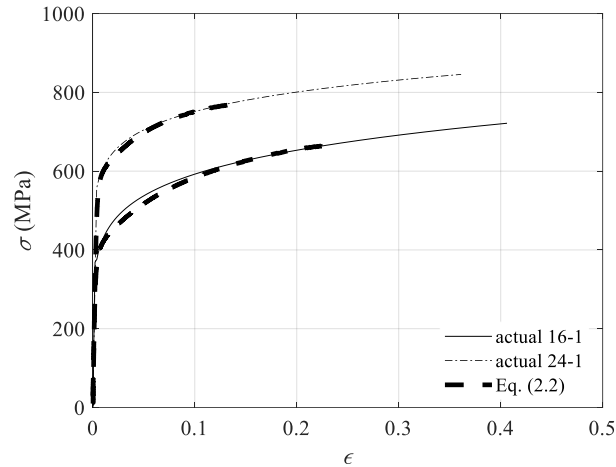


Figure 2.4 Comparison between the actual true stress - strain curves with the fitted ones for specimens 16-1 and 24-1

Because the scanned surfaces (see Table 2.1) and significant corrosion areas (see Fig. 2.8) on the 14 pipe specimens are large, it will be extremely time-consuming to carry out FEA of the pipe specimens with the resolution of the mesh the same as the scan resolution, i.e. one grid point corresponding to one node in FEA. The strategy of generating simplified FEA models proposed by Bao et al. (2018) is employed to develop FEA meshes that strike a balance between accuracy and computational efficiency. More specifically, the geometry of the corrosion regions is input in the FEA model based on a 10×10 mm grid. In other words, the mesh density of the corrosion region in the FEA model is 10×10 mm. Figure 2.5 illustrates how the corrosion geometry obtained from the LPIT laser scan with a 2×1 mm grid is input into the FEA model. In Fig. 2.5, the dashed lines are the grid lines of the laser scan, whereas the solid lines represent the FEA mesh. The corrosion depths at FEA mesh points 1, 2, 3 and 4 are taken as the maximum corrosion depths of the shaded areas centered by these four points, respectively.

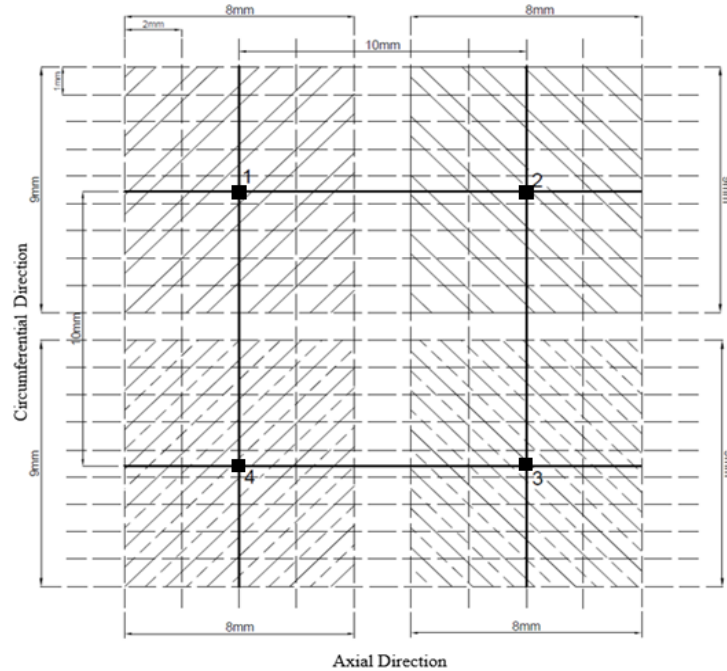
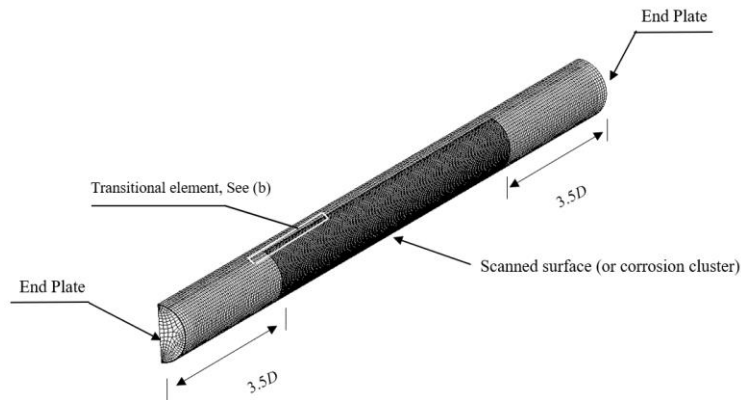


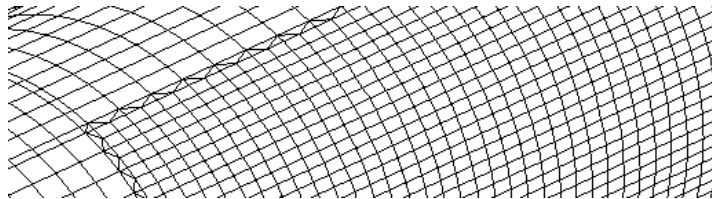
Figure 2.5 Finite element generation strategy in the corrosion region

As an illustration, the configuration of the FEA model containing the scanned corroded surface of specimen 16-1 is depicted in Fig. 2.6(a). The FEA model consists mainly of 8-node brick (C3D8) elements, and the prismatic (C3D6) element is used as the transitional element (see Fig. 2.6(b)). A half pipe model is built, which assumes that the two identical circumferentially aligned corrosion areas contained in the corresponding full-scale model do not interact with each other. This assumption is justified because their circumferential separation distance is large, which eliminates the potential for interaction. Accordingly, the half pipe model has the same burst capacity as the corresponding full pipe model but can be analyzed more efficiently (Bao et al. 2018). The FEA model is extended $3.5D$ longitudinally from each boundary of the corrosion region to eliminate the end effect. As explained in the above, the element size in the corrosion region is 10×10 mm, and a relatively coarser mesh (i.e. 20×20 mm) is used for the corrosion free areas outside the corrosion region. The FEA model in Fig. 2.6 consists of around 100,000 nodes and 80,000 elements. The mesh convergence studies regarding the possible shear locking along the thickness direction and the high stress gradient within the corrosion region have been performed to ensure the accuracy of the numerical results. Based on the convergence study,

four layers of elements along the thickness direction are used in both the corrosion region and the areas outside the corrosion region.



a) Configuration of the FEA model



b) Transitional element

Figure 2.6 FEA model of pipe segment containing the scan surface of specimen 16-1

The burst of a pipe segment involves the fracture of the remaining ligament, which cannot be simulated due to the continuum constitutive model employed in FEA. The failure criterion adopted in this study is that burst failure occurs when the von Mises stress of any node in the corrosion region reaches the true stress corresponding to the ultimate tensile strength.

2.4.3 FEA validation

In Fig. 2.7, the burst capacities of the 14 pipe specimens are determined by FEA and compared with those observed in the tests. Let P_{test} and P_{FEA} denote the burst capacities observed in the tests and determined by FEA, respectively. The mean and coefficient of variation (COV) of the test-to-FEA predicted ratios (P_{test}/P_{FEA}) are 0.97 and 6.5%, respectively. It should be mentioned that large discrepancies between P_{test} and P_{FEA} are observed for specimens 16-2 and 16-3. These two tests were paused due to the equipment malfunction when the internal pressures nearly reached the final burst levels. The internal

pressures were maintained during the pause while the malfunctioning equipment was replaced, and the tests were resumed after the pause. The short suspension at a high stress level may cause the growth of micro cracks in the corroded region, which reduces the burst capacities of the specimens and results in relatively large discrepancies between the FEA-predicted and tested capacities. By excluding these two tests, the mean and COV of test-to-predicted ratios are 0.99 and 4.4%, respectively. The comparisons demonstrate the accuracy of FEA in the burst capacity prediction of pipe segments containing naturally-occurring corrosion anomalies.

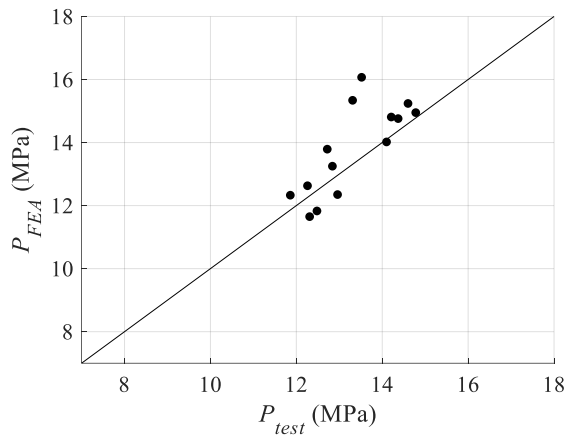


Figure 2.7 Comparison between the test-based and FEA-predicted burst capacities of the 14 specimens

2.4.4 RSTRENG model

As shown in Fig. 2.8, the RSTRENG model characterizes the 3D corrosion features by the river-bottom path, which passes through the deepest corroded points on different circumferential planes. The river bottom path is then projected onto a longitudinal plane that is perpendicular to the wall thickness to generate the river bottom profile. The corrosion feature is divided into n sub-features with each sub feature occupying a contiguous portion of the river bottom profile. The burst pressure of the i^{th} sub-feature, $P_{RST,i}$, can be calculated with the following equation:

$$P_{RST,i} = (\sigma_y + 68.95) \frac{1 - \frac{A_i}{l_i t}}{1 - \frac{A_i}{M_i l_i t}} \frac{d_{max}}{t} \leq 0.8 \quad (2.5)$$

where A_i and l_i are, respectively, the corroded area and the length of the i^{th} sub-feature on the river bottom profile. The bulging factor M_i is given by

$$M_i = \begin{cases} \sqrt{1 + 0.6275 \frac{l_i^2}{Dt} - 0.003375 \frac{l_i^4}{(Dt)^2}} & \frac{l_i^2}{Dt} \leq 50 \\ 3.3 + 0.032 \frac{l_i^2}{Dt} & \frac{l_i^2}{Dt} > 50 \end{cases} \quad (2.6)$$

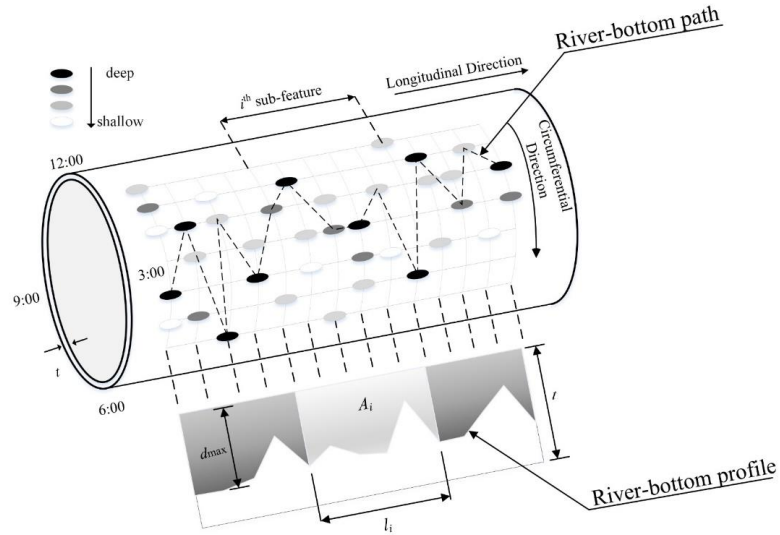


Figure 2.8 Illustration of the river bottom path and river bottom profile of a naturally occurring corrosion feature

The burst capacity (P_{RST}) of the corrosion feature is then determined as the minimum value of the burst capacities of all the sub-features, i.e.

$$P_{RST} = \min\{P_{RST,i}\} \quad i = 1, 2, \dots, n \quad (2.7)$$

2.5 Results and Discussions

2.5.1 Impact of depth threshold

Tables 2.3 and 2.4 list the burst pressures predicted by using FEA, $P_{FEA}(d_{th})$, and RSTRENG model, $P_{RST}(d_{th})$, after applying different depth thresholds. As expected, the increase in the threshold value leads to a higher predicted burst capacity. Let P_{FEA} and P_{RST} denote the FEA-predicted and RSTRENG-predicted burst capacities without imposing d_{th} . The percentage increase of the FEA prediction, $\varepsilon_{FEA}(d_{th}) = |P_{FEA}(d_{th}) - P_{FEA}|/P_{FEA}$, and RSTRENG prediction, $\varepsilon_{RST}(d_{th}) = |P_{RST}(d_{th}) - P_{RST}|/P_{RST}$, corresponding to different d_{th} values are also calculated. Tables 2.3 and 2.4 show that imposing $d_{th} = 10\%t$ has a

negligible impact on the burst capacities predicted by both FEA and RSTRENG: the increase in the burst capacities of the 14 specimens after imposing $d_{th} = 10\%t$ is generally less than 2%. On the other hand, a depth threshold of $15\%t$ ($20\%t$) can result in the predicted burst capacities about 5% (10%) higher than that without imposing d_{th} . Thus, $d_{th} = 10\%t$ is recommended based on the above results. A comparison between Tables 2.3 and 2.4 indicate that the FEA-predicted burst capacity is more sensitive to the application of d_{th} than the RSTRENG-predicted burst capacity. This can be attributed to that FEA takes into account the three-dimensional corrosion geometry, while the river-bottom profile considered in RSTRENG is two-dimensional.

Table 2.3 Impact of the depth threshold on the predicted burst capacity based on FEA

Specimen ID	P_{FEA} (MPa)	$P_{FEA}(d_{th})$ (MPa)					$\varepsilon_{FEA}(d_{th})$ (%)				
		2	5	10	15	20	2	5	10	15	20
16-1	15.24	15.25	15.29	15.50	15.84	16.24	0.0	0.3	1.7	3.9	6.5
16-2	15.34	15.34	15.40	15.77	16.03	16.28	0.0	0.4	2.8	4.5	6.1
16-3	16.07	16.08	16.17	16.48	16.87	17.03	0.1	0.6	2.5	5.0	6.0
16-5	12.33	12.33	12.42	12.55	12.59	12.64	0.0	0.8	1.8	2.1	2.5
16-6	13.79	13.80	13.91	13.99	14.07	14.27	0.1	0.9	1.4	2.0	3.4
16-7	13.25	13.28	13.46	13.58	13.67	13.70	0.2	1.5	2.5	3.1	3.4
24-1	14.81	14.81	14.83	14.94	15.26	15.96	0.0	0.2	0.9	3.0	7.8
24-2	14.76	14.76	14.79	15.03	15.45	15.95	0.0	0.2	1.9	4.7	8.1
30-1	11.65	11.65	11.67	11.73	11.85	12.16	0.0	0.2	0.7	1.7	4.4
30-2	14.02	14.02	14.05	14.12	14.37	14.76	0.0	0.2	0.7	2.5	5.3
30-3	14.95	14.95	14.99	15.29	15.43	15.59	0.0	0.3	2.3	3.2	4.3
30-4	11.83	11.83	11.83	12.05	12.32	12.59	0.0	0.0	1.8	4.1	6.4
30-5	12.63	12.63	12.66	12.83	13.17	13.69	0.0	0.3	1.6	4.3	8.4
30-6	12.35	12.36	12.39	12.61	12.85	13.25	0.0	0.3	2.1	4.0	7.3
Mean							0.0	0.4	1.8	3.4	5.7

Table 2.4 Impact of the depth threshold on the predicted burst capacity based on the RSTRENG

Specimen ID	P_{RST} (MPa)	$P_{RST}(d_{th})$ (MPa)					$\varepsilon_{RST}(d_{th})$ (%)				
		2	5	10	15	20	2	5	10	15	20
16-1	10.72	10.72	10.72	10.75	10.82	11.10	0.0	0.0	0.3	1.0	3.6
16-2	10.77	10.77	10.77	10.78	11.00	11.31	0.0	0.0	0.1	2.1	5.0
16-3	11.22	11.22	11.22	11.32	11.72	12.11	0.0	0.0	0.9	4.4	7.9
16-5	8.02	8.02	8.02	8.02	8.02	8.02	0.0	0.0	0.0	0.0	0.0
16-6	9.00	9.00	9.00	9.00	9.00	9.00	0.0	0.0	0.0	0.0	0.0
16-7	9.39	9.39	9.39	9.42	9.57	9.60	0.0	0.0	0.2	1.9	2.2
24-1	11.50	11.50	11.50	11.50	11.66	12.33	0.0	0.0	0.0	1.4	7.2
24-2	11.49	11.49	11.49	11.52	11.95	12.61	0.0	0.0	0.3	4.1	9.7
30-1	8.64	8.64	8.64	8.64	8.64	8.64	0.0	0.0	0.0	0.0	0.0
30-2	11.09	11.09	11.09	11.14	11.42	12.14	0.0	0.0	0.4	3.0	9.5
30-3	11.66	11.66	11.66	11.69	12.00	12.29	0.0	0.0	0.3	2.9	5.4
30-4	10.57	10.57	10.57	10.58	10.63	10.85	0.0	0.0	0.1	0.6	2.6
30-5	10.58	10.58	10.58	10.66	10.77	10.83	0.0	0.0	0.7	1.8	2.3
30-6	10.07	10.07	10.07	10.13	10.42	10.83	0.0	0.0	0.5	3.4	7.5
Mean							0.0	0.0	0.3	1.9	4.5

2.5.2 Impact of interaction rules

Based on the depth threshold analysis described in the previous section, $d_{th} = 10\%t$ is employed in this study to remove the background corrosions on the external surfaces of the 14 specimens. Individual corrosion anomalies on the specimens are subsequently extracted. A total of 54 significant corrosion areas (designated as CA# in Fig. 2.9 and Fig. A.1 of Appendix A) are identified from the 14 specimens. The five interaction rules listed in Table 2.2 are used to combine the closely spaced corrosion anomalies within each of these areas into corrosion clusters. Since a given corrosion area usually contains multiple clusters, the cluster with the lowest burst capacity evaluated using a given approach (i.e. either FEA or RSTRENG) within the area is defined as the critical cluster corresponding to the area. As an illustration, the critical corrosion clusters generated according to the 5 interaction rules within the 6 corroded areas on specimen 16-1 are depicted in different colors in Fig. 2.9. The critical clusters on the other 13 specimens are depicted in Fig. A.1 of Appendix A. Given the corrosion area and interaction rule, the critical cluster identified based on FEA is the same as that identified based on RSTRENG for all 54 corrosion areas and five interaction rules, although the burst capacity of the critical cluster evaluated using FEA differs from that evaluated using RSTRENG.

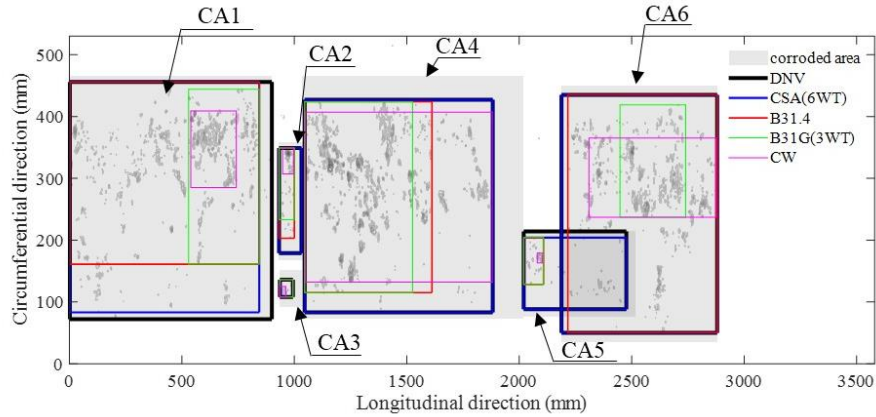
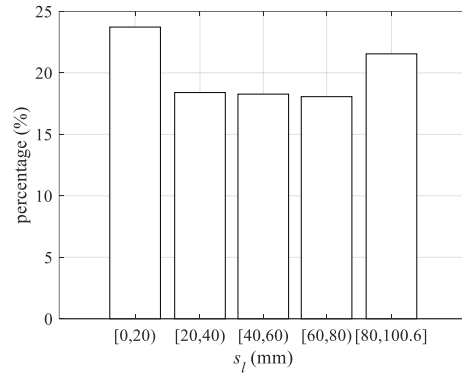
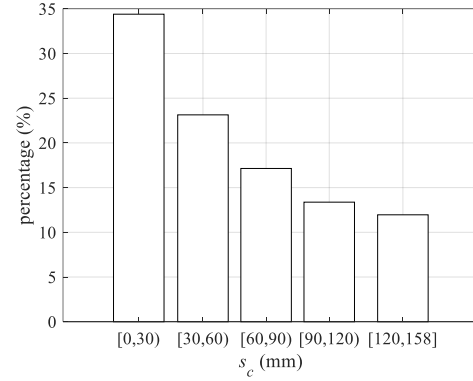
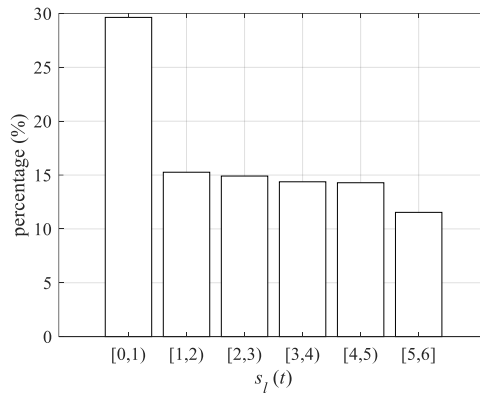
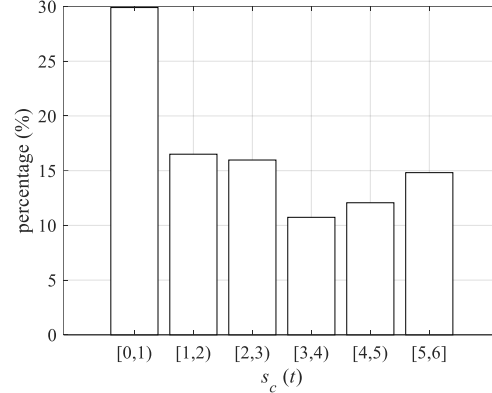
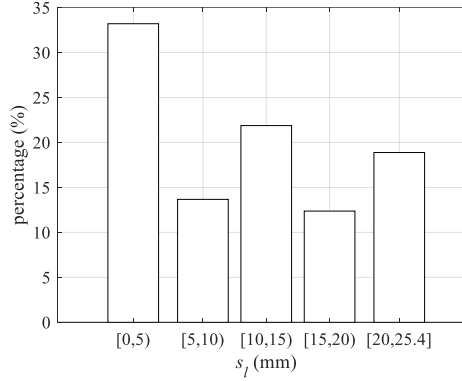
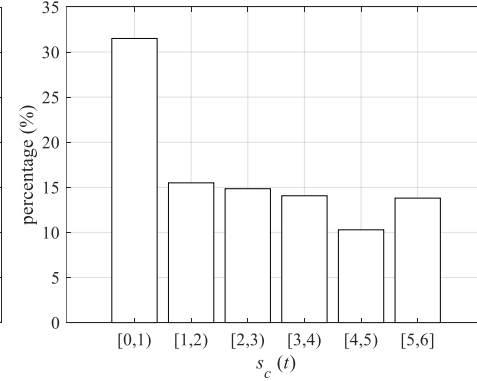
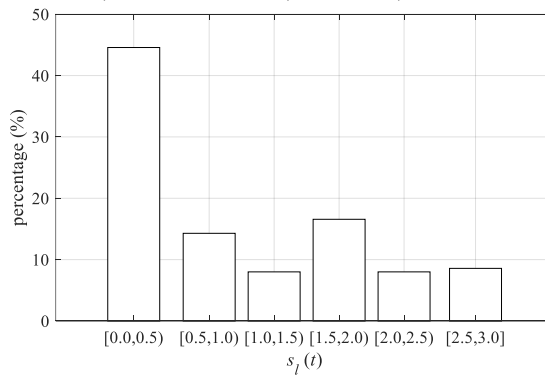
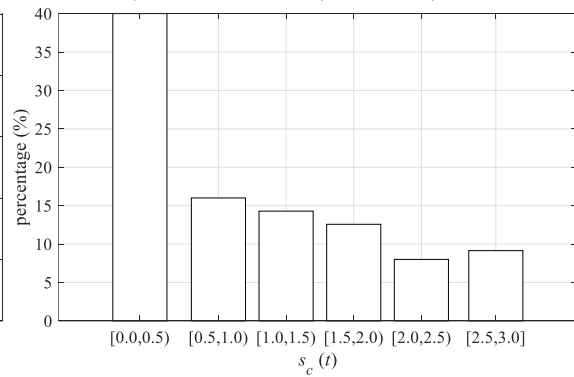


Figure 2.9 Corroded areas on specimen 16-1 and critical corrosion clusters identified based on different interaction rules

The critical corrosion cluster generated by using the DNV rule within CA1 as shown in Fig. 2.9 is 898 mm long and 386 mm wide, and contains 368 corrosion anomalies. According to the interaction limits of DNV rule listed in Table 2.2, these 368 corrosion anomalies result in 6289 pairs of interacting corrosion anomalies. Figures 2.10(a) and 2.10(b) summarize the longitudinal, s_l , and circumferential spacing, s_c , of each of the 6289 interacting anomaly pairs. Similarly, the distribution of s_l and s_c in the critical corrosion clusters generated according to the other four interaction rules are also shown in Fig. 2.10. Figure 2.10 indicates that the values of s_l and s_c between pairs of interacting corrosion anomalies within a given cluster cover the ranges of possible values of s_l and s_c , i.e. $0 \leq s_l \leq (s_l)_{lim}$ and $0 \leq s_c \leq (s_c)_{lim}$. Similar results are also observed for CA2 through CA54, although for brevity these results are not shown. This suggests that the dataset used in the present study is suitable and balanced to investigate the effectiveness of the interaction rules for naturally-occurring corrosion anomalies.

a) s_l for DNV ruleb) s_c for DNV rulec) s_l for CSA (6WT) ruled) s_c for CSA (6WT) rulee) s_l for B31.4 (1 in \times 6t) rulef) s_c for B31.4 (1 in \times 6t) ruleg) s_l for B31G (3WT) ruleh) s_c for B31G (3WT) rule

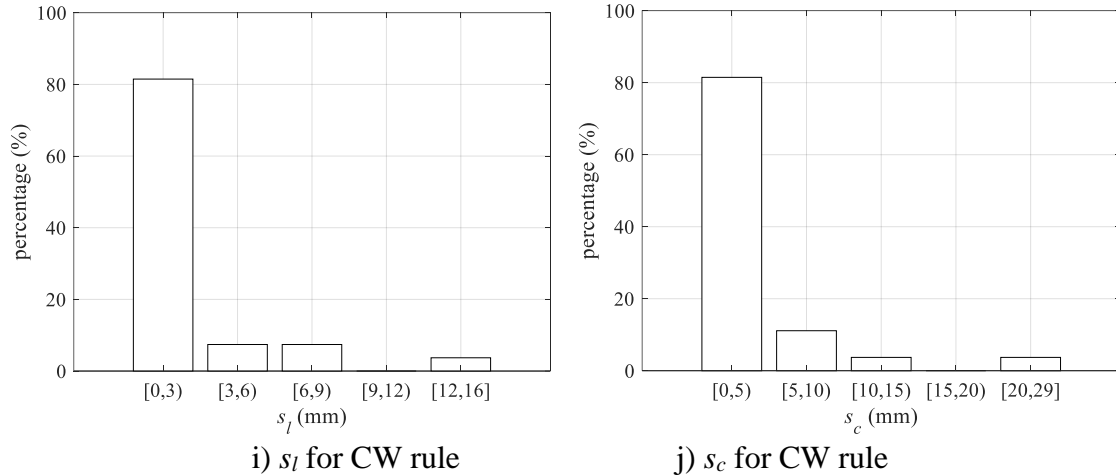


Figure 2.10 Distribution of longitudinal and circumferential separation distances between interacting corrosion anomalies in CA1 in terms of different interaction rules

Figure 2.9 and Appendix A compare the sizes of the critical corrosion clusters on the 54 significant corrosion areas resulting from different interaction rules. Among them, the DNV rule is the most stringent interaction rule and results in the largest critical clusters, often as large as the corrosion area, whereas the CW rule is usually the least stringent rule and results in the smallest critical corrosion clusters.

The burst capacities of the critical corrosion clusters within the 54 significant corrosion areas are predicted by FEA. Let P_{FEA-b} denote the burst capacity of the corrosion area predicted by FEA, and let $P_{FEA-\bullet}$ denote the FEA-predicted burst capacities of the critical corrosion clusters within the area generated according to interaction rule \bullet . Define $e_{FEA-\bullet} = |P_{FEA-\bullet} - P_{FEA-b}| / P_{FEA-b}$. Table 2.5 summarizes the values of P_{FEA-b} , $P_{FEA-\bullet}$ and $e_{FEA-\bullet}$ for the 54 corroded areas. Similarly, the burst capacities of the corrosion area and critical corrosion cluster within the area are also evaluated using RSTRENG, denoted by P_{RST-b} and $P_{RST-\bullet}$, respectively. Table 2.6 summarizes the values of P_{RST-b} , $P_{RST-\bullet}$ and $e_{RST-\bullet} = |P_{RST-\bullet} - P_{RST-b}| / P_{RST-b}$.

Tables 2.5 and 2.6 reveal that the burst capacities of the critical corrosion clusters based on the CW and B31G (3WT) rules can be 5% higher than the burst capacity of the

corresponding corrosion area, while the burst capacities of the critical clusters based on the DNV and CSA (6WT) rules differ by less than 2% from burst capacities of the corresponding corrosion areas. The burst capacity of the critical cluster based on the B31.4 rule is on average also close to the burst capacity of the corroded area, although in a few cases the difference can be as large as 3-4%. Tables 2.5 and 2.6 suggest that the CSA (6WT) rule results in critical clusters that accurately capture the most critical regions of the corrosion area. The use of the B31G (3WT) and CW rules may lead to non-conservative critical clusters as their burst capacities can be 5% higher than the burst capacity of the corrosion areas. Although the DNV rule results in similar burst capacities of critical clusters as the CSA (6WT) rule, the large $(s_l)_{lim}$ and $(s_c)_{lim}$ values associated with the DNV rule generally result in large corrosion clusters that are time-consuming to identify and analyze. Therefore, the DNV rule is considered unamenable for practical application.

Table 2.5 Impact of the interaction rule on the FEA-predicted burst capacities

Corroded Area	P_{FEA-b} (MPa)	Burst capacity of critical cluster (MPa)						Relative difference (%)				
		P_{FEA-}	P_{FEA-}	P_{FEA-}	P_{FEA-}	P_{FEA-}	e_{FEA}	e_{FEA}	e_{FEA-}	e_{FEA-}	e_{FEA-}	
		DNV	CSA	B31.4	B31G	CW	-DNV	-CSA	B31.4	B31G	CW	
CA1	16.2	16.2	16.2	16.2	16.4	16.6	0.00	0.00	0.00	1.11	2.64	
CA2	16.9	16.9	16.9	17.3	17.4	17.6	0.00	0.00	2.21	2.80	3.68	
CA3	17.5	17.5	17.5	17.5	17.5	17.5	0.00	0.00	0.00	0.00	0.00	
CA4	15.7	15.7	15.7	15.7	15.7	15.8	0.00	0.00	0.00	0.00	0.67	
CA5	17.4	17.4	17.4	17.5	17.5	17.8	0.10	0.10	0.95	0.95	2.68	
CA6	16.5	16.5	16.5	16.5	16.6	16.7	0.00	0.00	0.29	0.89	1.38	
CA7	15.7	15.7	15.7	15.9	15.9	16.3	0.00	0.00	1.04	1.35	4.04	
CA8	16.9	17.0	17.0	17.3	17.3	17.1	0.24	0.24	2.01	2.48	1.07	
CA9	17.4	17.4	17.4	17.4	17.5	17.5	0.05	0.19	0.19	0.35	0.35	
CA10	17.5	17.6	17.6	17.6	17.6	17.6	0.52	0.53	0.53	0.53	0.53	
CA11	16.5	16.6	16.7	16.7	16.8	17.1	0.34	0.94	1.17	1.78	3.87	
CA12	17.3	17.4	17.4	17.5	17.5	17.6	1.04	1.04	1.23	1.29	1.76	
CA13	17.0	17.0	17.0	17.1	17.1	17.3	0.06	0.06	0.14	0.18	1.41	
CA14	17.0	17.1	17.2	17.2	17.4	17.4	0.43	0.87	0.87	2.23	2.23	
CA15	15.2	15.3	15.3	15.3	15.4	15.4	0.20	0.20	0.33	1.25	1.25	
CA16	17.1	17.3	17.3	17.3	17.4	17.4	1.14	1.14	1.14	1.81	2.08	
CA17	12.9	12.9	12.9	12.9	12.9	12.9	0.00	0.33	0.41	0.41	0.00	
CA18	17.3	17.4	17.4	17.4	17.4	17.4	0.32	0.49	0.49	0.49	0.49	
CA19	16.5	16.6	16.6	16.6	16.6	16.6	0.61	0.61	0.61	0.61	0.61	
CA20	16.9	16.9	16.9	16.9	17.1	17.2	0.13	0.13	0.14	1.36	2.03	
CA21	16.6	16.6	16.6	16.6	16.6	16.7	0.22	0.22	0.22	0.22	0.32	
CA22	14.4	14.7	14.7	14.7	14.9	14.9	1.80	1.80	1.80	3.19	3.19	
CA23	18.0	18.1	18.1	18.1	18.1	18.3	0.13	0.13	0.46	0.48	1.58	
CA24	17.9	18.0	18.0	18.1	18.1	18.1	0.73	0.73	1.16	1.16	1.56	
CA25	15.5	15.5	15.5	15.5	15.7	15.7	0.00	0.00	0.00	1.29	1.29	
CA26	18.1	18.1	18.1	18.1	18.1	18.3	0.05	0.05	0.05	0.05	1.15	

(continued on next page)

Table 2.5 (Continued)

Corroded Area	P_{FEA-b} (MPa)	Burst capacity of critical cluster (MPa)					Relative difference (%)				
		P_{FEA-}	P_{FEA-}	P_{FEA-}	P_{FEA-}	P_{FEA-}	e_{FEA}	e_{FEA}	e_{FEA-}	e_{FEA-}	e_{FEA-}
		DNV	CSA	B31.4	B31G	CW	-DNV	-CSA	B31.4	B31G	CW
CA27	14.1	14.1	14.1	14.1	14.1	14.1	0.58	0.58	0.58	0.58	0.58
CA28	18.1	18.1	18.1	18.1	18.1	18.1	0.00	0.00	0.00	0.00	0.01
CA29	17.9	17.9	17.9	17.9	18.0	18.1	0.00	0.00	0.25	0.50	1.44
CA30	17.9	18.0	18.0	18.0	18.1	18.1	0.53	0.53	0.53	1.10	1.10
CA31	17.7	17.7	17.7	17.8	17.8	18.3	0.00	0.00	0.48	0.76	3.25
CA32	13.8	13.8	14.0	14.4	14.5	14.0	0.00	1.30	4.61	5.12	1.32
CA33	15.7	15.8	15.8	15.8	15.8	15.8	0.54	0.54	0.54	0.66	0.94
CA34	16.5	16.6	16.7	16.7	16.8	16.8	0.16	0.73	0.73	1.33	1.33
CA35	16.5	16.5	16.5	16.5	16.5	16.7	0.02	0.09	0.27	0.27	1.50
CA36	14.9	14.9	14.9	14.9	14.9	14.9	0.05	0.11	0.13	0.14	0.21
CA37	16.4	16.4	16.4	16.4	16.4	16.4	0.03	0.09	0.15	0.18	0.24
CA38	16.4	16.4	16.4	16.4	16.4	16.4	0.29	0.33	0.34	0.34	0.40
CA39	15.8	15.8	15.9	15.9	16.0	16.1	0.10	0.75	1.11	1.30	2.52
CA40	15.0	15.0	15.0	15.1	15.2	15.7	0.06	0.22	0.47	1.48	4.84
CA41	14.9	15.0	15.1	15.2	15.2	15.2	0.88	1.54	2.19	2.34	2.34
CA42	14.7	14.7	14.7	14.7	14.8	14.8	0.10	0.13	0.17	0.26	0.27
CA43	14.9	14.9	14.9	15.3	15.3	15.5	0.00	0.01	2.96	2.99	4.19
CA44	11.6	11.7	11.7	11.7	11.8	11.8	0.66	0.66	0.77	1.46	1.59
CA45	14.3	14.3	14.3	14.3	14.3	14.3	0.16	0.16	0.17	0.23	0.25
CA46	15.6	15.7	15.8	15.8	16.0	16.1	0.49	1.11	1.23	2.63	3.30
CA47	15.2	15.3	15.3	15.3	15.3	15.3	0.26	0.26	0.29	0.29	0.54
CA48	15.8	15.9	15.9	15.9	15.9	16.3	0.81	0.81	0.90	0.90	3.04
CA49	12.1	12.1	12.1	12.2	12.2	12.5	0.01	0.06	0.68	0.83	2.83
CA50	14.3	14.3	14.3	14.3	14.3	14.4	0.20	0.24	0.32	0.32	1.26
CA51	12.9	12.9	13.0	13.0	13.0	13.6	0.13	0.80	0.81	0.89	5.77
CA52	13.0	13.1	13.2	13.3	13.3	13.7	0.39	1.04	2.36	2.36	5.04
CA53	13.4	13.4	13.4	13.6	13.7	13.5	0.04	0.04	1.71	2.21	0.66
CA54	12.6	12.7	12.7	12.7	13.0	13.1	0.52	0.52	0.81	3.07	4.20
Mean							0.28	0.42	0.80	1.16	1.79
Maximum							1.80	1.80	4.61	5.12	5.77

Table 2.6 Impact of the interaction rule on the RSTRENG-predicted burst capacities

Corroded Area	P_{RST-b} (MPa)	Burst capacity of critical cluster (MPa)					Relative difference (%)				
		P_{RST-}	P_{RST-}	P_{RST-}	P_{RST-}	P_{RST-}	e_{RST}	e_{RST}	e_{RST}	e_{RST}	e_{RST}
		DNV	CSA	B31.4	B31G	CW	DNV	CSA	B31.4	B31G	CW
CA1	11.3	11.3	11.3	11.3	11.3	11.4	0.00	0.00	0.08	0.12	0.41
CA2	12.4	12.5	12.5	12.5	12.5	12.7	0.03	0.03	0.33	0.33	1.65
CA3	12.9	13.0	13.0	13.0	13.0	13.2	0.17	0.17	0.17	0.17	1.79
CA4	10.7	10.7	10.7	10.7	10.7	10.7	0.00	0.00	0.00	0.00	0.00
CA5	12.6	12.6	12.6	12.6	12.6	13.1	0.05	0.05	0.09	0.09	3.99
CA6	11.4	11.4	11.4	11.4	11.6	11.6	0.00	0.00	0.00	1.53	2.12
CA7	10.8	10.8	10.8	10.8	10.8	11.1	0.00	0.00	0.33	0.33	2.65
CA8	11.9	11.9	11.9	12.2	12.3	12.4	0.00	0.00	2.66	2.69	3.56
CA9	12.2	12.2	12.2	12.2	12.3	12.3	0.00	0.00	0.00	0.24	0.24
CA10	12.7	12.7	12.8	12.8	13.0	13.2	0.03	0.27	0.27	2.25	3.55
CA11	11.3	11.3	11.4	11.7	11.7	11.8	0.00	0.59	3.19	3.66	3.98
CA12	12.5	12.5	12.5	12.5	12.7	12.9	0.00	0.00	0.00	1.15	3.33

(continued on next page)

Table 2.6 (Continued)

Corroded Area	P_{RST-b} (MPa)	Burst capacity of critical cluster (MPa)					Relative difference (%)				
		P_{RST-}	P_{RST-}	P_{RST-}	P_{RST-}	P_{RST-}	e_{RST-}	e_{RST-}	e_{RST-}	e_{RST-}	e_{RST-}
		DNV	CSA	B31.4	B31G	CW	DNV	CSA	B31.4	B31G	CW
CA13	12.3	12.3	12.3	12.3	12.3	12.6	0.00	0.00	0.00	0.23	2.74
CA14	12.6	12.6	12.6	12.6	12.8	12.8	0.09	0.19	0.19	1.30	1.30
CA15	10.3	10.3	10.3	10.3	10.6	10.6	0.00	0.04	0.04	2.48	2.48
CA16	12.7	12.7	12.7	12.7	12.7	12.8	0.06	0.06	0.06	0.28	0.73
CA17	8.0	8.0	8.0	8.0	8.0	8.0	0.00	0.00	0.00	0.00	0.00
CA18	12.7	12.7	12.7	12.7	12.7	12.7	0.14	0.48	0.48	0.48	0.48
CA19	11.8	11.8	11.8	11.8	11.8	11.8	0.01	0.01	0.01	0.01	0.17
CA20	12.1	12.1	12.1	12.1	12.2	12.5	0.00	0.00	0.00	0.43	3.42
CA21	11.6	11.6	11.6	11.6	11.6	11.6	0.00	0.00	0.00	0.00	0.00
CA22	9.0	9.0	9.0	9.0	9.0	9.0	0.00	0.00	0.00	0.00	0.00
CA23	13.4	13.4	13.4	13.4	13.5	13.8	0.07	0.07	0.19	1.29	2.93
CA24	13.0	13.0	13.0	13.0	13.0	13.5	0.04	0.04	0.04	0.04	3.46
CA25	10.5	10.5	10.5	10.5	10.5	10.5	0.00	0.00	0.00	0.02	0.02
CA26	13.5	13.6	13.6	13.6	13.6	13.7	0.09	0.28	0.28	0.28	1.32
CA27	10.1	10.1	10.1	10.1	10.1	10.1	0.00	0.00	0.00	0.00	0.00
CA28	13.4	13.4	13.4	13.4	13.4	13.4	0.12	0.12	0.12	0.12	0.12
CA29	13.1	13.1	13.1	13.1	13.1	13.3	0.00	0.00	0.00	0.03	0.88
CA30	12.9	12.9	12.9	12.9	13.0	13.0	0.05	0.05	0.05	0.86	0.86
CA31	12.6	12.6	12.6	12.7	12.7	12.9	0.00	0.00	0.62	0.88	2.04
CA32	9.4	9.4	9.4	9.6	9.6	9.5	0.00	0.00	1.65	1.65	0.99
CA33	12.1	12.1	12.1	12.1	12.1	12.1	0.00	0.00	0.00	0.20	0.26
CA34	13.3	13.3	13.3	13.3	13.4	13.4	0.01	0.34	0.34	1.13	1.13
CA35	13.3	13.3	13.3	13.3	13.3	13.6	0.03	0.03	0.05	0.05	2.41
CA36	11.5	11.5	11.5	11.5	11.5	11.5	0.00	0.00	0.00	0.00	0.00
CA37	13.1	13.1	13.2	13.4	13.4	13.6	0.00	0.55	2.47	2.28	3.46
CA38	13.0	13.0	13.1	13.1	13.1	13.5	0.02	0.18	0.21	0.21	3.64
CA39	12.1	12.1	12.1	12.2	12.3	13.0	0.00	0.00	0.02	1.49	7.27
CA40	11.5	11.5	11.5	11.5	11.6	12.1	0.00	0.00	0.00	0.87	4.90
CA41	11.6	11.6	11.6	11.6	11.6	11.7	0.00	0.02	0.18	0.18	0.30
CA42	11.9	11.9	11.9	11.9	11.9	11.9	0.00	0.00	0.00	0.00	0.09
CA43	12.3	12.3	12.3	12.5	12.5	12.6	0.00	0.55	2.18	2.18	2.51
CA44	8.6	8.6	8.6	8.6	8.6	8.6	0.00	0.00	0.00	0.00	0.00
CA45	11.1	11.1	11.1	11.1	11.2	11.2	0.00	0.00	0.00	0.94	0.94
CA46	12.6	12.6	12.6	12.6	13.0	13.2	0.00	0.00	0.01	2.91	4.48
CA47	11.7	11.7	11.7	11.7	11.7	12.3	0.00	0.00	0.00	0.00	5.50
CA48	13.4	13.4	13.4	13.4	13.4	13.6	0.02	0.02	0.04	0.04	1.28
CA49	10.6	10.6	10.6	10.6	10.6	10.6	0.00	0.00	0.00	0.00	0.00
CA50	12.4	12.4	12.4	12.4	12.4	12.4	0.00	0.00	0.00	0.00	0.00
CA51	10.7	10.7	10.7	10.7	10.7	11.1	0.00	0.00	0.00	0.00	4.03
CA52	10.7	10.7	10.7	10.7	10.7	10.8	0.00	0.00	0.00	0.00	0.99
CA53	11.5	11.5	11.5	11.5	11.5	11.5	0.00	0.00	0.23	0.23	0.00
CA54	11.0	11.0	11.0	11.0	11.3	11.2	0.00	0.00	0.04	2.26	1.15
Mean							0.02	0.08	0.31	0.70	1.77
Maximum							0.17	0.59	3.19	3.66	7.27

2.6 Conclusion

This chapter investigates the impact of the depth threshold and five commonly used interaction rules on the evaluation of burst capacities of naturally corroded pipelines based on 14 pipe specimens containing naturally occurring corrosion anomalies. The RSTRENG model and FEA are employed to evaluate the burst capacities of 14 pipe specimens containing naturally occurring corrosions. It is observed that applying a corrosion depth threshold of $10\%t$ to corroded pipe surface has a negligible (generally less than 2%) impact on the burst capacities predicted using FEA and RSTRENG, but can greatly facilitate the identification of individual corrosion anomalies and corrosion clusters.

The effectiveness of the DNV, CSA (i.e. 6WT), B31G (i.e. 3WT), B31.4 (i.e. $1 \text{ in} \times 6t$) and CW interaction rules is investigated based on the burst capacities of 54 groups of corrosion clusters identified from the 14 pipe specimens evaluated using the RSTRENG model and FEA. The burst capacities of the critical corrosion clusters identified using the DNV and CSA (6WT) rules differ from the burst capacity of the corresponding corroded areas by less than 2%, while the burst capacities of the critical clusters identified using the B31G (3WT) and CW interaction rules can be 5% higher than the burst capacity of the corresponding corrosion area. The DNV rule is considered unamenable for practice as it leads to large corrosion clusters, which are highly time-consuming to be analyzed. On the other hand, the critical corrosion cluster identified using the CSA (6WT) rule is smaller than the critical cluster identified using the DNV rule but still captures the critical corrosion region. Thus, the CSA (6WT) interaction rule is recommended for combining naturally occurring corrosion anomalies into corrosion clusters for practical fitness-for-service assessments of corroded pipelines.

References

- Al-Owaisi. S., Becker. A. A., Sun. W., Al-Shabibi. A., Al-Maharbi. M., Pervez. T. and Al-Salmi. H. 2018. An experimental investigation of the effect of defect shape and orientation on the burst pressure of pressurized pipes. *Engineering Failure Analysis*. 93: 200 - 213.

- ASME. 2016. Fitness-For-Service. API 579-1/ASME FFS-1. The American Society of Mechanical Engineers. New York, USA.
- ASME. 2018. Manual for determining the remaining strength of corroded pipelines. Supplement to ASME B31 code for pressure piping. ASME B31G - 2018. New York, USA.
- ASME. 2019. Pipeline transportation systems for liquids and slurries, ASME code for pressure piping, B31. The American Society of Mechanical Engineers, New York, USA.
- Bao. J. and Zhou. W. 2020. Influence of the corrosion anomaly class on predictive accuracy of burst capacity models for corroded pipelines. *International Journal of Geosynthetics and Ground Engineering*. 45.
- Bao. J., Zhang. S., Zhou. W. and Zhang. S. 2018. Evaluation of burst pressure of corroded pipe segments using three-dimensional finite element analysis. In: *Proceedings of the 2018 International Pipeline Conference. IPC2018*. Sept. 24 - 28. Calgary, Canada.
- Benjamin. A. C., Freire. J. L. F., Vieira. R. D. and Cunha. D. J. S. 2016a. Interaction of corrosion defects in pipelines - Part 1: Fundamentals. *International Journal of Pressure Vessels and Piping*. 144: 56 - 62.
- Benjamin. A. C., Freire. J. L. F., Vieira. R. D. and Cunha. D. J. S. 2016b. Interaction of corrosion defects in pipelines - Part 2: MTI JIP database of corroded pipe tests. *International Journal of Pressure Vessels and Piping*. 145: 41 - 59.
- Coulson K. E. W. and Worthingham. R. G. 1990. Pipe corrosion 1: standard damage assessment approach is overly conservative. *Oil and Gas Journal*. 88(15): 54 - 59.
- Coulson K. E. W. and Worthingham. R. G. 1990. Pipe corrosion conclusion: new guidelines promise more accurate damage assessment. *Oil and Gas Journal*. 88(16): 41 - 44.
- CSA. 2019. Oil and gas pipeline systems, CSA standard Z662-19. Mississauga, Canada.
- DNV. 2017. Corroded pipelines. DNV-RP-F101 code. Det Norske Veritas. Oslo, Norway.
- Kiefner. J. F. and Vieth. P. H. 1989. A modified criterion for evaluating the remaining strength of corroded pipe. Report prepared for American gas association. PR3 - 805. Columbus, OH, USA.
- Lamontagne. M. 2002. Interaction rules - an integral factor. In: *Proceedings of the NACE International Conference Corrosion*. April 7 - 11. Denver, USA.

- Mondal, B. C. and Dhar, A. S. 2016. Burst pressure assessment for pipelines with multiple corrosion defects. In: Proceedings of the 5th International Structural Specialty Conference. Canadian Society for Civil Engineering. Jun. 1 - 4. London, Canada.
- Mondal, B. C. and Dhar, A. S. 2017. Interaction of multiple corrosion defects on burst pressure of pipelines. Canadian Journal of Civil Engineering. 44(8): 589 - 597.
- Pipeline Operators Forum. 2016. Specifications and requirements for in-line inspection of pipelines. Version 2016.
- Sun, J. and Cheng, Y. 2018. Assessment by finite element modeling of the interaction of multiple corrosion defects and the effect on failure pressure of corroded pipelines. Engineering Structure. 165: 278 - 286.
- Cronin, D. S. 2000. Assessment of corrosion defects in pipelines. Ph.D. thesis. Waterloo, Canada: Department of Mechanical Engineering, University of Waterloo.
- Zhang, S., Yan, J., Kariyawasam, S., Huang, T. and Al-Amin, M. 2018. A more accurate and precise method for large metal loss corrosion assessment. In: Proceedings of the 2018 International Pipeline Conference. IPC2018. Sept. 24 - 28. Calgary, Canada.
- Zhu, X. K. and Leis B. N. 2005. Influence of yield-to-tensile strength ratio on failure assessment of corroded pipelines. Journal of Pressure Vessel Technology. 127: 436 - 442.

3 Influence of the Corrosion Anomaly Class on Predictive Accuracy of Burst Capacity Models for Corroded Pipelines

3.1 Introduction

Metal-loss corrosion is one of the major threats to the integrity of buried oil and gas pipelines (Lam and Zhou 2016). Corrosion on buried pipelines is largely influenced by properties of the surrounding soils such as the pH value, soil resistivity, water content and dissolved chloride. Extensive research has been reported in the literature to predict the severity of corrosion on pipeline using soil parameters as predictors (Alamilla et al. 2009; Velázquez 2010; Xiang and Zhou 2020). In practice, pipeline engineers carry out the fitness-for-service (FFS) assessment to evaluate the structural integrity of corroded pipelines and then determine necessary, if any, mitigation actions. The FFS assessment of a corroded pipeline generally involves evaluating the pressure containment capacity, i.e. burst capacity, of the pipeline by using one of several widely accepted semi-empirical burst capacity models such as ASME B31G (ASME 2018), B31G Modified (Kiefner and Vieth 1989) and RSTRENG (Kiefner and Vieth 1989) models. It follows that the predictive accuracy of the burst capacity model is critically important for the FFS assessment and subsequent decision-making for corrosion mitigations (Zhang et al. 2018; Zhang et al. 2020).

The accuracy of burst capacity models is commonly evaluated by comparing the burst capacities observed from a series of full-scale burst tests (P_{test}) of corroded pipe segments with the corresponding capacities predicted by the models. Benjamin et al. (2000) and Benjamin et al. (2016) investigated the accuracy of the B31G, B31G Modified, RSTRENG and DNV (DNV 2017) models based on full-scale burst tests of pipe specimens containing artificially-induced corrosion anomalies. The accuracy of several burst capacity models was evaluated by Cronin and Pick (2000) and Zhou and Huang (2012) based on full-scale burst tests of naturally corroded pipe specimens. Unlike artificially-induced corrosion anomalies, which are typically regular-shaped (e.g. cubic or semi-ellipsoidal), naturally-occurring corrosion anomalies are irregular-shaped and have complex geometries (Kiefner

and Vieth 1989; Cronin and Pick 2000; Zhang et al. 2018; Zhang et al. 2020). A given naturally-occurring corrosion anomaly is often characterized by its maximum depth (d_a), length (l_a) and width (w_a) (Fig. 3.1). High-resolution ILI tools are regularly employed to detect and size corrosion anomalies on the pipeline (Siraj and Zhou 2019). The sizing capabilities of ILI tools, in particular the tools based on the MFL technique, depend on the geometry of the corrosion anomaly (POF 2016). To facilitate the proper specification of sizing capabilities of ILI tools, a corrosion anomaly classification system is suggested by the Pipeline Operators Forum (POF) (POF 2016) and has been widely recognized in the pipeline industry. The POF system categorizes a given corrosion anomaly into one of seven classes depending on the length and width of the anomaly, namely general (GEN), pitting (PITT), axial grooving (AXGR), circumferential grooving (CIGR), pin hole (PINH), axial slotting (AXSL) and circumferential slotting (CISL). The specific classification criteria are summarized in Table 3.1. It is therefore valuable to investigate to what extent the accuracy of commonly used burst capacity models is dependent on the anomaly classification as the finding will help pipeline engineers select the most suitable models for anomalies in different classes and thus improve the accuracy of the FFS assessment. To our best knowledge, such a study has not been reported in the literature.

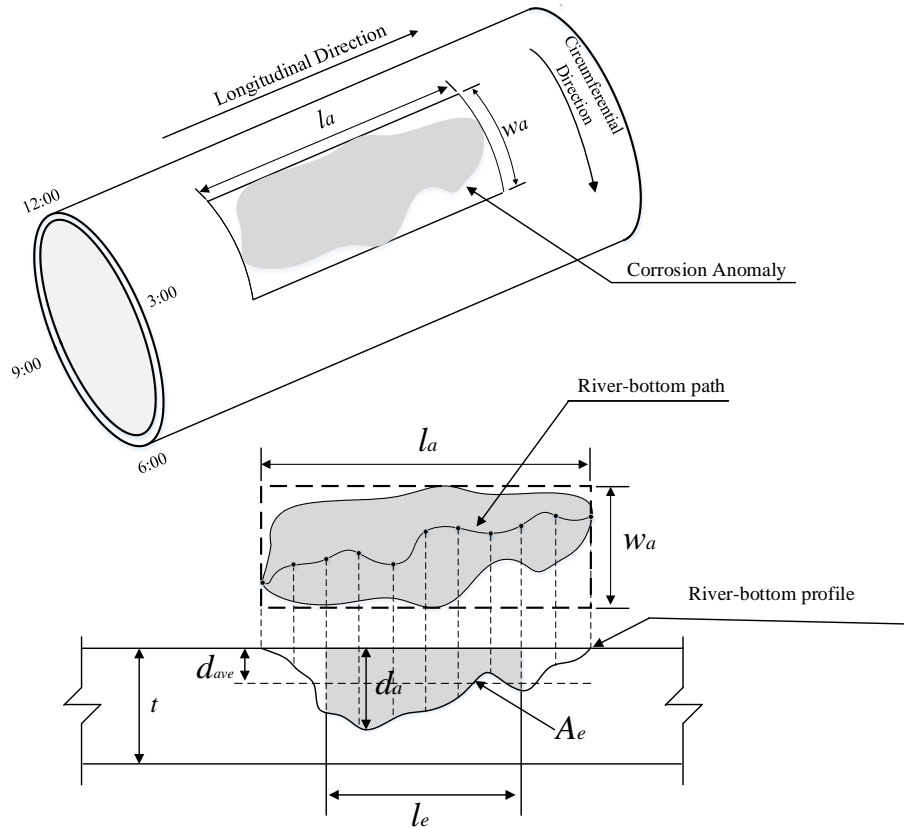


Figure 3.1 Illustration of a naturally occurring corrosion anomaly on a corroded pipeline

Table 3.1 POF classification criteria for corrosion anomalies

Anomaly Class	Definition
GEN	$w_a \geq 3A$ and $l_a \geq 3A$
PITT	$(A \leq l_a < 3A$ and $0.5 < l_a/w_a < 2$ and $w_a \geq A$) or $(3A \leq l_a < 6A$ and $l_a/w_a < 2$ and $w_a < 3A)$
AXGR	$A \leq w_a < 3A$ and $l_a/w_a \geq 2$
CIGR	$A \leq l_a < 3A$ and $l_a/w_a \leq 0.5$
PINH	$l_a < A$ and $w_a < A$
AXSL	$l_a \geq A$ and $w_a < A$
CISL	$l_a < A$ and $w_a \geq A$

$A = 10$ mm if pipe wall thickness (t) < 10 mm; $A = t$ if $t \geq 10$ mm.

Ideally, full-scale burst tests of naturally corroded pipe specimens should be used to evaluate the accuracy of the burst capacity model in terms of the anomaly classification. There are however significant practical obstacles to this approach. First, the number of full-scale burst tests of naturally corroded pipe specimens available in the literature is

limited due mainly to the high cost of obtaining suitable specimens (from corroded in-service pipelines) and carrying out the test. Second, the earlier literature on burst test, e.g. the well-known Battelle studies (Kiefner and Vieth 1989; Vieth and Kiefner and 1993; Kiefner et al. 1996), did not report widths of the corrosion anomalies on the test specimens, which further reduces the number of usable test data. Many studies (e.g. Chouchaoui 1993; Cronin 2000; Yoshida and Yamaguchi 2013; Zhang and Zhou 2020) over the last three decades have demonstrated the high accuracy of three-dimensional (3D) elasto-plastic finite element analyses (FEA) for evaluating the burst capacity of corroded pipelines. In particular, Bao et al. (2018) have demonstrated the accuracy of FEA for evaluating the burst capacity of full-scale naturally-corroded pipe specimens. A recently completed full-scale burst test program (Zhang et al. 2018; Zhang et al. 2020) includes 16 naturally corroded pipe specimens extracted from in-service pipelines. These specimens contain a large number of corrosion anomalies on their external surfaces. Furthermore, detailed 3D geometric profiles of the anomalies have been captured by high-resolution laser scanners and provided to the present study.

The objective of the present study is to investigate the influence of the corrosion anomaly classification on the accuracy of seven existing burst capacity models by comparing model- and FEA-predicted burst capacities for the corrosion anomalies identified on the above-mentioned pipe specimens. The seven burst capacity models are the B31G, B31G Modified (B31G-M), RSTRENG, PCORRC, PCORRC Modified (PCORRC-M) (Mokhtari and Melchers 2019), CSA (CSA 2019) and Shell92 models (Ritchie and Last 1995). The POF classification is employed to categorize the corrosion anomalies into seven classes. For the anomalies in each class, the basic statistics, i.e. mean and COV of the FEA-to-model predicted burst capacities are evaluated to quantify the accuracy of the burst capacity model. The rest of the chapter is organized as follows. Section 3.2 briefly describes the seven burst capacity models considered in the study. Section 3.3 describes the 16 test specimens reported by Zhang et al. (2018, 2020) and POF classification of the corrosion anomalies on the specimens. Section 3.4 presents details of the finite element model for the burst capacity evaluation and model validation. Section 3.5 presents the

accuracy of the seven burst capacity models in terms of the anomaly classification, followed by conclusions in Section 3.6.

3.2 Burst capacity models

The B31G, B31G-M, RSTRENG, CSA and Shell92 models are all based on the so-called NG-18 equation (Maxey et al. 1972). The CSA model is suggested in Annex O of the Canadian oil and gas pipeline standard, CSA Z662-19 (CSA 2019), whereas the Shell92 model was proposed by Ritchie and Last (1995) in the 1990s. The PCORRC model was developed by Leis and Stephens (Leis and Stephens 1997; Stephens and Leis 2000) based on results of parametric FEA. The PCORRC-M model is recently proposed by Mokhtari and Melchers (2019). The prediction equations of the seven models are listed as follows.

B31G

$$P_{b-31G} = \begin{cases} \frac{2t\sigma_f}{D} \frac{1 - \frac{2d_a}{3t}}{1 - \frac{2d_a}{3tM_1}} & d_a/t \leq 0.8 \text{ and } \frac{l^2}{Dt} \leq 20 \\ \frac{2t\sigma_f}{D} \left(1 - \frac{d_a}{t}\right) & d_a/t \leq 0.8 \text{ and } \frac{l^2}{Dt} > 20 \end{cases} \quad (3.1a)$$

$$\sigma_f = 1.1\sigma_y \quad (3.1b)$$

B31G-M

$$P_{b-31GM} = \frac{2t\sigma_f}{D} \frac{1 - \frac{0.85d_a}{t}}{1 - \frac{0.85d_a}{tM_2}} \quad d_a/t \leq 0.8 \quad (3.2a)$$

$$\sigma_f = \sigma_y + 68.95 \quad (3.2b)$$

CSA

$$P_{b-CSA} = \frac{2t\sigma_f}{D} \frac{1 - \frac{d_{ave}}{t}}{1 - \frac{d_{ave}}{tM_2}} \quad (3.3a)$$

$$\sigma_f = \begin{cases} 1.15\sigma_u & SMYS \leq 241 \text{ MPa} \\ 0.9\sigma_u & SMYS > 241 \text{ MPa} \end{cases} \quad (3.3b)$$

PCORRC

$$P_{b-PCO} = \frac{2t\sigma_u}{D} \left[1 - \frac{d_a}{t} \left(1 - \exp\left(\frac{-0.157l}{\sqrt{\frac{D(1-d_a/t)}{2}}} \right) \right) \right] \quad l \leq 2D \text{ and } \frac{d_a}{t} \leq 0.8 \quad (3.4)$$

Shell 92

$$P_{b-S92} = \frac{2t\sigma_f}{D} \frac{1 - \frac{d_a}{t}}{1 - \frac{d_a}{tM_1}} \quad d_a/t \leq 0.85 \quad (3.5a)$$

$$\sigma_f = 0.9\sigma_u \quad (3.5b)$$

RSTRENG

$$P_{b-RST} = \frac{2t\sigma_f}{D} \frac{1 - \frac{A_e}{l_e t}}{1 - \frac{A_e}{M_{2e} l_e t}} \quad d_a/t \leq 0.8 \quad (3.6a)$$

$$\sigma_f = \sigma_y + 68.95 \quad (3.6b)$$

PCORRC-M

$$P_{b-PCOM} = \frac{2t\sigma_u}{D} \left[1 - \frac{d_{eqv}}{t} \left(1 - \exp \left(\frac{-0.157l_a}{\sqrt{\frac{D(1-d_{eqv}/t)}{2}}} \right) \right) \right] \quad l_a \leq 2D \text{ and } \frac{d_a}{t} \leq 0.8 \quad (3.7a)$$

$$d_{eqv} = \left(\frac{v}{l_a w_a} + d_a \right) / 2 \quad (3.7b)$$

$$M_1 = \sqrt{1 + \frac{0.8l_a^2}{Dt}} \quad (3.8)$$

$$M_2 = \begin{cases} \sqrt{1 + 0.6275 \frac{l_a^2}{Dt} - 0.003375 \frac{l_a^4}{(Dt)^2}} & \frac{l_a^2}{Dt} \leq 50 \\ 3.3 + 0.032 \frac{l_a^2}{Dt} & \frac{l_a^2}{Dt} > 50 \end{cases} \quad (3.9)$$

In Eqs. (3.1)-(3.9), P_{b-31G} denotes the burst capacity predicted by the B31G model (the subscripts after the hyphen identify the particular burst capacity model); the meanings of P_{b-31GM} , P_{b-CSA} , P_{b-PCO} , etc. are self-explanatory; D is the pipe outside diameter; d_{ave} denotes the average depth of the river-bottom profile of the corrosion anomaly (Fig. 3.1); σ_y and σ_u denote the yield and tensile strengths of the pipe steel, respectively (the unit of σ_y in Eqs. (3.2) and (3.6) must be MPa); σ_f is known as the flow stress, and M_1 and M_2 denote the Folias factor, albeit calculated using different expressions. The RSTRENG model calculates the burst capacity by identifying the effective portion (i.e. effective area) of the river-bottom profile of the corrosion anomaly (Fig. 3.1), with the corresponding area and length denoted by A_e and l_e , respectively, and M_{2e} in Eq. (3.6) is obtained by substituting l_e in Eq. (3.9). The procedure to identify the effective area of the river-bottom profile can be found in many references (e.g. Kiefner and Vieth 1989; Zhou and Huang 2012). The PCORRC-M model replaces the maximum corrosion depth d_a in the original PCORRC

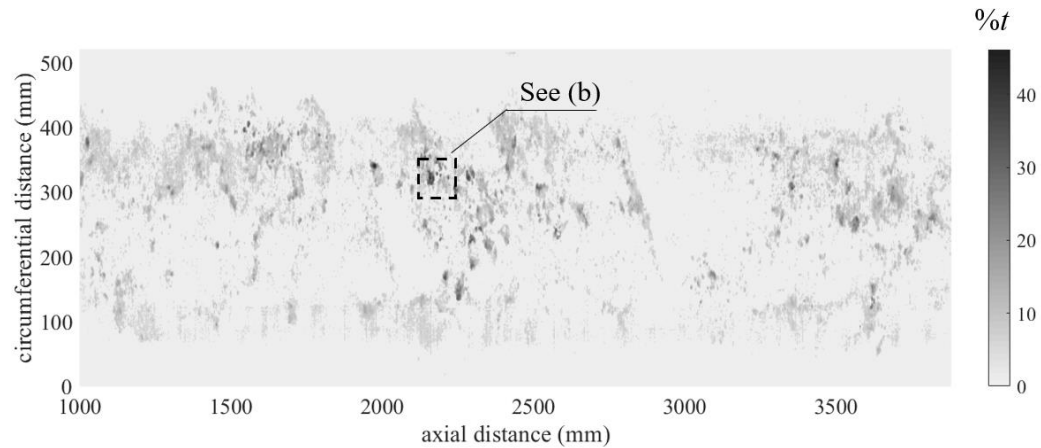
model by the equivalent depth d_{eqv} , which is a function of the metal loss volume V , length, width and maximum depth of a corrosion anomaly. In the FFS assessment in practice, σ_y and σ_u are typically set to equal the SMYS and SMTS, respectively, of the pipe steel. Note that all of the models except the CSA model have explicit applicability limits, e.g. $d_a/t \leq 0.8$ for B31G-M and RSTRENG. Note further that PCORRC-M is the only model that explicitly takes into account the defect width. Since PCORRC is developed by fitting results of parametric 3D FEA of corroded pipelines, the defect width is implicitly accounted for through the fitting constant and functional form of PCORCC.

3.3 Corroded pipe specimens

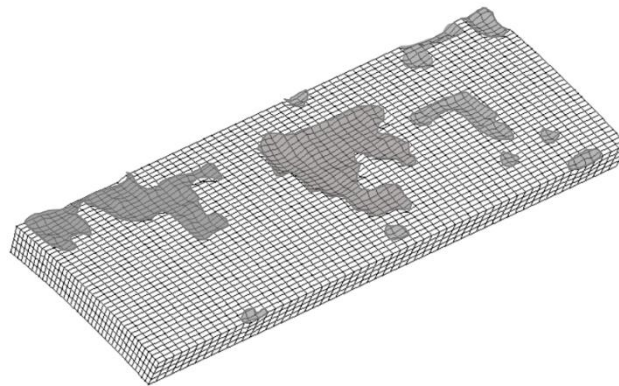
Zhang et al. (2018, 2020) reported a burst test program involving 16 pipe specimens removed from in-service pipelines with corruptions on the external surface. The key geometric and material properties of the specimens are summarized in Table 3.2. The yield and tensile strengths, and Young's modulus (E) of each specimen are determined by the tensile coupon test. The external surface of each specimen is scanned by a high-resolution laser scanning device before the burst test. Figure 3.2(a) depicts the scanned external surface of specimen 16-1, as an example. The longitudinal coordinate is with respect to the upstream girth weld of the pipe joint from which the specimen is removed, and the circumferential coordinate is the arc length with respect to the top of the pipe circumference (i.e. the 12 o'clock position). The corrosion depths ($\%t$) at grid positions within the scanned area are displayed in grayscale. The laser scan data for each specimen are processed to identify the individual corrosion anomalies contained within the scanned area. To this end, any corrosion depths within the scanned area that are less than or equal to $5\%t$ are ignored; in other words, the corrosion depths at the corresponding grid points are assumed to be zero. This facilitates the identification of individual anomalies. Since corrosion depths less than or equal to $10\%t$ are generally considered to have a negligible effect on the burst capacity (CSA 2019), this process does not influence the assessment of burst capacity models.

As an illustration, the individual corrosion anomalies identified within a small portion of the scanned surface of specimen 16-1 are depicted in Fig. 3.2(b). In total, 897 individual

corrosion anomalies are obtained from the 16 specimens listed in Table 3.2. A few anomalies on the specimens are not considered because the maximum depths of these anomalies exceed $80\%t$, which is beyond the applicability range for the B31G, B31G-M, PCORRC, PCORRC-M and RSTRENG models. The POF classifications of these anomalies are summarized in Table 3.3. Most (601) of the 897 corrosion anomalies are pitting corrosions. The X52-grade specimens contain 288 anomalies, whereas the X70-grade specimens contain 609 anomalies.



a) Scanned surface of specimen 16-1



b) Representative corrosion anomalies

Figure 3.2 Scanned surface and representative corrosion anomalies on specimen 16-

Table 3.2 Summary of the 16 test specimens in Zhang et al. (2018, 2020)

No.	Specimen ID	D (mm)	t (mm)	Steel grade	σ_y (MPa)	σ_u (MPa)	E (GPa)
1	16-1	408.2	6.2	X52	369	540	167
2	16-2	407.7	6.2	X52	369	540	167
3	16-3	407.7	6.2	X52	369	540	167
4	16-5	407.7	5.9	X52	393	557	189
5	16-6	407.4	5.9	X52	408	576	191
6	16-7	407.4	6.0	X52	408	576	191
7	20-3	508.0	6.5	X52	392	549	190
8	24-1	610.5	6.8	X70	553	680	145
9	24-2	610.5	6.7	X70	553	680	145
10	30-1	763.2	8.4	X70	536	655	187
11	30-2	763.4	8.5	X70	535	652	170
12	30-3	763.2	8.4	X70	568	691	171
13	30-4	763.7	8.5	X70	562	604	174
14	30-5	762.9	8.4	X70	546	659	154
15	30-6	764.1	8.4	X70	515	628	161
16	30-7	762.0	9.9	X70	370	535	214

Table 3.3 Number of individual anomalies in different POF classes identified on the 16 pipe specimens

Specimen	PINH	CISL	CIGR	AXSL	AXGR	PITT	GEN
16-1	4	0	2	5	1	43	3
16-2	3	5	2	4	1	50	11
16-3	0	2	0	5	0	36	1
16-5	3	1	2	3	6	20	6
16-6	0	1	0	1	5	3	4
16-7	1	1	2	1	0	11	2
20-3	5	1	0	4	4	22	1
24-1	4	2	1	7	11	27	0
24-2	3	2	1	2	6	95	3
30-1	4	3	3	3	3	56	29
30-2	3	5	3	6	0	35	5
30-3	1	3	0	0	0	17	1
30-4	8	6	0	4	4	54	6
30-5	5	4	0	2	0	81	8
30-6	0	0	0	0	0	0	14
30-7	2	3	0	5	1	51	7
All	46	39	16	52	42	601	101

The lengths and widths of the 897 corrosion anomalies are depicted in Fig. 3.3. The lengths of the corrosion anomalies range from 7 to 368 mm; the widths are between 5 and 213 mm, and the maximum depths of the anomalies are between 20 and 79% t , respectively.

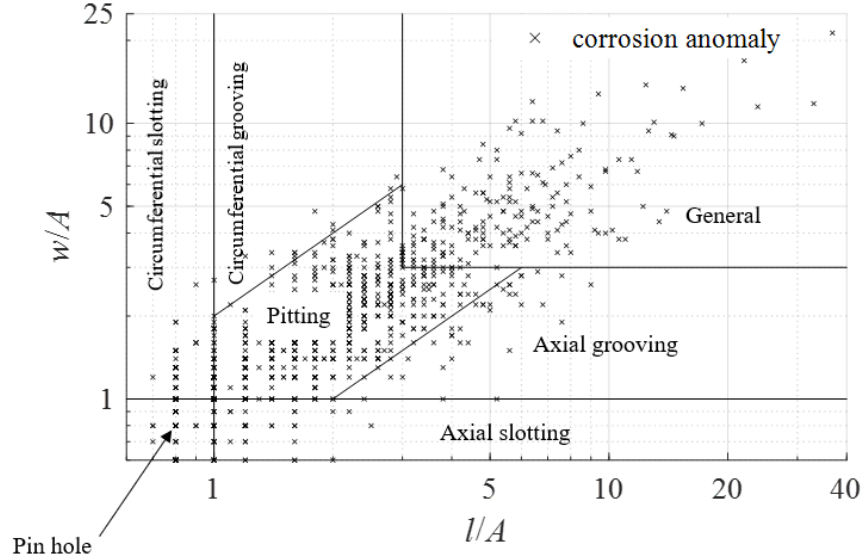


Figure 3.3 Lengths and widths of the 897 corrosion anomalies collected in the present study

3.4 Finite element analysis

3.4.1 FEA model

The commercial FEA software ANSYS (version 16.1) is used to perform the FEA of the 897 corrosion anomalies involved in the present study. The 8-node brick elements (C3D8) with full integration points are primarily used in the finite element model, with the 6-node prismatic (C3D6) linear elements with full integration points used to transition the fine mesh within the corroded region to the relatively coarse mesh within the corrosion-free region on the pipe model. The von Mises yield criterion, associated plastic flow rule and isotropic hardening model are adopted. The commonly used power-law true stress (σ)-strain (ε) relationship is employed in the analysis.

$$\begin{cases} \sigma = E\varepsilon & \sigma < \sigma_y \\ \sigma = K\varepsilon^n & \sigma \geq \sigma_y \end{cases} \quad (3.10)$$

where K is the strength coefficient, and n is the strain hardening exponent. The values of n and K values are evaluated from Zhu and Leis (2005).

$$n = 0.224 \left(\frac{\sigma_u}{\sigma_y} - 1 \right)^{0.604} \quad (3.11)$$

$$K = \frac{\sigma_u e^n}{n^n} \quad (3.12)$$

where e is the base of natural logarithm. Figure 3.4 depicts the $\sigma - \varepsilon$ relationships for two representative specimens, 16-1 and 30-1.

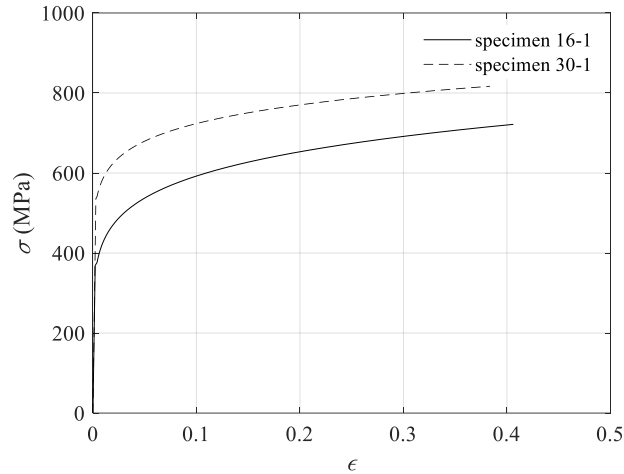


Figure 3.4 True stress σ - true strain ε curves for specimens 16-1 and 30-1

Various failure criteria have been suggested in the literature to define the burst capacity of corroded pipelines in FEA. For example, Choi et al. (2003) suggested that the burst capacity corresponds to the point where the von Mises stress throughout the remaining ligament in the corroded region reaches 90% of the true stress corresponding to σ_u . The failure criterion adopted in the present study states that the burst capacity is reached when the maximum von Mises stress anywhere in the corroded region reaches the true stress corresponding to σ_u . The adequacy of this criterion has been demonstrated by Cronin (2000), Bao et al. (2018) and Zhang and Zhou (2020).

3.4.2 Validation of FEA model

Sixteen (16) full-scale burst tests of naturally corroded pipe specimens reported by Zhang et al. (2018, 2020) and fourteen (14) full-scale burst tests of pipe specimens containing artificially-induced corrosion anomalies reported by Chouchaoui (1993) are used to validate the finite element model and failure criterion described in Section 3.4.1. The attributes of the 16 naturally corroded specimens in Zhang et al. (2018, 2020) are described in Section 3.3. For each of the specimens, Zhang et al. (2018, 2020) identified the critical corrosion cluster at which burst was observed to initiate during the test. Note that a cluster

includes a series of closely-spaced corrosion anomalies grouped using the so-called interaction rule to account for the potential interaction between the anomalies; that is, the burst capacity corresponding to interacting anomalies is lower than the burst capacities corresponding to respective individual anomalies. The commonly used B31.4 rule (ASME 2019) was employed by Zhang et al. (2018, 2020) to identify the clusters. According to this rule, two anomalies are considered to form a cluster (i.e. interacting with each other) if both of the following two conditions are met: the longitudinal separation distance is less than or equal to 1 inch (25.4 mm), and the circumferential separation distance is less than or equal to $6t$ (Fig. 3.5). The key geometric characteristics of the critical corrosion clusters on the 16 specimens in Zhang et al. (2018, 2020) are summarized in Table 3.4. Table 3.5 summarizes the attributes of the 14 specimens as well as key geometric characteristics of the artificially-induced corrosion clusters reported by Chouchaoui (1993).

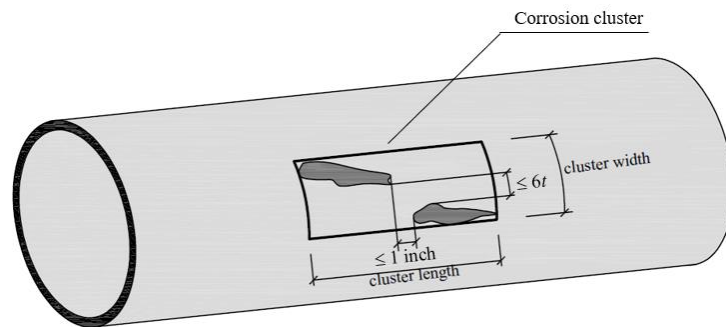


Figure 3.5 Illustration of the 1 in \times $6t$ interaction rule

Table 3.4 Geometric characteristics of the critical corrosion clusters on 16 specimens in Zhang et al. (2018, 2020)

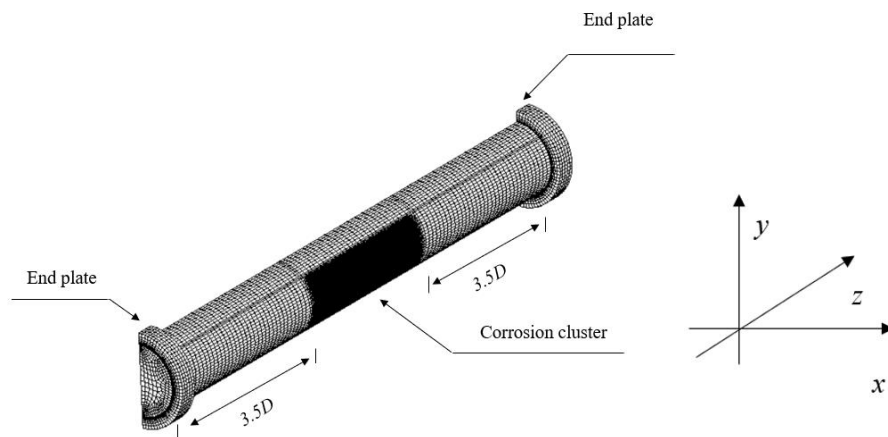
No.	Specimen	Cluster geometry		
		Length (mm)	Width (mm)	Maximum depth (% <i>t</i>)
1	16-1	844	296	33
2	16-2	1160	391	47
3	16-3	330	212	43
4	16-5	356	223	97
5	16-6	344	121	57
6	16-7	542	375	87
7	20-3	362	142	28
8	24-1	1504	248	30
9	24-2	428	191	39
10	30-1	4326	407	68
11	30-2	430	262	48
12	30-3	610	386	73
13	30-4	710	192	78
14	30-5	782	271	59
15	30-6	1450	244	75
16	30-7	1110	104	32

Table 3.5 Geometric characteristics of 14 specimens and the critical corrosion clusters on the 14 specimens in Chouchaoui (1993)

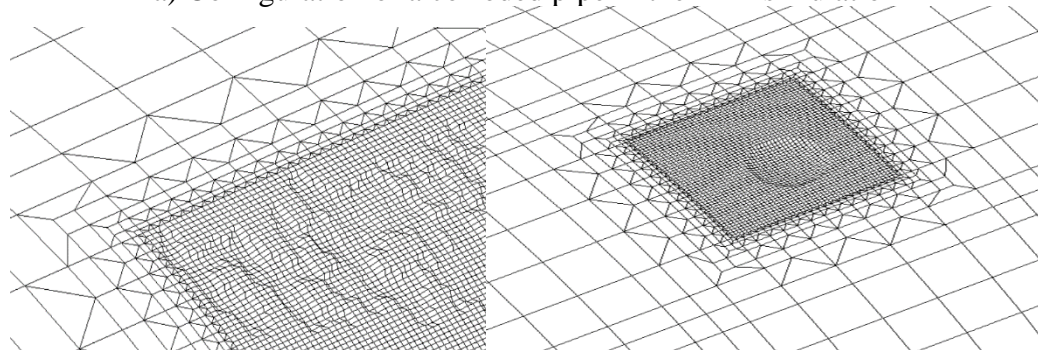
Specimen	Specimen geometry		Cluster geometry			Material property			
	<i>D</i> (mm)	<i>t</i> (mm)	Length (mm)	Width (mm)	Maximum depth (% <i>t</i>)	Steel grade	σ_y (MPa)	σ_u (MPa)	<i>E</i> (GPa)
S1CC	324	6.16	20.12	19.99	61	X46	356	514	207
S3CC	324	6.25	19.93	72.83	61				
S4CC	324	6.18	19.92	174.21	61				
S1CO	324	6.40	20.07	19.30	50				
S2CO	324	6.01	19.35	37.98	60				
S3CO	324	6.30	19.80	51.22	57				
S1LC	322	6.27	77.38	20.88	60				
S2LC	324	6.29	72.31	20.81	60				
S3LC	324	6.24	72.12	20.81	61				
S4LC	324	6.16	173.97	19.99	60				
S1LO	325	6.45	20.82	21.51	47				
S2LO	324	6.40	39.38	20.22	58				
S3LO	325	6.45	97.92	20.86	59				
S4LO	324	6.35	123.23	21.41	59				

Figure 3.6 depicts the finite element models for two representative specimens from Zhang et al. (2018) and Zhang et al. (2020) (specimen 16-1) and Chouchaoui (1993) (specimen S1CC), respectively. Based on the mesh convergence study, the element size is selected

to be 2 (longitudinal) \times 1 (circumferential) mm in the corrosion region, and 32 \times 16 mm in the corrosion-free region, with the C3D6 elements used as transition elements between the fine and coarse meshes. Four layers of elements are used along the thickness direction to avoid the shear locking effect. To eliminate the influence of the end condition, the model is extended 3.5*D* longitudinally from each side of the corrosion region (Fig. 3.6a). To improve the computational efficiency, only a half pipe model as opposed to the full pipe model is generated. Although this implies that the full pipe model contains two identical corrosion clusters, it has no impact on the burst capacity evaluated because the two corrosion clusters are kept well separated circumferentially to eliminate any interaction effects. The model for specimen 16-1 contains approximately 500,000 nodes and 560,000 elements, whereas the model for specimen S1CC contains approximately 42,000 nodes and 33,000 elements.



a) Configuration of a corroded pipe in the FEA simulation



b) A corrosion cluster from specimen 16-1

c) A corrosion cluster from S1CC

Figure 3.6 Two representative FEA models of corrosion clusters on specimens 16-1 and S1CC

The FEA-predicted burst capacities (P_{FEA}) as well as burst capacities observed in the test for the 30 specimens are depicted in Figure 3.7. The mean and COV of test-to-predicted ratio for the 16 specimens reported by Zhang et al. (2018) and Zhang et al. (2020) are 0.95 and 7.4%, respectively. FEA over-predicts the burst capacities of specimens 16-2, 16-3 and 20-3 by 16.9%, 19.6% and 18.4%, respectively. The significant over-predictions of specimen 16-2 and 16-3 can be explained by the equipment malfunction that occurred during the testing of these two specimens. The tests were paused at high internal pressure levels (i.e. close to the burst pressure) because of the malfunctioning of a certain test equipment. The high internal pressure levels were maintained until the replacement of the malfunctioning equipment, after which the tests were resumed. The sustaining of a high internal pressure level may lead to the development of micro cracks in the corrosion region and reduce the burst capacity of the test specimen. The specimen 20-3 is known to be a poorly manufactured pipe with significant non-uniformity in the mechanical properties along the pipe body. If specimens 16-2, 16-3 and 20-3 are excluded, the mean and COV of the test-to-predicted ratio for the remaining 13 specimens are 0.98, 5.1%, respectively. The mean and COV of the test-to-predicted ratios for the 14 specimens in Chouchaoui (1993) are 1.00 and 5.4%, respectively. These results demonstrate the accuracy of the finite element model and failure criterion.

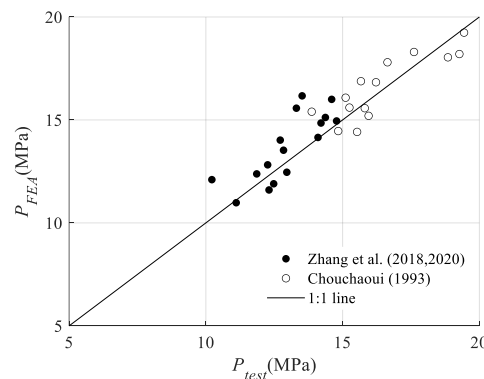


Figure 3.7 Comparison between the test-based and FEA-based burst capacities

3.5 Influence of anomaly classification on the accuracy of burst capacity models

As shown in Table 3.3 and Fig. 3.3, a total of 897 individual corrosion anomalies are identified on the 16 specimens reported by Zhang et al. (2018) and Zhang et al. (2020). For each of the specimens, FEA and the semi-empirical models are employed to evaluate its burst capacities by considering all of the identified corrosion anomalies on the specimen individually. For example, a total of 58 burst capacities of specimen 16-1 are obtained from FEA, each corresponding to one of the 58 corrosion anomalies identified on the specimen. The values of σ_y and σ_u employed in FEA and burst capacity models for a given specimen are the same as those provided in Table 3.2. The stress-strain relationship adopted in FEA is given by Eqs. (3.10) - (3.12), with the value of E given in Table 3.2.

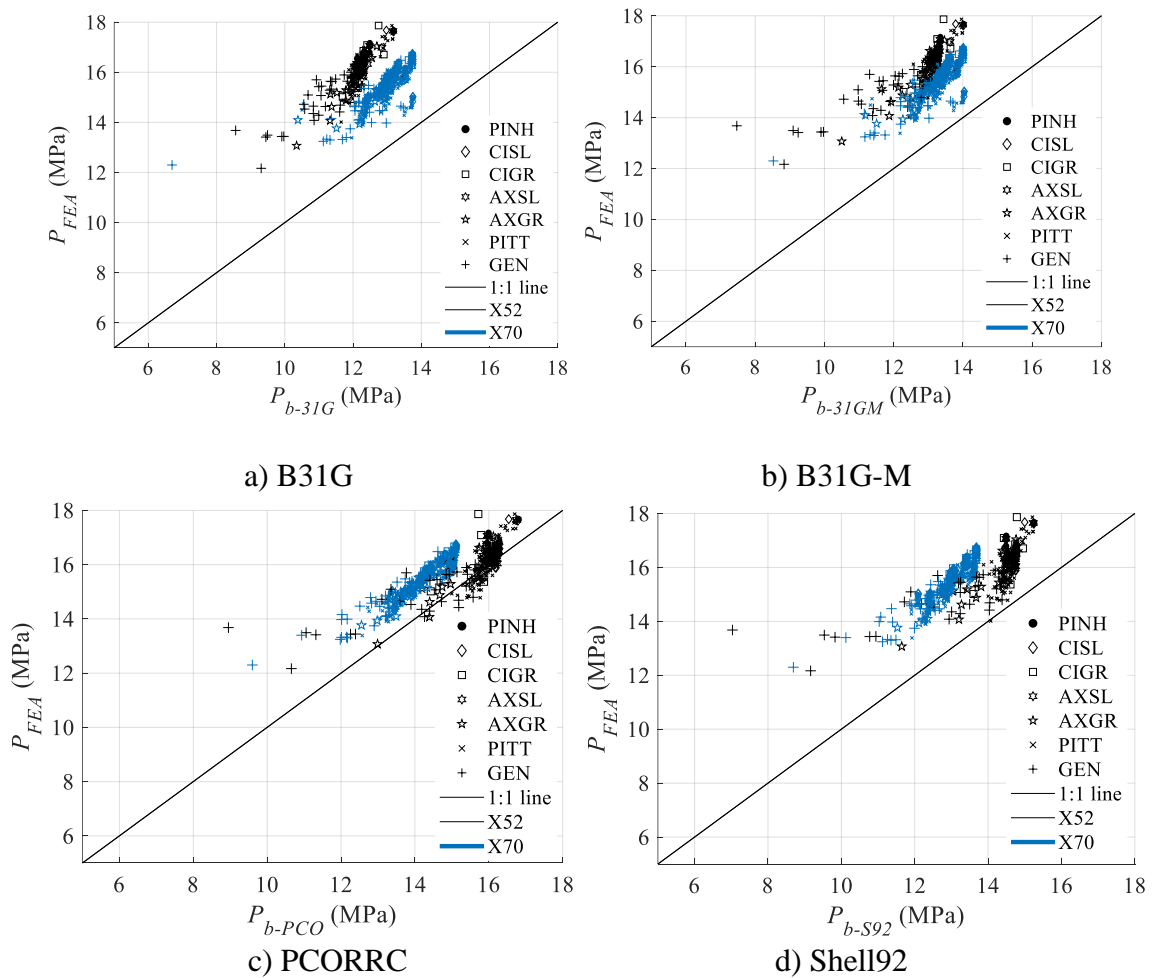
The comparisons between the burst capacities predicted by the semi-empirical models and FEA are depicted in Fig. 3.8, with the mean and COV of the FEA-to-model predicted ratios summarized in Table 3.6. The results in Table 3.6 indicate that all seven burst capacity models are on average more conservative than FEA, regardless of the class of corrosion anomalies. For a given burst capacity model, its predictive accuracy is similar for the six non-general classes of anomalies, i.e. PINH, PITT, AXSL, AXGR, CISL and CIGR. The model in general becomes less accurate for anomalies in the general corrosion class (GEN), although the extent of the decrease in accuracy varies among different models. This is expected given that anomalies in the GEN class are larger and likely have more complex geometry than anomalies in the other classes. The B31G model is more conservative and has higher predictive variability than the other models for all classes of anomalies (the mean and COV of P_{FEA}/P_{b-31G} are the highest among all the models). Figure 3.8(a) reveals that the B31G model is more conservative for X52-grade specimens than for X70-grade specimens, due primarily to the inadequacy of the flow stress definition in the model. The B31G-M model is consistently more accurate than the B31G model for the six non-general classes of anomalies. For the GEN anomalies, the accuracies of these two models are however practically the same and lower than those of the other five models. The Shell92 and CSA models are of very similar accuracy for the six non-general classes of anomalies. This is somewhat unexpected because the former model requires only the maximum depth

and length of an anomaly while the latter requires the entire river-bottom profile to compute the average depth of the anomaly. This observation implies that the river-bottom profile of non-general classes of anomalies is near rectangular, i.e. $d_{ave} \approx d_a$. For the GEN anomalies, the CSA model is markedly more accurate than the Shell92 model, which implies that a rectangular idealization of the river-bottom profile with the depth of the rectangle equal to the maximum corrosion depth d for the GEN anomalies is likely to be unsatisfactory. It is worth noting that the COV of P_{FEA}/P_{b-CSA} for the GEN anomalies is lower than those of all the other models. The accuracy of RSTRENG model is similar to that of B31G-M for the non-general classes of anomalies. For the GEN anomalies, the accuracy of RSTRENG is comparable to that of CSA, with the COV of P_{FEA}/P_{b-RST} somewhat higher than that of P_{FEA}/P_{b-CSA} .

The PCORRC model is the most accurate among all the models that do not require the river-bottom profile. A comparison between the statistics for PCORRC and PCORRC-M suggests that the latter does not offer improved predictive accuracy over the former for the non-general classes of anomalies. Nevertheless, PCORRC-M is more accurate than PCORRC when applied to the GEN anomalies: the mean (1.03) and COV (5.3%) of P_{FEA}/P_{b-PCOM} are less than those of original PCORRC. This can be attributed to that PCORRC-M takes into account the total volume loss of the corrosion anomaly in the prediction equation as opposed to the maximum depth and length only in PCORRC. Note that the predictions by PCORRC and PCORRC-M are the least biased, i.e. means of P_{FEA}/P_{b-PCO} and P_{FEA}/P_{b-PCOM} closest to unity, compared with the other models. Note also that predictions by PCORRC and PCORRC-M are lower than the corresponding FEA predictions for some anomalies contained in the X52-grade specimens (Fig. 3.8(c)), whereas the predictions by the other five models are consistently lower than the corresponding FEA predictions for all the anomalies considered.

Based on the above discussions, the PCORRC model is recommended for non-general classes of anomalies as it achieves a good balance between accuracy and ease of application in practice. For anomalies in the GEN class, the CSA model is recommended based primarily on the COV of P_{FEA}/P_{b-CSA} being lower than those of the other models. Although

predictions by the CSA model tend to be more biased than those by PCORRC and PCORRC-M for the GEN anomalies, it is believed that such a bias can be addressed relatively easily in practice by applying, for example, a simple multiplicative correction factor to the model predictions. Finally, it must be emphasized that the present study focuses on burst capacity predictions for individual corrosion anomalies as opposed to clusters that contain a series of closely-spaced individual anomalies. Given that corrosion clusters generally have more complex geometric characteristics than individual anomalies, the finding of the present study suggests that the burst capacity models requiring detailed corrosion geometric information (such as the CSA, RSTRENG and PCORRC-M models) will have markedly higher predictive accuracies than the models requiring only simple corrosion geometry and therefore should be employed in practice whenever feasible.



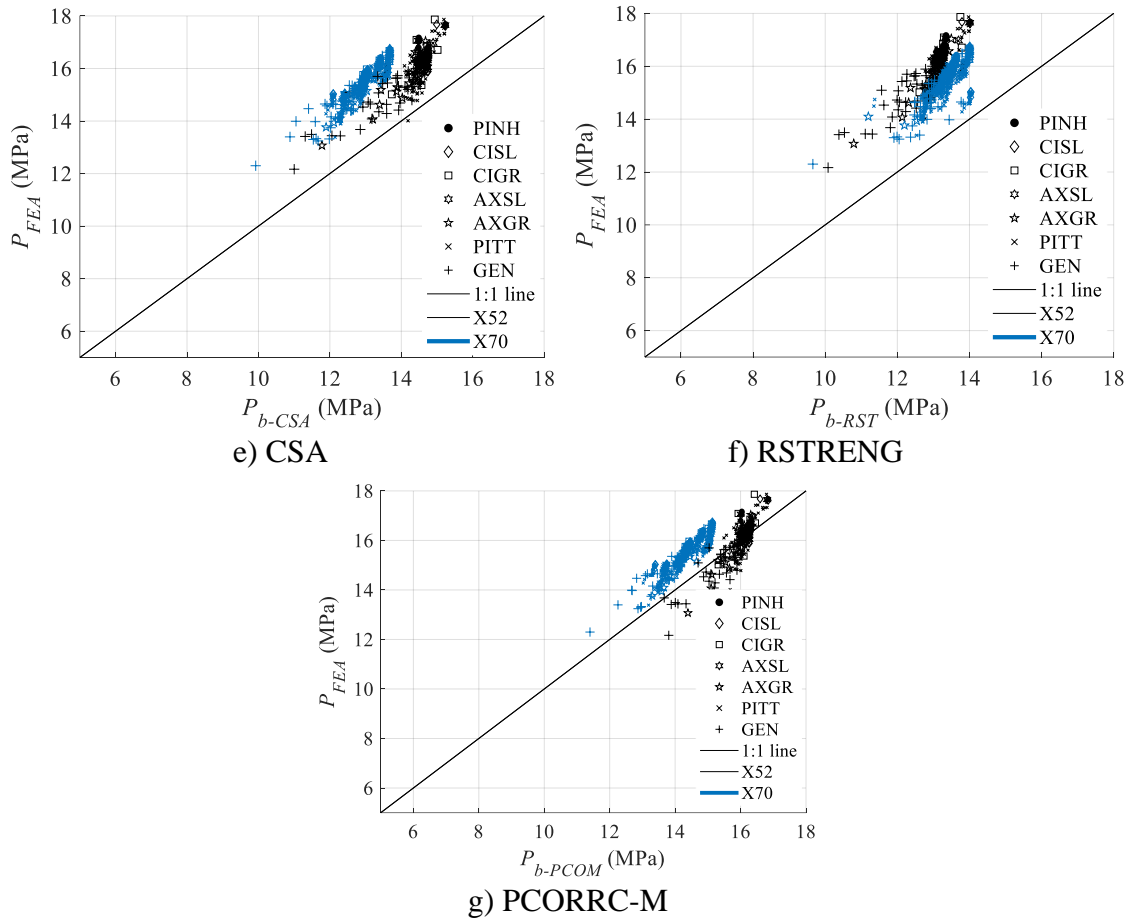


Figure 3.8 Comparison between the FEA and predicted burst capacities in terms of different semi-empirical models and corrosion anomaly classes

Table 3.6 Statistics of the FEA-to-model predicted burst capacity ratios for different classes of corrosion anomalies

Model		PINH	CISL	CIGR	AXSL	AXGR	PITT	GEN
P_{FEA}/P_{b-31G}	Mean	1.24	1.24	1.27	1.26	1.23	1.23	1.25
	COV (%)	5.6	6.3	5.6	5.4	4.9	6.1	9.1
P_{FEA}/P_{b-31GM}	Mean	1.19	1.19	1.22	1.20	1.19	1.18	1.22
	COV (%)	3.5	4.3	3.9	3.0	3.5	4.0	9.0
P_{FEA}/P_{b-PCO}	Mean	1.08	1.07	1.07	1.05	1.06	1.06	1.10
	COV (%)	3.2	3.9	4.3	3.8	3.4	3.8	6.7
P_{FEA}/P_{b-S92}	Mean	1.19	1.18	1.17	1.16	1.16	1.16	1.20
	COV (%)	3.3	4.0	4.7	4.0	3.4	4.0	9.0
P_{FEA}/P_{b-CSA}	Mean	1.19	1.19	1.17	1.16	1.16	1.16	1.15
	COV (%)	3.3	4.0	4.7	3.9	3.8	4.0	4.1
P_{FEA}/P_{b-RST}	Mean	1.19	1.19	1.21	1.20	1.17	1.18	1.16
	COV (%)	3.5	4.3	3.5	3.0	3.1	4.1	5.2
P_{FEA}/P_{b-PCOM}	Mean	1.07	1.07	1.06	1.05	1.04	1.05	1.03
	COV (%)	3.2	3.9	4.8	3.9	4.6	4.0	5.3

3.6 Conclusions

This chapter investigates the predictive accuracy of semi-empirical burst capacity models for corroded pipelines in terms of the classification of corrosion anomalies. Seven burst capacity models are considered, namely the B31G, B31G-M, PCORRC, PCORRC-M, Shell92, CSA and RSTRENG models. A total of 897 individual corrosion anomalies are identified on the external surfaces of 16 naturally corroded pipe specimens removed from in-service pipelines. According to the POF anomaly classification system, these anomalies are grouped into 46 pin holes, 39 circumferential slotting, 16 circumferential grooving, 52 axial slotting, 42 axial grooving, 601 pitting and 101 general corrosion anomalies. The burst capacities of the pipe specimens corresponding to each of these anomalies are evaluated using the seven burst capacity models, as well as three-dimensional elasto-plastic FEA validated by full-scale burst tests reported in the literature. With the FEA-predicted burst capacity considered as the benchmark, the accuracy of the semi-empirical burst capacity model is evaluated based on the mean and COV of the FEA-to-model predicted burst capacity ratios calculated corresponding to the different classes of anomalies.

It is observed that the accuracy of a given burst capacity model is similar for non-general classes of anomalies. The accuracy of the model decreases when applied to the general class of anomalies, although the degree of the accuracy deterioration varies among the models. The PCORRC model is recommended for non-general classes of anomalies with the mean of FEA-to-predicted burst capacity ratios ranging from 1.05 to 1.08 and corresponding COV ranging from 3.2 to 4.3%. The CSA model is recommended for anomalies in the general class with the mean and COV of the FEA-to-model predicted burst capacity ratios equal to 1.16 and 4.1%, respectively.

References

- Alamilla. J. L., Espinosa-Medina. M. A. and Sosa. E. 2009. Modelling steel corrosion damage in soil environment. *Corrosion Science*. 51(11): 2628 - 2638.
- ASME. 2018. Manual for determining the remaining strength of corroded pipelines. Supplement to ASME B31 code for pressure piping. ASME B31G - 2018. New York, USA.

- AMSE. 2019. Pipeline transportation systems for liquids and slurries, ASME code for pressure piping, B31. The American Society of Mechanical Engineers, New York, USA.
- Bao. J., Zhang. S., Zhou. W. and Zhang. S. 2018. Evaluation of burst pressure of corroded pipe segments using three-dimensional finite element analysis. In: Proceedings of the 2018 International Pipeline Conference. IPC2018. Sept. 24 - 28. Calgary, Canada.
- Benjamin. A. C., Viera. R. D., Freire. J. L. F. and Castro. J. T. P. 2000. Burst tests on pipeline with long external corrosion. In: Proceedings of the 2000 International Pipeline Conference. IPC2000. Oct. 1 - 5. Calgary, Canada.
- Benjamin. A. C., Freire. J. L. F., Vieira. R. D. and Cunha. D. J. S. 2016. Interaction of corrosion defects in pipelines - Part 2: MTI JIP database of corroded pipe tests. International Journal of Pressure Vessels and Piping. 145: 41 - 59.
- Choi. J. B., Goo. B. K., Kim. J. C., Kim. Y. J. and Kim. W. S. 2003. Development of limit load solutions for corroded gas pipelines. International Journal of Pressure Vessels and Piping. 80: 121 - 128.
- Chouchaoui. B. 1993. Evaluating the Remaining Strength of Corroded Pipelines. Ph.D. thesis. Waterloo, Canada: Department of Mechanical Engineering, University of Waterloo.
- Cronin. D. S. 2000. Assessment of corrosion defects in pipelines. Ph.D. thesis. Waterloo, Canada: Department of Mechanical Engineering, University of Waterloo.
- Cronin. D. S. and Pick. R. J. 2000. Experimental database for corroded pipe: evaluation of RSTRENG and B31G. In: Proceedings of the 2000 International Pipeline Conference. IPC2000. Oct. 1 - 5. Calgary, Canada.
- CSA. 2019. Oil and gas pipeline systems, CSA Standard Z662 - 19. Mississauga, Canada.
- DNV. 2017. Corroded Pipelines. DNV-RP-F101 code. Det Norske Veritas. Oslo, Norway.
- Kiefner. J. F. and Vieth. P. H. 1989. A modified criterion for evaluating the remaining strength of corroded pipe. Report prepared for American gas association. PR3 - 805. Columbus, OH, USA.
- Kiefner. J. F., Vieth. P. H. and Roytman. I. 1996. Continued validation of RSTRENG. Report prepared for the line pipe research supervisory committee, Pipeline Research Committee of Pipeline Research Council International, Inc. PRCI. Catalog No. L51749e. Columbus, OH, USA.

- Lam. C. and Zhou. W. 2016. Statistical analyses of incidents on onshore gas transmission pipelines based on PHMSA database. *International Journal of Pressure Vessels and Piping*. 145: 29 - 40.
- Leis. B. N. and Stephens. D. R. 1997. An alternative approach to assess the integrity of corroded line pipe part I: current status; part II: alternative criterion. In: *Proceedings of the 7th International Offshore and Polar Engineering Conference*. May 25 - 30. Honolulu, USA.
- Maxey. W. A., Kiefner. J. F., Eiber. R. J. and Duffy. A. R. 1972. Ductile fracture initiation, propagation, and arrest in cylindrical vessels. Fracture toughness. In: *Proceedings of the 1971 National Symposium on Fracture Mechanics, Part II, ASTM STP 514*. American Society of Testing and Materials: 70 - 81.
- Mokhtari. M. and Melchers. R. E. 2019. Next generation fracture prediction models for pipes with localized corrosion defects. *Engineering Failure Analysis*. 105: 610 - 626.
- Pipeline Operators Forum. 2016. Specifications and requirements for in-line inspection of pipelines. Version 2016.
- Ritchie. D. and Last. S. 1995. Burst criteria of corroded pipelines - defect acceptance criteria. In: *Proceedings of the EPRG/RPC Biennial Joint Technical Meeting on Line Pipe Research*. Apr. 18 - 21. Cambridge, UK.
- Siraj. T. and Zhou. W. 2019. Quantification of measurement error in the lengths of metal-loss corrosion defects reported by inline inspection tools. *Journal of Pressure Vessel Technology*. 141(6): 061402.
- Stephens. D. R. and Leis. B. N. 2000. Development of an alternative failure criterion for residual strength of corrosion defects in moderate-to high-toughness pipe. In: *Proceedings of the 2000 International Pipeline Conference, IPC2000*. Oct. 1 - 5. Calgary, Canada.
- Velázquez. J. C., Caleyó. F., Valor. A. and Hallen. J. M. 2010. Field study - pitting corrosion of underground pipelines related to local soil and pipe characteristics. *Corrosion*. 66(1): 016001.
- Vieth. P. H. and Kiefner. J. F. 1993. Database of corroded pipe tests. Report prepared for the pipeline corrosion supervisory committee, Pipeline Research Committee of Pipeline Research Council International, Inc. PRCI Catalog No. L51689. Columbus, OH, USA.
- Xiang. W. and Zhou. W. 2020. A nonparametric Bayesian network model for predicting corrosion depth on buried pipelines. *Corrosion*. 76(3): 235 - 247.

- Yoshida. N. and Yamaguchi. A. 2013. Effect of thickness measurement procedure on stress analysis of pipes with local metal loss. In: Proceedings of the ASME 2013 Pressure Vessel and Piping Conference. PVP2013. Jul. 14 - 18. Paris, France.
- Zhang. S., Yan. J., Kariyawasam. S., Huang. T. and Al-Amin. M. 2018. A more accurate and precise method for large metal loss corrosion assessment. In: Proceedings of the 2018 International Pipeline Conference. IPC2018. Sept. 24 - 28. Calgary, Canada.
- Zhang. S., Yan. J., Kariyawasam. S., Huang. T. and Al-Amin. M. 2020. Plausible profile (Psqr) corrosion assessment model: refinement, validation and operationalization. In: Proceedings of the 2020 International Pipeline Conference. IPC2020. Sept. 28 - Oct. 2. Calgary, Canada.
- Zhang. S. and Zhou. W. 2020. Assessment of effects of idealized defect shape and width on the burst capacity of corroded pipelines. *Thin-Walled Structures*. 154: 106806.
- Zhou. W. and Huang. G. 2012. Model error assessments of burst capacity models for corroded pipelines. *International Journal of Pressure Vessels and Piping*. 99 - 100: 1 - 8.
- Zhu. X. K. and Leis. B. N. 2005. Influence of yield-to-tensile strength ratio on failure assessment of corroded pipelines. *Journal of Pressure Vessel Technology*. 127: 436 - 442.

4 A Modified RSTRENG Model for Evaluating the Burst Capacity of Corroded Pipelines

4.1 Introduction

Corrosion poses a significant threat to the structural integrity of buried oil and gas steel pipelines as they age (Lam and Zhou 2016), and generally manifests as irregularly-shaped three-dimensional (3D) features of metal loss, i.e. pipe wall thinning, on the external or internal surface (or both) of the pipeline (Fig. 4.1). A corrosion feature can be a single isolated anomaly or a group of closely-spaced anomalies, commonly known as a cluster (Fig. 4.1). The so-called interaction rules (Lamontagne 2002) are used in practice to determine if multiple anomalies in proximity should be treated as a cluster. To carry out the fitness-for-service (FFS) assessment of a pipeline containing a corrosion feature, pipeline engineers typically employ semi-empirical models to predict the pressure containment capacity, i.e. burst capacity of the pipeline, for example, the ASME B31G (ASME 2018), B31G Modified (Kiefner and Vieth 1989), RSTRENG (Kiefner and Vieth 1989), DNV-S (DNV-RP-F101 2017), DNV-I (DNV-RP-F101 2017), and PCORRC models (Leis and Stephens 1997; Stephens and Leis 2000). Note that DNV-S and DNV-I refer to the two models applicable to single and interacting corrosion anomalies, respectively, as recommended in DNV-RP-F101 (2017).

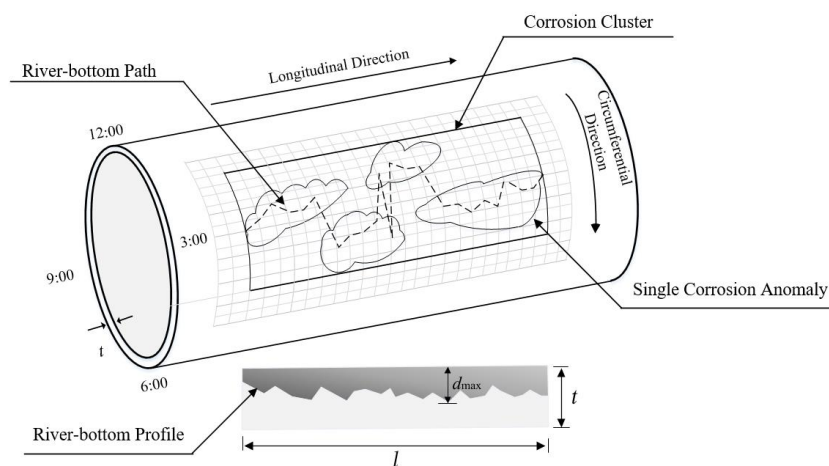


Figure 4.1 Illustration of a corrosion cluster, river-bottom path and river-bottom profile

The semi-empirical burst capacity models can be grouped into two categories, namely Level 1 and Level 2 models (ASME 2018). Level 1 models, such as the ASME B31G, B31G Modified, DNV-S, and PCORRC models, employ the length (l) and maximum depth (d_{max}) of the corrosion feature (Fig. 4.1) to evaluate the burst capacity, whereas Level 2 models, such as the RSTRENG and DNV-I models, employ the river-bottom profile of the corrosion feature in the evaluation. The river-bottom profile is generated by projecting the path that connects the deepest points along different circumferential planes intersecting the corrosion feature onto a longitudinal plane perpendicular to the pipe wall thickness (Fig. 4.1). Zhou and Huang (2012) investigated the predictive accuracy of several well-known Level 1 and 2 models by comparing model-predicted burst capacities with the corresponding observed burst capacities for a series of full-scale tests of pipe specimens containing naturally-occurring corrosion features. They reported that the RSTRENG model is the most accurate among the models considered; however, it is still associated with considerable model uncertainty.

The length and maximum depth employed in Level 1 models are rather crude characterizations of the geometry of a 3D corrosion feature. While the river-bottom profile captures the most severe path in the corrosion feature, the two-dimensional nature of the profile means that it misses other potentially important characteristics of the feature such as its width and metal loss volume. This suggests that the accuracy of semi-empirical models can be improved by better capturing the 3D characteristics of the corrosion feature. Research in this regard has been reported in the recent literature. Mokhtari and Melchers (2018, 2019) developed a modified PCORRC model, referred to as 3D PCORRC, by replacing the maximum depth in the original PCORRC model with the equivalent depth, which is a function of the volume, width, length and maximum depth of the corrosion feature. The 3D PCORRC model is shown to have an excellent accuracy for single isolated corrosion anomalies based on FEA and experimental results (Mokhtari and Melchers 2018; Mokhtari and Melchers 2019). Based on parametric FEA results, Chen et al. (2015) proposed a new burst capacity model that is similar to the DNV-I model but incorporates the corrosion width. Chen et al.'s model is validated by a limited number (6) of full-scale burst tests of specimens containing artificially-induced cubic corrosion features.

Zhang et al. (2018) proposed the so-called plausible profiles model, also called the Psqr model, for the FFS assessment of large corrosion features. Instead of employing the river-bottom profile, the Psqr model identifies a series of plausible profiles to characterize the corrosion morphology. The burst capacity corresponding to each plausible profile is then evaluated using the RSTRENG method, i.e. the effective area method as described in Section 4.2. Finally, the burst capacity of the corrosion feature is defined as a low percentile (e.g. 5th-percentile) value of the burst capacities corresponding to all the plausible profiles. The Psqr model has been shown to be highly accurate based on full-scale burst tests of 59 pipe specimens containing naturally-occurring or artificially-induced corrosion features (Zhang et al. 2018).

There are certain drawbacks associated with the above-described models. The 3D PCORRC is targeted at single isolated corrosion anomalies; its applicability and accuracy for large corrosion clusters are unclear. Although Chen et al.'s model is developed by considering corrosion clusters, the fact that it is validated based on a limited number of tests involving artificially-induced anomalies casts doubts on the application of the model to naturally-occurring corrosion features. The Psqr model is computationally intensive as the recommended number of plausible profiles to be generated for a given corrosion feature is nontrivial (i.e. about 500) (Zhang et al. 2018). Furthermore, a Monte Carlo simulation process is involved in the generation of a given plausible profile. The application of the Psqr model to a relatively large corrosion feature is therefore a time-consuming undertaking.

In the present study, we propose a modification of the RSTRENG model, referred to as the RSTRENG-M model, by replacing the river-bottom profile of the corrosion feature with an alternative, so-called "riverbed" profile. The riverbed profile consists of representative depths at various points along the corrosion feature whereby the representative depth at a given point is defined as the average of the maximum and average depths of the circumferential profile of the corrosion feature at this point. Based on 60 full-scale burst tests of pipe specimens containing naturally-occurring or artificially-induced corrosion features reported by Benjamin et al. (2016), Al-Owaisi et al. (2018), Zhang et al. (2018)

and Zhang et al. (2020), RSTRENG-M is shown to be more accurate than RSTRENG with marginal additional computational cost. Furthermore, RSTRENG-M is practically as accurate as but computationally more efficient than the Psqr model. To facilitate the application of RSTRENG-M to corrosion features detected and sized by inline inspection (ILI) tools, an empirical relationship between the representative and maximum depths at a given point in the profile is established based on detailed 3D profiles of a large number of naturally-occurring corrosion features on pipe specimens removed from in-service pipelines. The remaining part of the chapter is organized as follows. Section 4.2 briefly describes the RSTRENG model and effective area concept. Because the burst test data for full-scale corroded pipe specimens play an important role in the development of RSTRENG-M, the test data collected in the present study are presented in Section 4.3 before the development and validation of RSTRENG-M described in Section 4.4. Section 4.5 describes the application of RSTRENG-M in the context of ILI data, followed by concluding remarks in Section 4.6.

4.2 RSTRENG and effective area

Given the river-bottom profile of a corrosion feature as illustrated in Fig. 4.2, the RSTRENG model considers n sub-features, each feature occupying a contiguous portion of the profile. The burst capacity for the i^{th} sub-feature ($i = 1, 2, \dots, n$), $P_{b,i}$, is then evaluated as follows:

$$P_{b,i} = \frac{2t(\text{SMYS}+68.95)}{D} \frac{1-\frac{A_i}{l_i t}}{1-\frac{A_i}{M_i l_i t}} \quad (4.1)$$

$$M_i = \begin{cases} \sqrt{1 + 0.6275 \frac{l_i^2}{Dt} - 0.003375 \frac{l_i^4}{(Dt)^2}} & \frac{l_i^2}{Dt} \leq 50 \\ 3.3 + 0.032 \frac{l_i^2}{Dt} & \frac{l_i^2}{Dt} > 50 \end{cases} \quad (4.2)$$

where D and t are the pipe diameter and wall thickness, respectively; SMYS is the specified minimum yield strength of the pipe steel; SMYS + 68.95 MPa is the empirically defined flow stress; A_i and l_i are the area and length, respectively, of the portion of the river-bottom profile occupied by the i^{th} sub-feature, and M_i is the corresponding Folias factor. The burst capacity of the corrosion feature, P_{b-RST} , is then defined as the smallest value of the burst capacities of all n sub-features:

$$P_{b-RST} = \min\{P_{b,i}\} \quad (i = 1, 2, \dots, n) \quad (4.3)$$

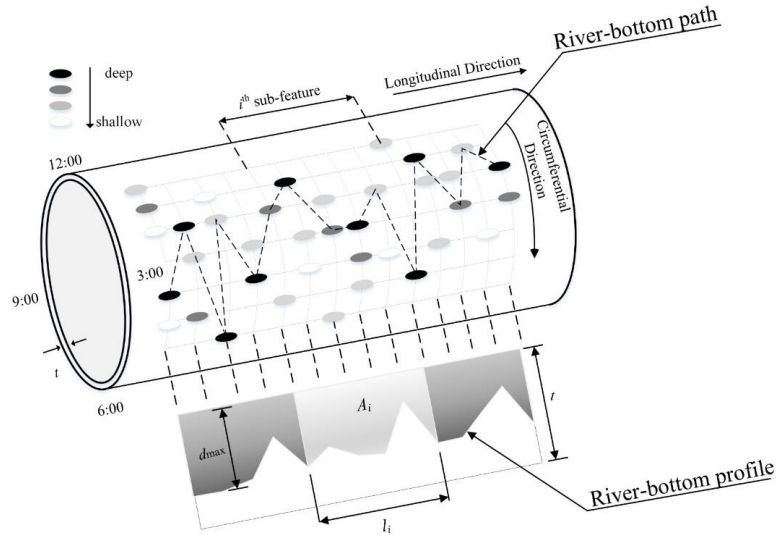


Figure 4.2 Illustration of the river-bottom profile and sub-features in the RSTRENG model

Consider $P_{b-RST} = P_{b,r}$ ($r = 1, 2, \dots, \text{or } n$). Then A_r and l_r are the so-called effective area and length, respectively, of the corrosion feature. It follows that RSTRENG is also known as the effective area method.

4.3 Full scale burst tests

Sixty (60) full-scale burst tests of corroded pipe specimens reported in the literature (Benjamin et al. 2016; Al-Owaisi et al. 2018; Zhang et al. 2018; Zhang et al. 2020) are collected in this study. Sixteen of the 60 specimens were removed from in-service pipelines and contain naturally-occurring corrosion features on the external surfaces of the specimens (Zhang et al. 2018; Zhang et al. 2020), whereas the other 44 specimens contain artificially-induced corrosion features of cubic or semi-ellipsoidal shape. The 3D profiles of corrosion features on the 16 naturally corroded pipe specimens are obtained from high-resolution laser-scanning devices. Each of the 16 specimens contains many individual corrosion anomalies, which are grouped into clusters by the widely used $1 \text{ inch} \times 6t$ interaction rule (ASME 2019). This interaction rule states that two adjacent corrosion anomalies are considered to interact with each other and therefore belong to the same cluster if their longitudinal and circumferential separation distances are less than or equal

to 25.4 mm (i.e. 1 inch) and $6t$, respectively. The 16 specimens contain 667 corrosion clusters in total. For each specimen, the corrosion cluster at which failure initiated during the burst test is identified because the burst capacity of the specimen observed in the test is considered the burst capacity of the cluster. Figure 4.3 shows a portion of the corroded external surface of one of the 16 specimens with the corrosion depth (in the unit of $\%t$) displayed by the grayscale. The longitudinal coordinate represents the relative distance of a measurement point with respect to the upstream girth weld, and the circumferential coordinate is the circumferential position (arclength) of the measurement point in terms of the 12:00 o'clock position (Fig. 4.2). The dash-lined box in Fig. 4.3 indicates a specific cluster, which consists of 262 single corrosion anomalies.

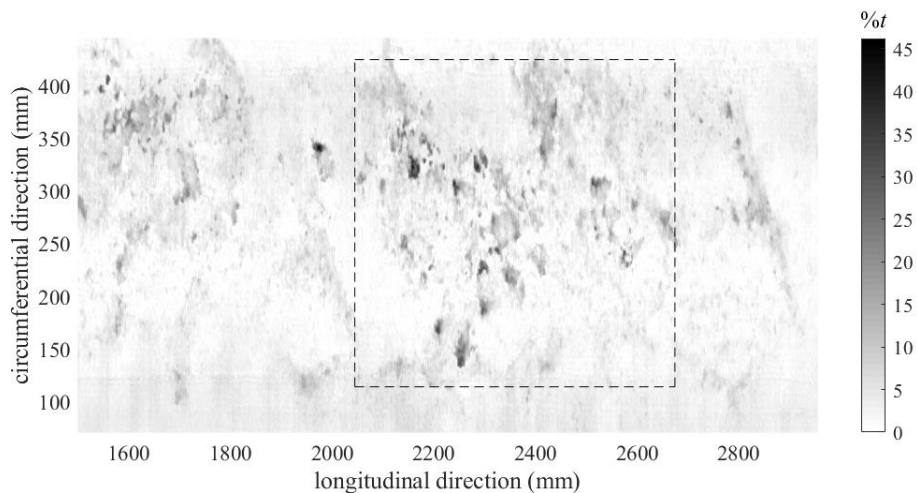
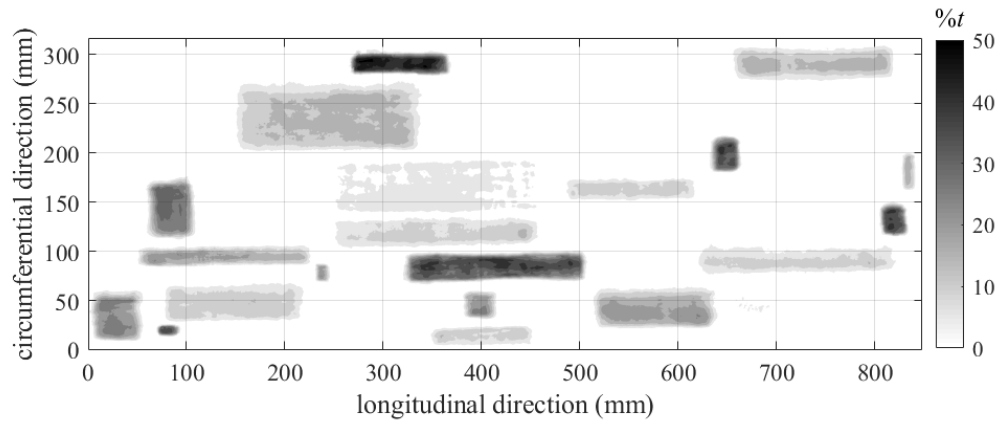


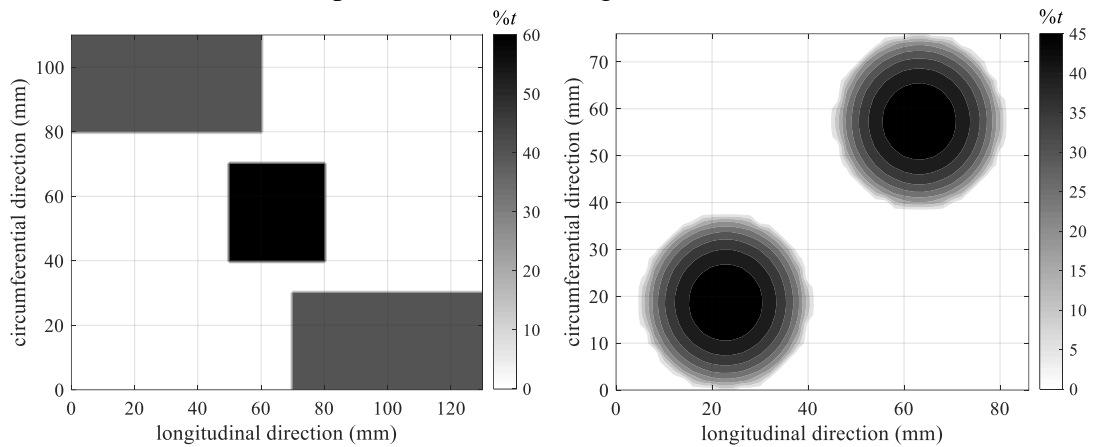
Figure 4.3 A portion of the naturally corroded external surface of a pipe specimen in Zhang et al. (2018) and Zhang et al. (2020)

The reference (Zhang et al. 2020) also includes 14 specimens that contain artificially-induced corrosion clusters. Each of the 14 specimens contains one corrosion cluster that consists of a series of (between 18 and 345) cubic individual anomalies with different widths, depths and lengths. Sixteen specimens are reported by Benjamin et al. (2016), with each of them containing an artificially-induced corrosion cluster consisting of cubic individual anomalies in different geometries ranging in number between 2 and 10. Finally, 14 specimens are reported by Al-Owaisi et al. (2018) with each of them including an artificially-induced cluster consisting of two identical semi-ellipsoidal-shaped anomalies. The corrosion clusters on three representative specimens reported in Zhang et al. (2020),

Benjamin et al. (2016) and Al-Owaisi et al. (2018), respectively, are shown in Fig. 4.4. The geometric and material properties of the 60 pipe specimens, as well as the corresponding defect information are summarized in Table 4.1. The burst capacities of the specimens observed in the test (P_{test}) are also included in Table 4.1.



a) Specimen 8-1 in Zhang et al. (2020)



b) Specimen IDTS 15 in Benjamin et al. (2016) c) Specimen 3 in Al-Owaisi et al. (2018)

Figure 4.4 Corrosion clusters on representative pipe specimens reported in Benjamin et al.(2016), Al-Owaisi et al. (2018) and Zhang et al. (2020)

Table 4.1 Summary of full-scale burst test data collected in the present study

No.	Source	Specimen ID	D (mm)	t (mm)	Steel grade	P_{test} (MPa)	Cluster at which burst initiates		σ_y (MPa)
							l (mm)	d_{max} (% t)	
1		16-1	408.2	6.2	X52	14.60	844	33	371
2		16-2	407.7	6.2	X52	13.31	1160	47	371
3		16-3	407.7	6.2	X52	13.52	330	43	371
4		16-5	407.7	5.9	X52	11.86	356	97	397
5		16-6	407.4	5.9	X52	12.72	344	57	412
6		16-7	407.4	6.0	X52	12.84	542	87	412
7		20-3	508.0	6.5	X52	10.22	362	39	395
8		24-1	610.5	6.8	X70	14.21	1504	30	555
9		24-2	610.5	6.7	X70	14.37	428	39	555
10		30-1	763.2	8.4	X70	12.31	4326	68	534
11		30-2	763.4	8.5	X70	14.10	430	48	530
12	Zhang et al. (2018);	30-3	763.2	8.4	X70	14.78	610	73	560
13		30-4	763.7	8.5	X70	12.48	710	78	511
14	Zhang et al. (2020)	30-5	762.9	8.4	X70	12.26	782	59	549
15		30-6	764.1	8.4	X70	12.96	1450	75	510
16		30-7	762.0	9.9	X52	11.11	1110	51	378
17		8-1	219.1	5.7	X52	19.98	848	52	410
18		8-2	219.1	5.7	X52	20.18	1052	48	410
19		12-1	323.9	6.2	X52	17.51	431	44	401
20		12-2	323.9	6.2	X52	17.03	433	46	401
21		20-1	508.0	9.5	X70	21.37	932	72	546
22		20-2	508.0	9.5	X70	22.08	552	75	546
23		24-3	609.6	9.0	X70	20.68	942	53	562
24		24-4	609.6	9.0	X70	19.85	421	53	562
25		34-1	863.6	11.7	X70	18.49	572	78	559
26		36-1	914.4	11.8	X70	17.60	580	49	569
27		42-1	1066.8	14.3	X70	18.61	303	64	572
28		42-2	1066.8	14.4	X70	17.49	816	58	548
29		48-1	1219.2	11.5	X70	11.97	546	67	542
30		48-2	1219.2	11.6	X70	13.42	550	69	619
31		IDTS 15	458.6	7.9	X70	24.00	130	60	639
32		IDTS 16	458.6	7.9	X70	23.40	190	60	662
33		IDTS 17	458.6	7.9	X70	21.20	320	60	662
34		IDTS 18	458.6	7.9	X70	22.70	170	60	662
35		IDTS 19	458.6	7.9	X70	23.30	210	60	662
36		IDTS 20	458.6	7.9	X70	20.80	430	60	654
37	Benjami n et al. (2016)	IDTS 21	458.6	7.9	X70	22.60	240	60	654
38		IDTS 22	458.6	7.9	X70	20.30	210	60	654
39		IDTS 23	458.6	7.9	X70	21.50	270	60	654
40		IDTS 24	458.6	8.0	X70	20.50	260	60	652
41		IDTS 25	458.6	8.0	X70	19.90	340	60	652
42		IDTS 26	458.6	8.0	X70	19.80	340	60	652
43		IDTS 27	458.6	8.0	X70	21.30	320	60	652
44		IDTS 28	458.6	7.9	X70	23.20	130	60	580
45		IDTS 29	458.6	7.9	X70	23.40	130	60	580
46		IDTS 30	458.6	7.9	X70	21.10	320	60	580

(continued on next page)

Table 4.1 (Continued)

No.	Source	Specimen ID	D (mm)	t (mm)	Steel grade	P_{rest} (MPa)	Cluster at which burst initiates		σ_y (MPa)
							l (mm)	d_{max} (% t)	
47		3	508	9.7	X60	19.05	81	49	456
48		4	508	9.6	X60	19.35	90	49	456
49		9	508	9.6	X60	19.62	80	50	456
50		10	508	9.5	X60	19.38	89	50	456
51		12	508	10.7	X60	24.17	107	49	506
52		13	508	10.7	X60	25.00	117	49	506
53		14	508	10.7	X60	24.32	128	49	506
54		19	508	9.9	X52	19.11	80	48	372
55	Al-Owaisi et al. (2018)	20	508	9.7	X52	19.59	110	49	372
56		21	508	9.7	X52	19.65	120	49	372
57		22	508	9.8	X52	20.08	130	49	372
58		23	508	9.8	X52	20.27	139	48	372
59		30	508	9.7	X52	20.68	76	49	372
60		31	508	9.7	X52	19.67	76	49	372

Note: Specimens #1 to #16 contain naturally occurring corrosion clusters; specimens #17 to #60 contain artificially induced corrosion clusters.

4.4 RSTRENG-M model

4.4.1 Model description

The riverbed profile as employed in RSTRENG-M is illustrated in Fig. 4.5. A total of m circumferential planes are employed to intersect the corrosion feature shown in Fig. 4.5. The intersection between the j^{th} ($j = 1, 2, \dots, m$) circumferential plane and corrosion feature results in a circumferential profile S_j (Fig. 4.5) for the feature. It is assumed in RSTRENG-M that the part of the corrosion feature no deeper than $0.1t$ has a negligible impact on the burst capacity (CSA 2019) and is therefore ignored in the model. Let $d_{max,j}$ and $d_{avg,j}$ denote the maximum and average depths, respectively, of the portion of S_j that is deeper than $0.1t$. It follows that $d_{max,j}$ and $d_{avg,j}$ will vanish if the entire S_j is no deeper than $0.1t$. Whereas the river-bottom profile is the longitudinal projection of the path that connects the deepest points within the corrosion feature, the riverbed profile is the longitudinal projection of the path that connects $d_{rep,j}$ for $j = 1, 2, \dots, m$, where $d_{rep,j}$ is the representative depth of S_j and defined as,

$$d_{rep,j} = qd_{max,j} + (1 - q)d_{avg,j} \quad (4.4)$$

In Eq. (4.4), q ($0 \leq q \leq 1$) is a weighting factor that defines the relative contributions of $d_{max,j}$ and $d_{avg,j}$ to $d_{rep,j}$. It follows that RSTRENG-M considers the influences on the burst

capacity of both the maximum defect depth (i.e. $d_{max,j}$) and overall metal loss (i.e. $d_{avg,j}$) at a given circumferential plane, as opposed to $d_{max,j}$ only in the RSTRENG model. Note that RSTRENG-M reverts to the RSTRENG model for $q = 1$. The riverbed profile in RSTRENG-M can be interpreted as consisting of a series of representative depths characterizing the “underwater” portion of the corrosion feature, i.e. the portion that is deeper than $10\%t$. Once the riverbed profile is obtained, the effective area method as described in Section 4.2, i.e. Eqs. (4.1) through (4.3), can be applied to compute the burst capacity.

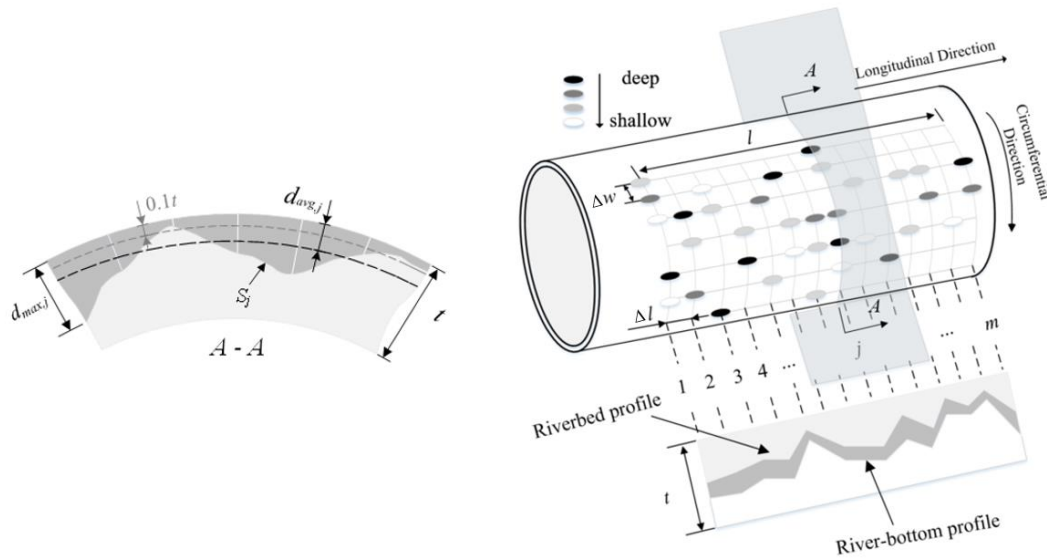


Figure 4.5 Illustration of the circumferential and riverbed profiles in RSTRENG-M

The value of q in Eq. (4.4) is determined by comparing the burst capacities predicted by RSTRENG-M (P_{b-RSM}) with the observed burst capacities (P_{test}) for the 16 specimens containing naturally-occurring corrosion features reported in Zhang et al. (2018) and Zhang et al. (2020), i.e. specimens #1 through #16 in Table 4.1. Figure 4.6 depicts the mean value and coefficient of variation (COV) of the test-to-predicted ratios (P_{test}/P_{b-RSM}) corresponding to different values of q between zero and unity. The figure indicates that the COV of P_{test}/P_{b-RSM} is minimized at $q = 0.48$, whereas the mean of P_{test}/P_{b-RSM} , as expected, monotonically increases (i.e. the model prediction becomes more conservative) as q increases from zero to unity. Given that the COV is insensitive to q in the vicinity of $q = 0.48$ as shown in Fig. 4.6, it is proposed to set q equal to 0.5 for simplicity and a

convenient interpretation of the representative depth. It follows that $d_{rep,j}$ is defined as the average of $d_{max,j}$ and $d_{avg,j}$, i.e.

$$d_{rep,j} = \frac{d_{max,j} + d_{avg,j}}{2} \quad (j = 1, 2, \dots, m) \quad (4.5)$$

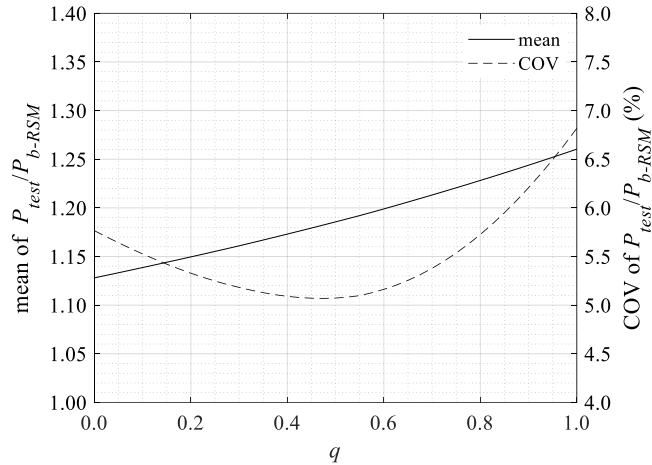


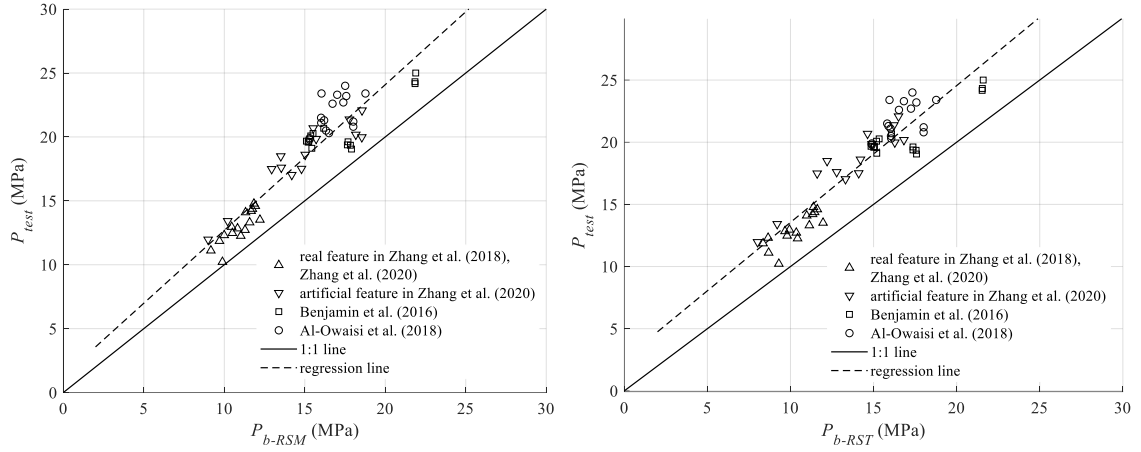
Figure 4.6 Mean and COV of test-to-predicted burst capacity ratios for RSTRENG-M as a function of the weighting factor q

4.4.2 Model validation

The full-scale test data summarized in Table 4.1 are used to validate RSTRENG-M. For comparison, the RSTRENG and Psqr models are also employed to predict the burst capacities of the specimens, denoted by P_{b-RST} and P_{b-PSQR} , respectively. Note that σ_y included in Table 4.1 are the actual (as opposed to nominal) yield strengths of the specimen and are employed in the RSTRENG, RSTRENG-M and Psqr models.

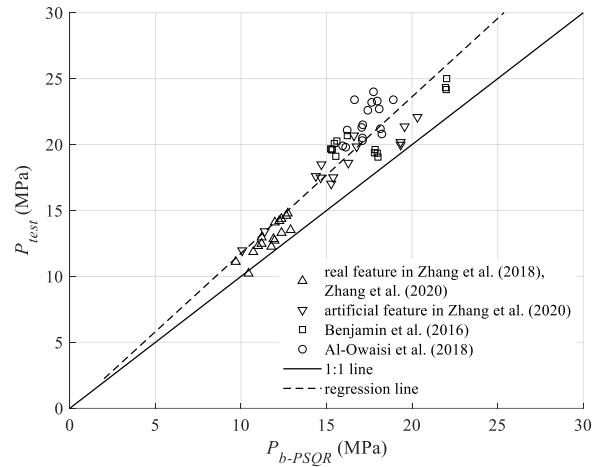
The test and predicted burst capacities are compared in Figs. 4.7(a), 4.7(b) and 4.7(c) for the RSTRENG-M, RSTRENG and Psqr models, respectively. Figure 4.7 indicates that the RSTRENG and RSTRENG-M models generally underpredict (i.e. being conservative) P_{test} , while the Psqr model overpredicts the burst capacity for one of the 16 specimens (specimen #7 in Table 4.1) removed from in-service pipelines. The regression lines in the figure suggest that the Psqr and RSTRENG-M tend to be slightly more conservative for larger values of P_{test} , whereas RSTRENG is more or less consistent for the entire range of P_{test} . The mean and COV of the test-to-predicted ratios are summarized in Table 4.2 for

different burst test datasets. Table 4.2 indicates that the RSTRENG-M and Psqr models lead to on average more accurate predictions than the RSTRENG model: the means of P_{test}/P_{b-RSM} , P_{test}/P_{b-PSQR} and P_{test}/P_{b-RST} are 1.23, 1.18 and 1.29, respectively, with the corresponding COVs equal to 7.4, 7.7 and 8.1%, respectively. The mean of P_{test}/P_{b-RSM} equals 1.23 (1.18 for naturally-occurring corrosion features) suggests that RSTRENG-M is perhaps somewhat conservative. We argue that the conservatism can be addressed without much difficulty in practice by using, for example, a simple multiplicative correction factor applied to the model prediction. Table 4.2 also indicates that the improvement in the predictive accuracy of RSTRENG-M over that of RSTRENG is most significant for the naturally-occurring and artificially-induced corrosion clusters reported in Zhang et al. (2018) and Zhang et al. (2020). Note that each of the clusters in Zhang et al. (2018) and Zhang et al. (2020) contains markedly more single anomalies than a given artificially-induced cluster reported in Benjamin et al. (2016) and Al-Owaisi et al. (2018) (see Fig. 4.4 for example). This suggests that RSTRENG-M is particularly advantageous for corrosion features with relatively complex morphologies. The predictive accuracy of the Psqr model is comparable to that of RSTRENG-M; however, the computational efficiency of the latter is an important consideration in the trade-off between the accuracy and efficiency of burst capacity models in practice. It is further noticed in Table 4.2 that predictions of all three models are on average more conservative for the 16 artificially defected pipe specimens reported by Benjamin et al. (2016) than those for the 16 naturally corroded specimens. This can be attributed to that the interaction rule used to group individual anomalies into a feature (i.e. cluster) is likely too conservative for the specimens in Benjamin et al. (2016), as evident from photographs of specimen rupture planes provided in Benjamin et al. (2016). For the naturally corroded specimens, the interaction rule is more accurate because the individual anomalies within a given cluster are generally quite close to each other. This may also be used to explain the more conservative predictions for the 16 artificially corroded specimens reported in Zhang et al. (2020), although photographs of the actual specimen rupture planes are unavailable for the specimens reported in Zhang et al. (2020).



a) RSTRENG-M

b) RSTRENG



c) Psqr Model

Figure 4.7 Comparison of test and predicted burst capacities for RSTRENG-M, RSTRENG and Psqr models

Table 4.2 Mean and COV of Test-to-predicted ratios for different burst test datasets

Burst test dataset		P_{test}/P_{b-RST}	P_{test}/P_{b-RSM}	P_{test}/P_{b-PSQR}
16 specimens in Zhang et al. (2018) and Zhang et al. (2020) – natural corrosion features	Mean	1.26	1.18	1.11
	COV (%)	6.8	5.1	5.0
14 specimens in Zhang et al. (2020) – artificial features	Mean	1.35	1.24	1.15
	COV (%)	7.5	6.9	5.9
16 specimens in Benjamin et al. (2016) – artificial features	Mean	1.32	1.30	1.26
	COV (%)	5.8	5.6	5.5
14 specimens in Al-Owaisi et al. (2018) – artificial features	Mean	1.21	1.19	1.19
	COV (%)	7.9	7.9	7.9
All 60 specimens	Mean	1.29	1.23	1.18
	COV (%)	8.1	7.4	7.7

4.4.3 Impact of resolution of riverbed profile

The application of RSTRENG-M to a given corrosion feature involves discretizing the feature using m circumferential planes as well as discretizing each circumferential profile (i.e. S_j in Fig. 4.5) to evaluate $d_{rep,j}$. The sensitivity of the predicted burst capacity to the resolution of the discretization is investigated in this section. Two types of resolution are considered, namely the longitudinal resolution Δl (i.e. $\Delta l = l/(m-1)$) and circumferential resolution Δw (Fig. 4.5). It is reasonable to assume that Δl governs the resolution of the riverbed profile for the application of the effective area method; in other words, the total number of sub-features (i.e. n) considered in the effective area method is completely dependent on Δl (or the value of m). In the validation of RSTRENG-M described in the previous section, both Δl and Δw are set to equal 2 mm. In the sensitivity analysis, Δl is set to equal one of three values, i.e. 2, 6 and 12 mm; the same set of values is also assigned to Δw . This results in a total of nine sets of values of Δl and Δw , i.e. $\Delta l \times \Delta w = 2 \times 2$ mm, 2×6 mm, ..., 12×12 mm. The means and COVs of P_{test}/P_{b-RSM} for the specimens in Table 4.1 corresponding to the nine sets of Δl and Δw values are summarized in Table 4.3.

For the naturally-occurring corrosion features, the results in Table 4.3 indicate that the longitudinal resolution Δl has no impact on burst capacities evaluated by RSTRENG-M for Δl ranging from 2 to 12 mm. On the other hand, a smaller value of Δw leads to on average more conservative predictions and a lower COV of the test-to-predicted ratios. This is

because a more refined circumferential resolution is able to better capture the maximum depth of each circumferential profile, thus leading to more conservative predictions of the burst capacity with less variability. These results suggest that $\Delta l = 12$ mm and $\Delta w \leq 6$ mm be used in the implementation of RSTRENG-M for naturally-occurring corrosion features. Similar trend can be observed for the artificially-induced corrosion features that a smaller Δw results in a higher mean values of P_{test}/P_{b-RSM} and a lower COV of P_{test}/P_{b-RSM} , while the predictions tends to be more conservative and less scattered (lower COV values) with a coarser longitudinal resolution. The results in Table 4.3 also indicate that the mean values and COVs of P_{test}/P_{b-RSM} for cases with $\Delta l = \Delta w$ (= 2, 6, or 12 mm) are always consistent.

Table 4.3 Impact of riverbed resolution on the RSTRENG-M model in terms of naturally occurring and artificial corrosion features

$\Delta l \times \Delta w$ (mm \times mm)	Naturally corroded specimens (specimens #1 - #16)		Artificially defected specimens (specimens #17 - #60)	
	Mean	COV (%)	Mean	COV (%)
2 \times 2	1.18	5.1	1.26	10.1
2 \times 6	1.17	5.2	1.22	11.1
2 \times 12	1.15	5.3	1.20	12.4
6 \times 2	1.18	5.1	1.31	9.7
6 \times 6	1.17	5.2	1.26	10.1
6 \times 12	1.15	5.3	1.24	10.5
12 \times 2	1.18	5.0	1.32	9.8
12 \times 6	1.17	5.1	1.28	10.0
12 \times 12	1.15	5.3	1.26	10.1

4.5 Application to inline inspection data

In practice, detailed high-resolution 3D profiles of corrosion features are usually unavailable. For example, the laser scan is only feasible for pipe segments that are excavated and de-coated, i.e. pipe segments that have already been selected for corrosion mitigation. On the other hand, ILI tools are commonly used in practice to detect, locate and size corrosion anomalies on buried oil and gas pipelines (Kisgawy and Gabbar 2010). An ILI tool typically characterizes an irregular-shaped single corrosion anomaly as a “box” on the pipe surface as illustrated in Fig. 4.8, and each box is associated with an ILI-reported length (in the longitudinal direction), width (in the circumferential direction) and depth (in

the through-wall thickness direction). It follows that, by applying the interaction rule, a corrosion cluster identified based on the ILI data consists of a series of “boxes”. The corresponding river-bottom profile of the cluster obtained from the ILI data resembles a step function.

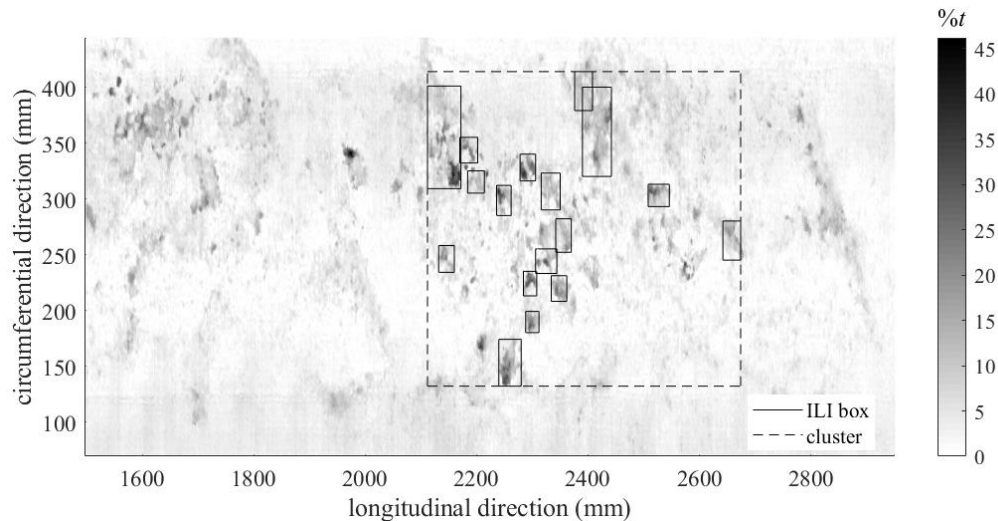
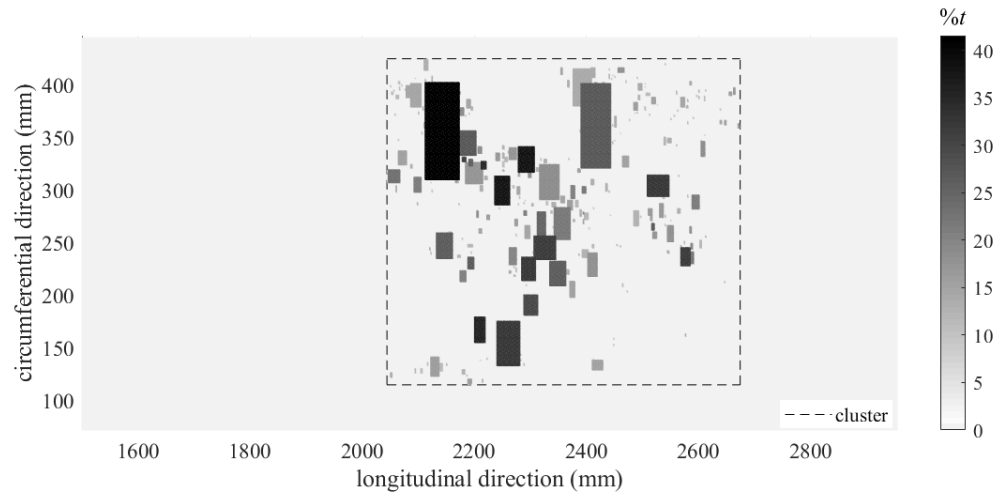


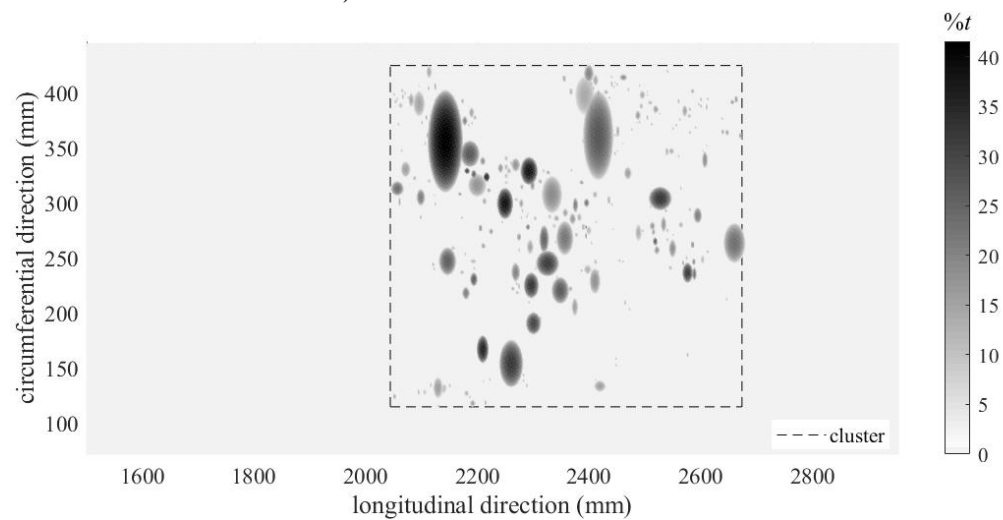
Figure 4.8 Assumed ILI-identified corrosion anomalies and cluster on specimen 16-1 in Table 4.1

The 3D shape of each box is further idealized to be either semi-ellipsoidal or cubic, with the width, length and depth of the semi ellipsoid (cube) equal to the width, length and maximum depth, respectively, of the corresponding corrosion anomaly (see Fig. 4.9). It should be emphasized that the measurement errors associated with the ILI tool in sizing corrosion anomalies (Siraj and Zhou 2019) are not considered in this study. Figure 4.10 depicts the burst capacities predicted by the RSTRENG, RSTRENG-M and Psqr models for the 14 specimens (specimens #1 to #16 excluding #4 and #6), with the means and COVs of the test-to-predicted ratios summarized in Table 4.4. Figure 4.10 and Table 4.4 indicate that all three models result in markedly conservative predictions of the burst capacities by assuming the geometry of individual anomalies to be cubic: the average under-prediction ranges from 46% (the Psqr model) to 51% (RSTRENG). By assuming individual anomalies to be semi-ellipsoidal, the conservatism in the predicted burst capacity can be reduced substantially. The mean of P_{test}/P_{b-RSM} (1.30) is almost the same as that of P_{test}/P_{b-PSQR} (1.27), and markedly lower than that of P_{test}/P_{b-RST} (1.36). Furthermore, the COV of P_{test}/P_{b-RSM} (11.1%) is markedly lower than those of P_{test}/P_{b-PSQR} and P_{test}/P_{b-RST} (both about

15%). These results illustrate the advantages of RSTRENG-M when applied to the ILI data.



a) Cubic individual anomalies



b) Semi-ellipsoidal individual anomalies

Figure 4.9 A corrosion cluster consisting of cubic and semi-ellipsoidal individual anomalies

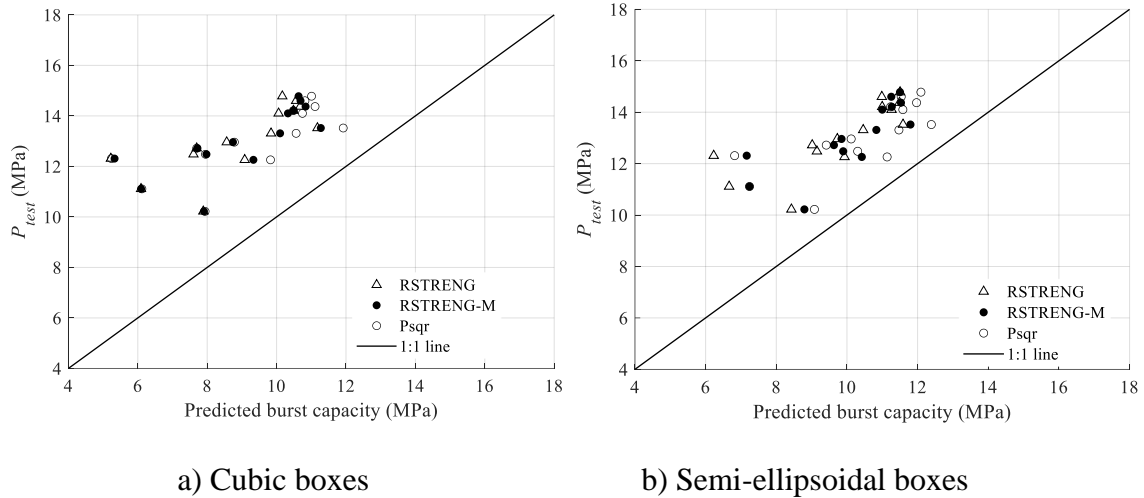


Figure 4.10 Comparison between the RSTRENG, RSTRENG-M and Psqr models based on the 14 simulated ILI measured clusters

Table 4.4 Mean and COV of Test-to-predicted ratios for 14 specimens containing naturally occurring corrosion features in the context of ILI data

Assumed geometry of individual anomalies		P_{test}/P_{b-RST}	P_{test}/P_{b-RSM}	P_{test}/P_{b-PSQR}
Cube	Mean	1.51	1.48	1.46
	COV (%)	18.7	18.7	20.7
Semi-ellipsoid	Mean	1.36	1.30	1.27
	COV (%)	15.2	11.1	14.4

To further facilitate the application of RSTRENG-M in practice, it is desirable to estimate the riverbed profile of a corrosion cluster based on the ILI data only. Since the maximum depths of individual anomalies included in the cluster are available in the ILI data, the riverbed profile can be estimated if the representative depth (d_{rep}) of a given circumferential profile is directly estimated from the corresponding maximum depth of the same circumferential profile without using Eq. (4.5). In other words, the application of RSTRENG-M is facilitated by eliminating the need to evaluate the average depth of the circumferential profile. Let d_{max-s} denote the maximum depth of a given circumferential profile S (only the portion of the profile that is deeper than $10\%t$ is considered) of the corrosion cluster – the subscript “s” is used to emphasize that d_{max-s} is associated with a given circumferential profile as opposed to the entire cluster. We attempt to develop an

empirical equation to evaluate d_{rep} from d_{max-s} based on the 16 naturally corroded specimens in Table 4.1. The 16 specimens contain 667 corrosion clusters, for which a total of 30,763 circumferential profiles are generated. The values of d_{avg-s} and d_{max-s} corresponding to these profiles are plotted in Fig. 4.11(a), which reveals a moderately strong linear correlation between these two quantities. Figure 4.11(b), which depicts values of d_{rep} and d_{max-s} , reveals a strong linear correlation between these two quantities. Given Fig. 4.11(b), the following equation is developed from the least squares analysis:

$$\frac{d_{rep}}{t} = 0.69 \frac{d_{max-s}}{t} + 0.04 \quad (d_{max-s}/t > 0.1) \quad (4.6)$$

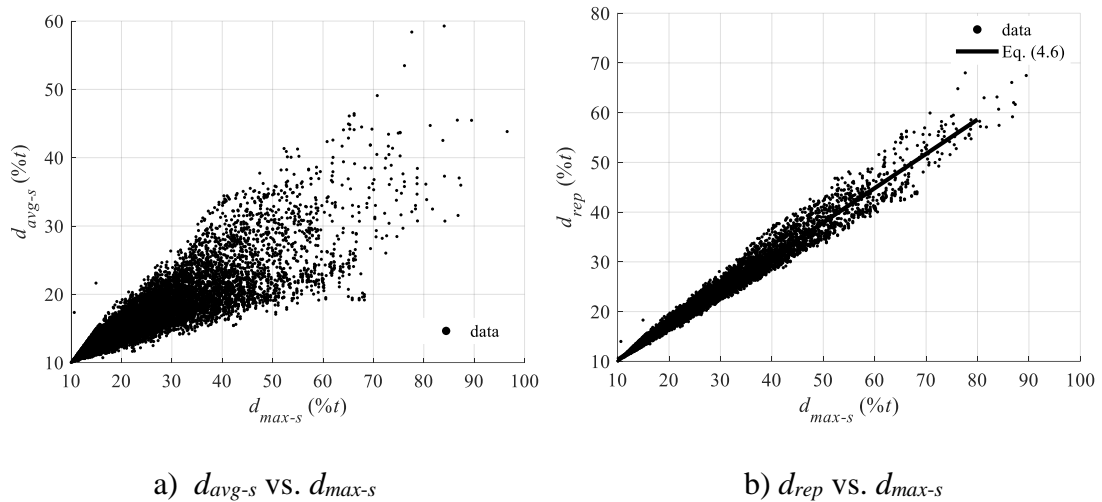
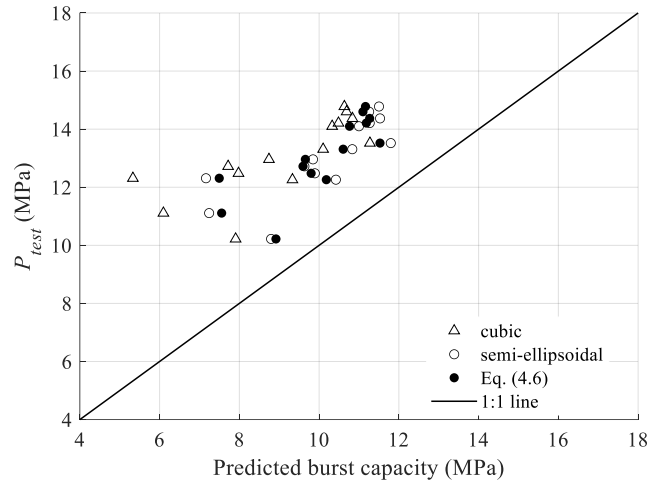


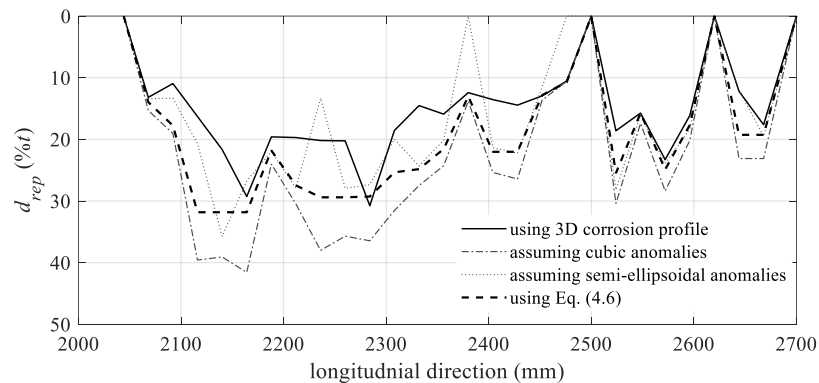
Figure 4.11 Relationships between d_{avg-s} and d_{max-s} , and d_{rep} and d_{max-s} , based on 30,763 circumferential profiles obtained from 667 clusters on 16 naturally corroded pipe specimens

Given Eq. (4.6), the riverbed profile for a corrosion cluster consisting of a set of individual anomalies detected and sized by the ILI tool can be rapidly generated by assuming each individual anomaly to be a cubic box with the corresponding length, width and depth reported by the ILI tool. This approach is employed to evaluate the burst capacities of specimens #1 through #16 (excluding #4 and #6) in Table 4.1, and the corresponding results are depicted in Fig. 4.12(a) along with the predicted burst capacities by assuming the individual anomalies to be cubic or semi-ellipsoidal boxes (without applying Eq. (4.6)). The mean and COV of the test-to-predicted burst capacity ratios corresponding to Eq. (4.6) equal 1.31 and 9.2%, respectively. Figure 4.12(b) depicts four different riverbed profiles

for a cluster on specimen 16-1 generated by using four different approaches: 1) detailed 3D corrosion profile, 2) individual anomalies assumed to be cubic boxes, 3) individual anomalies assumed to be semi-ellipsoidal boxes, and 4) individual anomalies assumed to be cubic boxes together with Eq. (4.6). The above results indicate the validity and suitability of using Eq. (4.6) to rapidly develop the riverbed profile for the application of RSTRENG-M in the context of the ILI data.



a) Comparison of predicted burst capacities



b) Comparison of riverbed profiles obtained by using different approaches for specimen 16-1 in Table 4.1

Figure 4.12 Comparisons of predicted burst capacities and the riverbed profiles when the riverbed profile is obtained by Eq. (4.6) or by assuming the corrosion anomalies as cubic and semi-ellipsoidal metal losses

4.6 Conclusion

An improvement of the well-known RSTRENG model, referred to as RSTRENG-M, is proposed in the present study to evaluate the burst capacity of corroded pipelines. RSTRENG-M differs from the RSTRENG model by employing the riverbed profile (as opposed to the river-bottom profile employed in RSTRENG) of a corrosion feature, which consists of the representative depths for a series of circumferential profiles of the feature. The representative depth for a given circumferential profile of the corrosion feature is the average of the maximum and average depths of the portion of the profile deeper than 10% of the pipe wall thickness. Given the riverbed profile, the effective area method as employed in RSTRENG is then applied to evaluate the burst capacity of the corrosion feature. The predictive accuracy of RSTRENG-M is demonstrated based on 60 full-scale burst tests of pipe specimens containing naturally-occurring or artificially-induced corrosion features reported in the literature: the mean and COV of test-to-predicted burst capacity ratios equal 1.23 and 7.4%, respectively. RSTRENG-M is shown to be more accurate than RSTRENG, in particular for corrosion clusters consisting of a large number of individual anomalies, and of similar accuracy as but more computationally efficient than the recently developed Psqr model.

The predictive accuracy of RSTRENG-M given the ILI-reported corrosion information is investigated based on the burst test data for 14 full-scale naturally corroded pipe specimens. It is observed that RSTRENG-M results in moderately conservative estimates of the burst capacity with relatively small variability (the mean and COV of the test-to-predicted ratios equal to 1.30 and 11.2%), if the individual corrosion anomalies included in a cluster are assumed to be semi-ellipsoidal-shaped with the corresponding width, length and depth reported by ILI. To further facilitate the application of RSTRENG-M in the context of ILI, a simple, empirical equation is developed to estimate the representative depth directly from the maximum depth for a given circumferential profile based on 30,763 circumferential profiles generated from a total of 667 corrosion clusters on 16 naturally corroded pipe specimens. RSTRENG-M offers a viable alternative for the fitness-for-service assessment of corroded oil and gas pipelines.

References

Al-Owaisi. S., Becker. A. A., Sun. W., Al-Shabibi. A., Al-Maharbi. M., Pervez. T., Al-Salmi. H. 2018. An experimental investigation of the effect of defect shape and orientation on the burst pressure of pressurized pipes. *Engineering Failure Analysis*. 93: 200 - 213.

ASME. 2018. Manual for determining the remaining strength of corroded pipelines. Supplement to ASME B31 Code for Pressure Piping. ASME B31G - 2018. New York, USA.

ASME. 2019. Pipeline transportation systems for liquids and slurries, ASME code for pressure piping, B31. The American Society of Mechanical Engineers, New York, USA.

Benjamin. A. C., Freire. J. L. F., Vieira. R. D., Cunha. D. J. S. 2016. Interaction of corrosion defects in pipelines - Part 2: MTI JIP database of corroded pipe tests. *International Journal of Pressure Vessels and Piping*. 145: 41 - 59.

Chen. Y., Zhang. H., Zhang. J., Li. X., Zhou. J. 2015. Failure analysis of high strength pipeline with single and multiple corrosions. *Materials and Design*. 67: 552 - 557.

CSA. 2019. Oil and gas pipeline systems, CSA Standard Z662 -19. Mississauga, Canada.

DNV. 2017. Corroded Pipelines. DNV-RP-F101 code. Det Norske Veritas. Oslo, Norway.

Kiefner. J. F. and Vieth. P. H. 1989. A modified criterion for evaluating the remaining strength of corroded pipe. Report Prepared for American Gas Association. PR3 - 805. Columbus, OH, USA.

Kishawy. H. A., Gabbar. H. A. 2010. Review of pipeline integrity management practices. *International Journal of Pressure Vessels and Piping*. 87(7): 373 - 380.

Lamontagne. M. 2002. Interaction rules - an integral factor. In: Proceedings of the NACE International Conference Corrosion. April 7 - 11. Denver, USA.

Lam. C. and Zhou. W. 2016. Statistical analyses of incidents on onshore gas transmission pipelines based on PHMSA database. *International Journal of Pressure Vessels and Piping*. 145: 29 - 40.

Leis. B. N. and Stephens. D. R. 1997. An alternative approach to assess the integrity of corroded line pipe part I: current status; part II: alternative criterion. In: Proceedings of the 7th International Offshore and Polar Engineering Conference, May 25 - 30. Honolulu, USA.

Mokhtari. M. and Melchers. R. E. 2018. A new approach to assess the remaining strength of corroded steel pipes. *Engineering Failure Analysis*. 93: 144 - 156.

Mokhtari, M. and Melchers, R. E. 2019. Next generation fracture prediction models for pipes with localized corrosion defects. *Engineering Failure Analysis*. 105: 610 - 626.

Siraj, T., Zhou, W. 2019. Quantification of measurement error in the lengths of metal-loss corrosion defects reported by inline inspection tools. *Journal of Pressure Vessel Technology*. 141: 061402.

Stephens, D. R. and Leis, B. N. 2000. Development of an alternative failure criterion for residual strength of corrosion defects in moderate-to high-toughness pipe. In: *Proceedings of the 2000 International Pipeline Conference*. IPC2000. Oct. 1 - 5. Calgary, Canada.

Zhang, S., Yan, J., Kariyawasam, S., Huang, T., Al-Amin, M. 2018. A more accurate and precise method for large metal loss corrosion assessment. In: *Proceedings of the 2018 International Pipeline Conference*. IPC2018. Sept. 24 - 28. Calgary, Canada.

Zhou, W. and Huang, G. 2012. Model error assessments of burst capacity models for corroded pipelines. *International Journal of Pressure Vessels and Piping*. 99 - 100: 1 - 8.

Zhang, S., Yan, J., Kariyawasam, S., Huang, T., Al-Amin, M. 2020. Plausible profile (Psqr) corrosion assessment model: refinement, validation and operationalization. In: *Proceedings of the 2020 International Pipeline Conference*. IPC2020. Sept. 28 – Oct. 2. Calgary, Canada.

5 A Random Field Model of External Metal-loss Corrosion on Buried Pipelines

5.1 Introduction

Metal-loss corrosion is one of the main threats to the structural integrity of buried oil and gas pipelines (Lam and Zhou 2016), and generally manifests itself as irregular-shaped features of pipe wall thinning on the external or internal surface (or both) of the pipeline. Figure 5.1 depicts two-dimensional (2D) and three-dimensional (3D) images of the corroded external surface of pipe segment #1 in Table 5.1 (see Section 5.3) based on measurements using a laser scanning device. The corrosion depth (z) in the unit of $\%t$ (t denotes the pipe wall thickness) at a given point on the surface quantifies the corresponding loss of the wall thickness at the point. The fitness-for-service (FFS) assessment of corroded pipelines in practice involves evaluating the pressure containment capacity, i.e. burst capacity, of the pipeline at corrosion features using suitable models, which are generally of the semi-empirical nature (Kiefner and Vieth 1989; Zhou and Huang 2012). An important step in the development of burst capacity models is to validate them using results of full-scale burst tests of corroded pipe specimens (Kiefner and Vieth 1989; Zhang et al. 2018). Pipe specimens containing naturally-occurring corrosion features are ideal for this purpose; however, it is a costly undertaking to obtain such specimens by extracting them from in-service pipelines. This imposes a severe constraint on the number of test specimens that can be afforded by the research program. Furthermore, it is difficult to control characteristics of the specimen (such as the diameter, wall thickness and material properties) and corrosion features (such as the maximum corrosion depth) for specimens removed from in-service pipelines. Alternatively, specimens containing artificially-induced flaws are employed in the burst tests (e.g. Benjamin et al. 2005; Al-Owaisi et al. 2018; Mokhtari and Melchers 2019). This overcomes the above-described disadvantages of specimens containing naturally-occurring corrosion; however, since artificially-induced flaws are in general regular-shaped, e.g. cubic or semi-ellipsoidal, they do not capture geometric characteristics of naturally-occurring corrosion features. Burst capacity models validated using test specimens containing artificially-induced flaws may not be suitable for practical FFS assessments. Three-dimensional (3D) elasto-plastic Finite Element Analyses (FEA) are being increasingly used to evaluate the burst capacity of corroded pipelines

(Chiodo and Ruggieri 2009; Al-Owaisi et al. 2018; Bao et al. 2018; Mokhtari and Melchers 2019). Various studies (Yoshida and Yamaguchi 2013; Bao et al. 2018; Mokhtari and Melchers 2019) reported in the literature have confirmed the high accuracy of FEA by comparing FEA-predicted burst capacities of test specimens containing naturally-occurring and artificially-induced corrosion features with the corresponding burst capacities observed in the test.

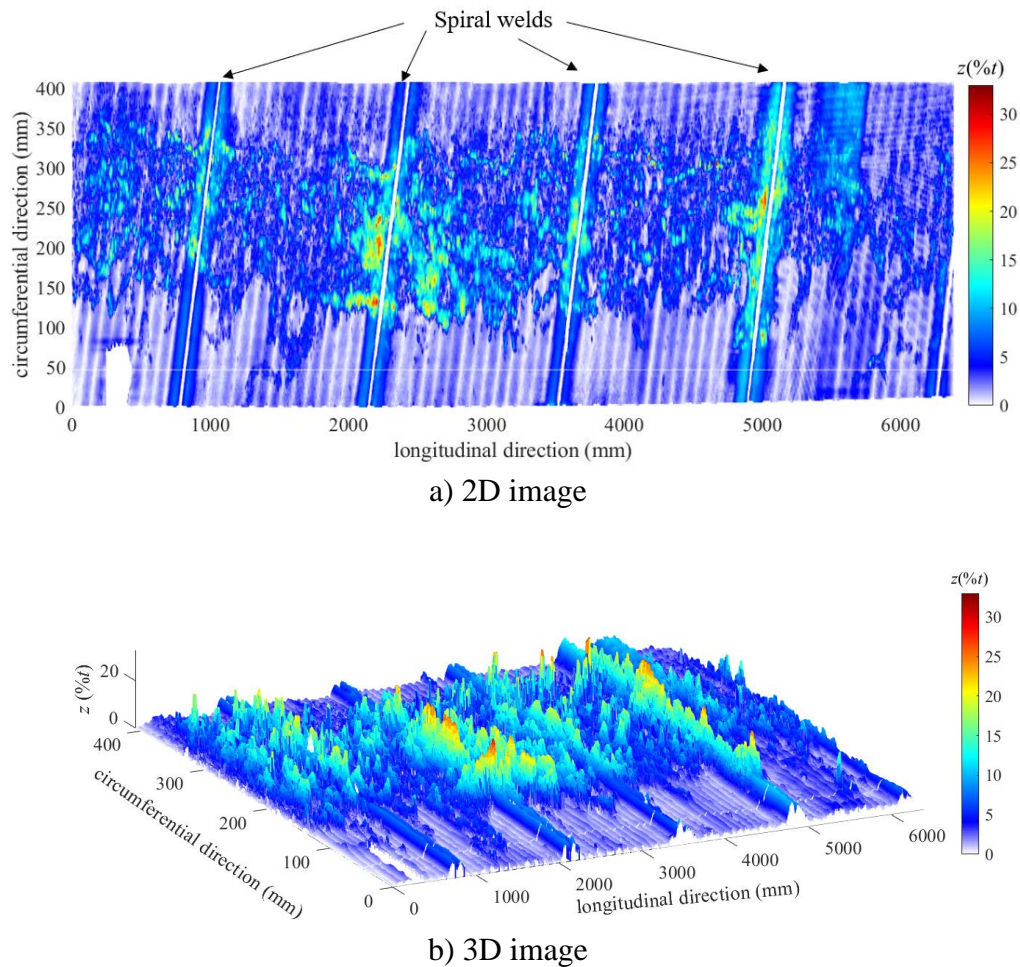


Figure 5.1 2D and 3D images of a corroded surface measured by the laser scanner

The advancement in FEA of the burst capacity of corroded pipelines motivates us to develop a random field model that can capture characteristics of naturally-occurring corrosion features and be used to stochastically simulate such features. By combining FEA with the random field-based corrosion model, full-scale burst tests of pipe specimens containing realistic corrosion features can be carried out numerically. This leads to

significant cost savings and great flexibility in selecting test parameters (e.g. pipe and corrosion geometry) as well as investigating influences of these parameters on the burst capacity of corroded pipelines. The random field corrosion model can be further employed to investigate the capacity of corroded pipelines with different configurations (e.g. pipe elbows) (Lee et al. 2015; Wang and Zhou 2019) and/or under complex loading conditions (e.g. internal pressure combined with bending) (Mohd et al. 2015; Chegeni et al. 2019). The present study focuses on modeling the external corrosion, i.e. corrosion on the external surface of the pipeline, based on high-resolution laser-scan corrosion measurements obtained from in-service pipelines. The proposed model employs a latent Gaussian random field, which is extensively used in the stochastic spatial modeling of rainfall (Bell 1987; Rasmussen 2013; Oliveira et al. 2018). The similarity between the rainfall and corrosion models is discussed in the following sections.

The remainder of this chapter is organized as follows. Section 5.2 presents a literature review of spatial models of metal-loss corrosion; Section 5.3 describes the corrosion measurement data that are the basis of the random field model proposed in this study; Section 5.4 presents the random field model, its analogy with the spatial rainfall model, a comparison between simulated and measured corrosion fields, and the impact of model parameters on the simulated field. Concluding remarks are included in Section 5.5.

5.2 Literature review

The spatial modeling of corrosion on ship structures, cast/ductile iron pipes and steel pipelines has been reported in the literature. Teixeira and Soares (2008) investigated the collapse strength of corroded steel plates in ship structures and employed a homogeneous, isotropic lognormal random field to characterize the corrosion depth on the ship plate. The authors assumed a Gaussian (squared exponential) correlation function (Vanmarcke 2010) as well as a representative value of the correlation length. Htun et al. (2013) carried out a similar study and employed the Gaussian random field to characterize the corrosion wastage on ship plates. Garbatov and Soares (2019) proposed two spatial models to characterize the thickness of corroded ship plates: the uniform density of corrosion pits with uncorrelated depths and randomly-located semi-elliptical-shaped corrosion pits with

uncorrelated shape coefficients. Ranji (2012) proposed a power spectral density function describing the nonuniform corrosion depths on both sides of a plate and simulated the corroded surface by a homogeneous Gaussian random field with the proposed power spectral density function. Li et al. (2017) assumed corrosion pits to distribute uniformly on the surface of ductile iron pipes and the growth of individual pits to follow a gamma process. The copula is employed to characterize the statistical dependence between growths of different pits. Aryai and Mahmoodian (2017) employed the Gaussian random field to model the depths of corrosion pits on the surface of cast iron water pipes and considered a time-dependent correlation length of the Gaussian random field. The corrosion measurement data obtained in the present study indicate that a significant portion of a corroded pipe surface has negligibly small corrosion depths and can be deemed corrosion free. This feature, i.e. the intermingling of corroded and corrosion-free areas on the pipe surface, cannot be dealt with by the aforementioned spatial models, but is a central component of the model proposed in the present study. Furthermore, the proposed model has the flexibility to incorporate the specific marginal distribution of the corrosion depth, which is non-Gaussian by physical constraints, and accounts for the spatial correlation between corrosion depths at different locations on the pipe surface.

5.3 Corrosion measurement data

The corrosion measurement data employed in the present study are provided by a Canadian pipeline operator. A series of naturally corroded pipe segments were removed from in-service pipelines owned by the operator for the purpose of corrosion mitigation. A portion of the external surface of each pipe segment was then scanned using a high-resolution laser-scanning device. The device measures the corrosion depths at regularly spaced points (i.e. grid points) on the pipe surface, with a grid spacing of 1 mm along the pipe longitudinal direction and 1 mm along the pipe circumferential direction, i.e. a 1×1 mm grid. Note that the circumferential grid spacing is the arc length. Table 5.1 summarizes the basic attributes of five pipe segments and corresponding laser scan data, where D is the pipe outside diameter, and L and W denote, respectively, the longitudinal and circumferential lengths of the scanned pipe surface, and z_{max} denotes the maximum corrosion depth recorded by the laser scan.

Table 5.1 Relevant information of the pipe segments in the analysis

Pipe segment	Specimen ID	D (mm)	t (mm)	L (mm)	W (mm)	z_{max} (% t)	% of grid points with z	
							≤ 2	≤ 5
1	24-1	610.5	6.8	6387	408	32	43	77
2	24-2	610.5	6.7	8080	497	39	60	90
3	30-1	763.2	8.4	6147	500	68	35	70
4	30-2	763.4	8.5	3127	461	48	58	81
5	30-3	763.2	8.4	2467	606	73	58	85

A common feature of the corrosion data obtained from the five pipe segments is that a significant portion of the measured corrosion depths on a given pipe is quite small, as indicated in the last two columns of Table 5.1. Take the corroded surface of pipe segment #1 as an example (depicted in Fig. 5.1). Out of a total of 2,606,304 grid points included in the scanned surface, 43% and 77% of them have measured corrosion depths less than $2\%t$ and $5\%t$, respectively. Note that the laser scan device is inevitably associated with measurement errors. Typical specifications of the laser scan indicate that the measured corrosion depth is within $\pm 1.5\%t$ (Applus n.d.). This suggests that the low end of measured corrosion depths contains considerable measurement noises and should be treated separately from deeper corrosion depths. From a practical standpoint, FFS assessments of corroded pipelines typically ignore shallow corrosion depths, say, $z \leq 10\%t$, as their effect on the burst capacity is negligible (CSA 2019). Based on these considerations, a threshold of $z_{th} = 5\%t$ is imposed in the present study such that any measured corrosion depths less than or equal to z_{th} are ignored with the corresponding grid points considered corrosion-free. Figure 5.2 depicts the corrosion depths of the scanned surface on pipe segment #1 after the threshold is imposed. We are therefore seeking a random field model that can capture the intermingling of corrosion-free and corroded areas on the pipe surface.

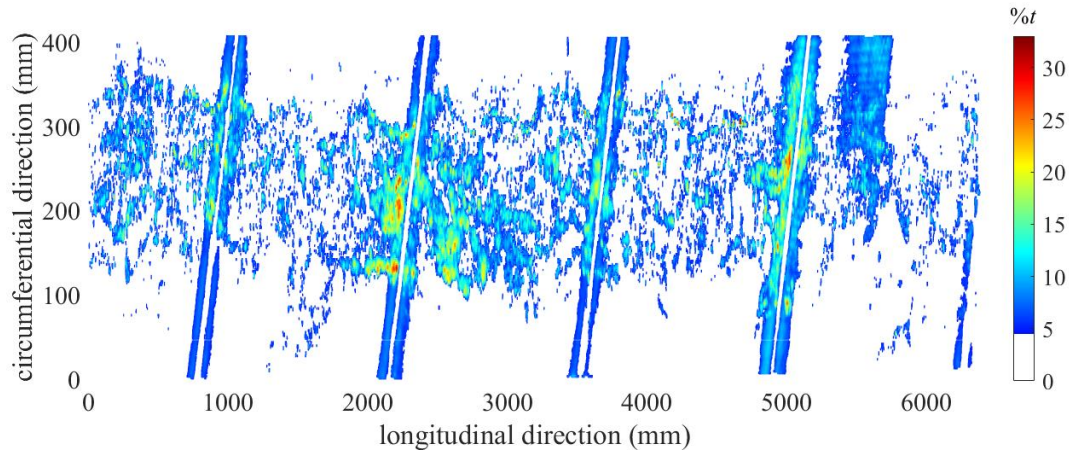


Figure 5.2 Corrosion depths on segment #1 with the corrosion threshold $z_{th} = 5\%t$ imposed

5.4 Random field model of corrosion on pipelines

5.4.1 Fundamentals

The intermingling of corrosion-free and corroded areas within a bounded region on the pipe surface is akin to the so-called spatial intermittency of rainfall (Bell 1987; Rasmussen 2013; Oliveira et al. 2018); that is, a geographical region of interest can be divided into two sub-regions at the end of a short rainfall accumulation period: a dry sub-region where there is no rainfall or rainfall below a minimum reportable amount (Wilks 1998), and a wet sub-region where the rainfall exceeds the minimum reportable amount. Rainfall models that employ one or two latent Gaussian random fields to capture the spatial characteristics of rainfall, including the intermittency, are extensively reported in the literature. For example, Bell (1987) first proposed to use a single latent Gaussian random field to characterize the rainfall occurrence (i.e. separation of dry and wet sub-regions) as well as the amount of rainfall in the wet sub-region through a suitable transformation of the Gaussian field. This approach can be considered an extension of the binary random field model (Vanmarcke 2010). Wilks (1998) and Berrocal et al. (2008) employed two independent latent Gaussian random fields to characterize the rainfall occurrence and amount, respectively. Oliveira et al. (2018) also employed two latent Gaussian random fields with the rainfall occurrence characterized by one of the fields and the rainfall amount jointly characterized by the two fields.

Inspired by the above-described spatial rainfall models, we propose to use a single latent homogeneous Gaussian random field to characterize corroded pipe surfaces. Let $Z(x, y)$ denote the random field of corrosion depths within an area of interest on the pipe surface, where x and y are the spatial coordinates, i.e. the longitudinal and circumferential positions, of a given point within the area with respect to an origin. It is assumed that the probability of having a nonzero corrosion depth at any given point within the field is f_c ($0 \leq f_c \leq 1$); in other words, the probability of the point being corrosion-free is $1 - f_c$. One may simply assume f_c to be a constant within the field. Indeed, a similar assumption was adopted by Bell (1987), who considered the probability of rainfall at any point within a bounded geographic region to be independent of the spatial position. However, this assumption is not supported by the corrosion data. As shown in Fig. 5.2, the corroded areas tend to be clustered as opposed to be uniformly distributed within the scanned surface. Therefore, f_c is considered in this study to be dependent on the spatial coordinates, i.e. $f_c = f_c(x, y)$. For notational brevity, x and y are not explicitly included in the formulations hereafter unless necessary for clarity. The nonzero corrosion depth is characterized by a cumulative distribution function (CDF) denoted by $H(z)$ that is assumed to be independent of spatial position. It follows that

$$F_Z(z) = \begin{cases} 1 - f_c & z = 0 \\ 1 - f_c + f_c H(z) & z > 0 \end{cases} \quad (5.1)$$

where $F_Z(z)$ ($z \geq 0$) denotes the CDF of Z . Let G denote the latent homogeneous Gaussian random field with a mean value of zero and a variance of unity. The correspondence between Z and G is first established by selecting a threshold g_0 in G such that G at any given point exceeds g_0 with a probability of f_c , i.e. $\text{Prob}[G \leq g_0] = 1 - f_c$ (Bell 1987; Rasmussen 2013). It follows that g_0 is given by

$$g_0 = \Phi^{-1}(1 - f_c) \quad (5.2)$$

where $\Phi^{-1}(\bullet)$ denotes the inverse of the standard Gaussian CDF $\Phi(\bullet)$. It is emphasized that g_0 is dependent on the spatial coordinates, i.e. $g_0 = g_0(x, y)$.

The complete correspondence between Z and G is then given by (Bell 1987; Rasmussen 2013),

$$z = \begin{cases} 0 & g \leq g_0 \\ H^{-1}\left(\frac{\Phi(g)-(1-f_c)}{f_c}\right) & g > g_0 \end{cases} \quad (5.3)$$

where g is a value of G , and $H^{-1}(\bullet)$ denotes the inverse of $H(z)$. The second branch of Eq. (5.3) is the inverse probability transformation between $F_Z(z)$ ($z > 0$) and $\Phi(g)$, or equivalently between $H(z)$ ($z > 0$) and a truncated Gaussian distribution ($g > g_0$). Figure 5.3 schematically illustrates the correspondence between Z and G . For easy illustration, the two-dimensional pipe surface is represented by a single horizontal axis in Fig. 5.3.

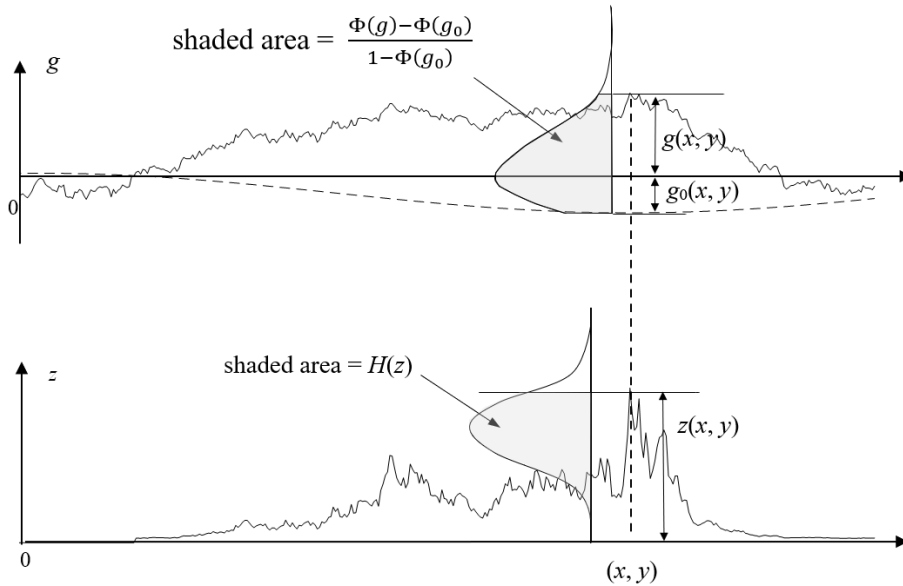


Figure 5.3 Illustration of the correspondence between Z and G

The nonzero corrosion depths within Z are assumed to be spatially correlated. The direct definition of the spatial correlation structure of Z is however difficult and ambiguous due to the existence of corrosion-free area in Z . Therefore, the spatial correlation structure of the latent Gaussian random field G is considered instead (Rasmussen 2013). It follows from G being a homogenous random field that the correlation coefficient between $G(x_1, y_1)$ and $G(x_2, y_2)$ ($(x_1, y_1) \neq (x_2, y_2)$) depends only on the separation between the two points. Let $r_G(\Delta x, \Delta y)$ denote the correlation coefficient, where $\Delta x = |x_1 - x_2|$ and $\Delta y = |y_1 - y_2|$. Given the corrosion measurement data such as that described in Section 5.3, the maximum likelihood (ML) method as described in the following can be used to estimate $r_G(\Delta x, \Delta y)$ (Rasmussen 2013). There are four scenarios in terms of values of $z_1 = z(x_1, y_1)$ and $z_2 = z(x_2, y_2)$: 1) $z_1 = z_2 = 0$; 2) $z_1 = 0$ and $z_2 > 0$; 3) $z_1 > 0$ and $z_2 = 0$, and 4) $z_1 > 0$ and $z_2 > 0$.

Let n_1, n_2, n_3 and n_4 denote the numbers of pairs of grid points that are separated by $(\Delta x, \Delta y)$ and belong to scenarios 1), 2), 3) and 4), respectively. Further let L_1, L_2, L_3 and L_4 denote the likelihood functions associated with pairs of points belonging to scenarios 1), 2), 3) and 4) respectively. Based on the correspondence between Z and G , the following expressions for L_1, L_2, L_3 and L_4 are derived (see Appendix B for the derivation):

$$L_1 = \prod_{i=1}^{n_1} \Phi_2(g_{0,1}^i, g_{0,2}^i, r_G) \quad (5.4a)$$

$$L_2 = \prod_{j=1}^{n_2} \Phi \left(\frac{g_{0,1}^j - r_G \Phi^{-1}(F_Z(z_{2,j}))}{\sqrt{1-(r_G)^2}} \right) \phi \left(\Phi^{-1}(F_Z(z_{2,j})) \right) (z_{2,j} > 0) \quad (5.4b)$$

$$L_3 = \prod_{k=1}^{n_3} \Phi \left(\frac{g_{0,2}^k - r_G \Phi^{-1}(F_Z(z_{1,k}))}{\sqrt{1-(r_G)^2}} \right) \phi \left(\Phi^{-1}(F_Z(z_{1,k})) \right) (z_{1,k} > 0) \quad (5.4c)$$

$$L_4 = \prod_{s=1}^{n_4} \phi_2 \left(\Phi^{-1}(F_Z(z_{1,s})), \Phi^{-1}(F_Z(z_{2,s})), r_G \right) (z_{1,s}, z_{2,s} > 0) \quad (5.4d)$$

where $g_{0,1}$ and $g_{0,2}$ represent values of g_0 at z_1 and z_2 , respectively, with the superscript \bullet indexing different pairs of z_1 and z_2 in scenarios 1), 2) and 3); $\Phi_2(\bullet, \bullet, r_G)$ and $\phi_2(\bullet, \bullet, r_G)$ denote, respectively, the CDF and probability density function (PDF) of a standard bivariate Gaussian distribution with a correlation coefficient of r_G (for notational brevity, $r_G(\Delta x, \Delta y)$ is simply written as r_G); $z_{2,j}$ ($j = 1, 2, \dots, n_2$) and $z_{1,k}$ ($k = 1, 2, \dots, n_3$) denote values of nonzero corrosion depths in scenarios 2) and 3), respectively, and $z_{1,s}$ and $z_{2,s}$ ($s = 1, 2, \dots, n_4$) denote values of nonzero corrosion depths in scenario 4). An estimate of r_G , \tilde{r}_G , can be obtained by maximizing the log-likelihood function for the n ($= n_1 + n_2 + n_3 + n_4$) pairs of points, i.e.

$$\tilde{r}_G = \underset{r_G}{\operatorname{argmax}} \{\ln(L_1 L_2 L_3 L_4)\} \quad (5.5)$$

By repeating the ML method to evaluate \tilde{r}_G corresponding to different values of Δx and Δy , a parametric function of $r_G(\Delta x, \Delta y)$ can be developed from curve fitting.

5.4.2 Parameter estimation

The proposed random field corrosion model is fully defined given $f_c(x, y)$, $H(z)$ and $r_G(\Delta x, \Delta y)$. Given the corrosion data described in Section 5.3, $f_c(x, y)$ is determined by calculating the fraction of grid points of nonzero corrosion depths (i.e. $z > z_{th}$) within a local area (e.g. a 10×10 mm square) of the scanned surface and assigning the calculated f_c value to the grid point at the center of the area. This calculation is repeated until f_c values for all the grid points within the scanned surface are estimated. Figure 5.4 depicts the estimated f_c values for pipe segment #1. These empirical values of $f_c(x, y)$ can be directly employed in the random field model. Alternatively, a parametric function of $f_c(x, y)$ can be developed by fitting the empirical values (see Appendix C), and then employed in the random field model.

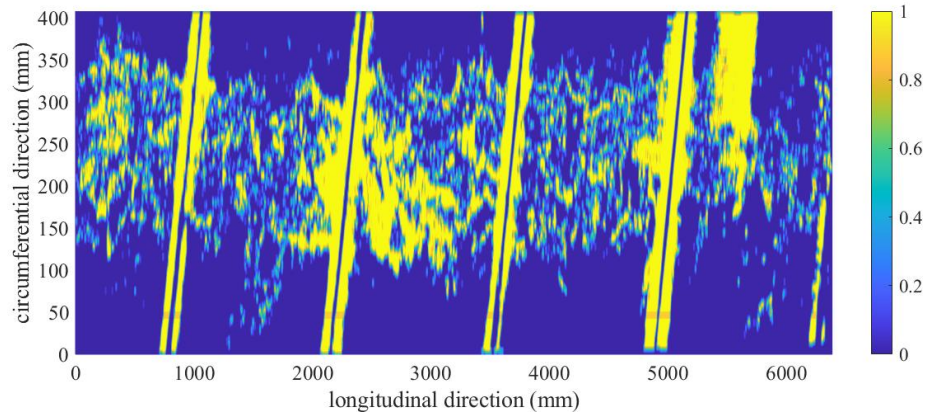


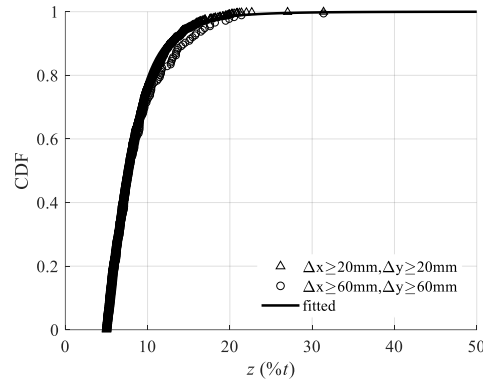
Figure 5.4 Empirical $f_c(x, y)$ values for pipe segment #1

To estimate $H(z)$, the nonzero corrosion depths at well-separated grid points within the scanned surface are extracted such that the data are close to independent and identically distributed (iid) observations. Figure 5.5 depicts the empirical CDFs of nonzero corrosion depths on the five pipe segments, corresponding to different minimum separation distances (Δx and Δy) between the grid points from which the data are extracted. It is observed that the empirical CDF for a given pipe segment remains essentially the same for Δx and Δy greater than 20 mm. Furthermore, a shifted lognormal distribution with a lower bound of z_{th} is found to fit the empirical CDF well, as also depicted in Fig. 5.5. The corrosion depths measured from the five specimens with Δx and Δy greater than 60 mm are also shown in the lognormal probability paper in Fig. 5.6. The means and coefficients of variation (COV)

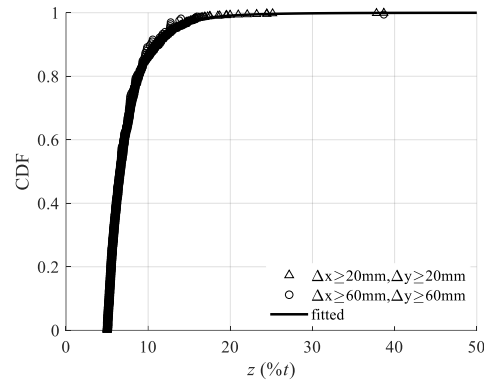
of $H(z)$, denoted by m_H and v_H respectively, are calculated based on samples of nonzero corrosion depths corresponding to $\Delta x \geq 60$ mm and $\Delta y \geq 60$ mm for the 5 pipe segments and are summarized in Table 5.2. By considering $H(z)$ as a shifted lognormal distribution with the lower bound of z_{th} , Eq. (5.3) is rewritten as follows:

$$z = \begin{cases} 0 & g \leq g_0 \\ \exp\left(\eta\Phi^{-1}\left(\frac{\Phi(g)-(1-f_c)}{f_c}\right) + \xi\right) + z_{th} & g > g_0 \end{cases} \quad (5.6)$$

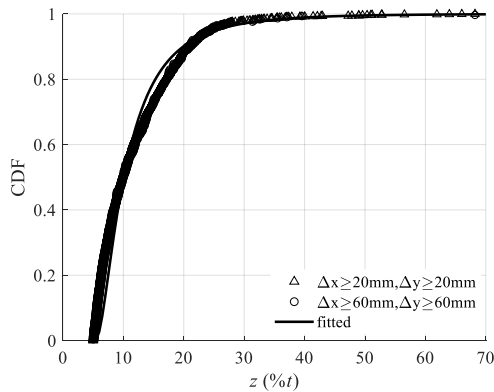
where $\eta = \sqrt{\ln\left(1 + v_H^2 \frac{m_H^2}{(m_H - z_{th})^2}\right)}$ and $\xi = \ln(m_H - z_{th}) - \frac{1}{2}\eta^2$.



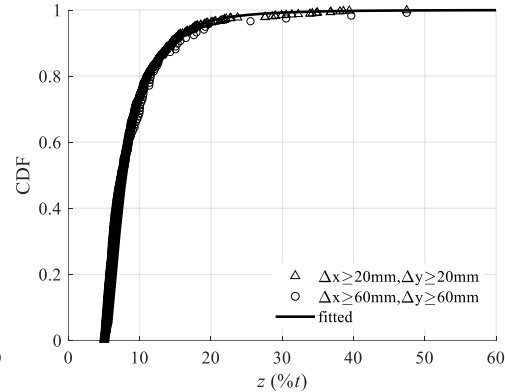
a) segment #1



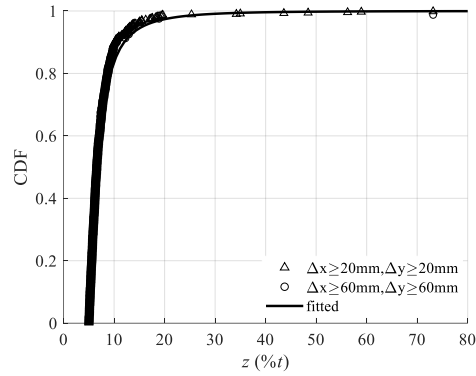
b) segment #2



c) segment #3

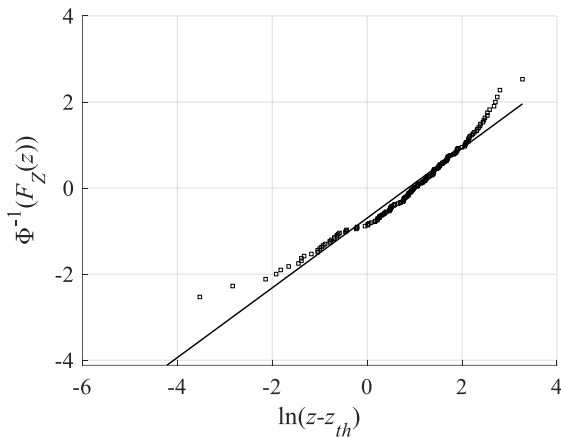


d) segment #4

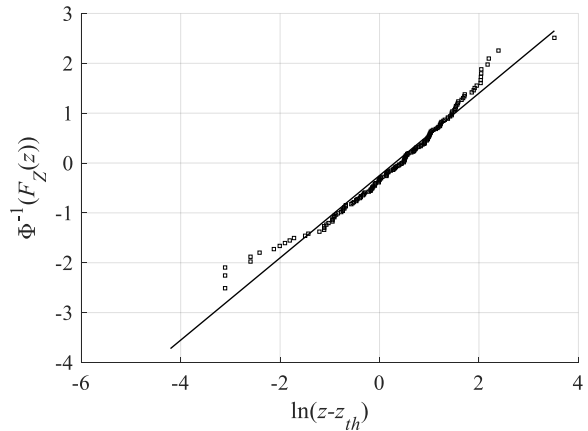


e) segment #5

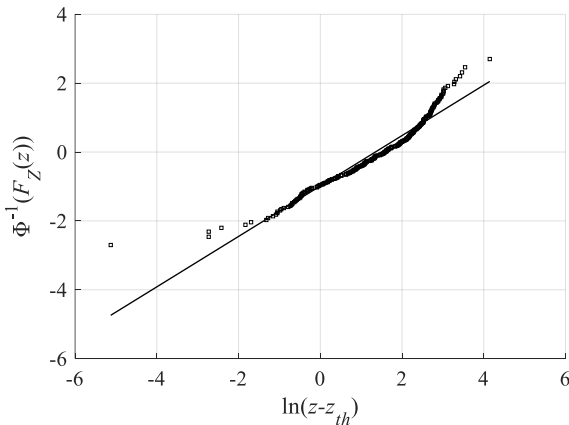
Figure 5.5 Empirical CDFs at different separation distances versus the fitted CDF for the five pipe segments in Table 5.1



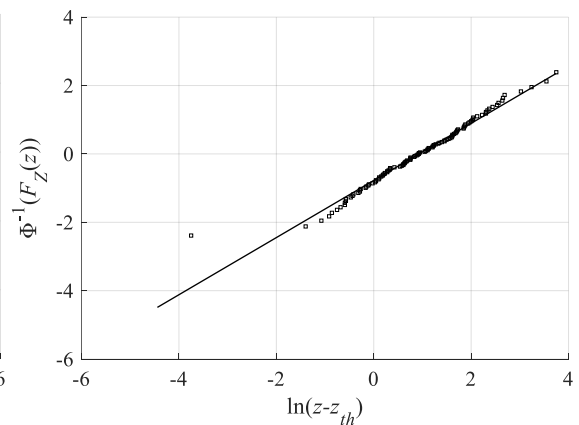
a) segment #1



b) segment #2



c) segment #3



d) segment #4

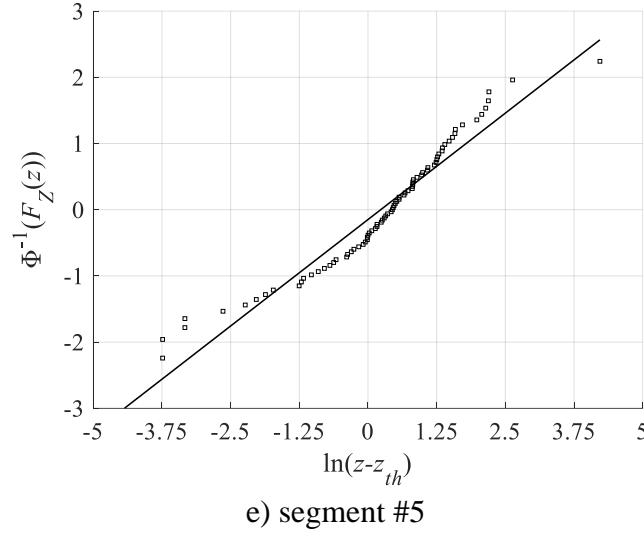


Figure 5.6 Lognormal probability papers for the corrosion depths measured with $\Delta x \geq 60$ mm and $\Delta y \geq 60$ mm on the five pipe segments in Table 5.1

Table 5.2 Parameters of the random field corrosion model for the five pipe segments

Pipe segment	m_H (%t)	v_H (%)	Δ_c (mm)
#1	8.61	39.8	45.9
#2	7.51	40.4	21.2
#3	12.23	60.1	45.6
#4	9.07	52.0	45.1
#5	7.81	68.2	54.7

Figure 5.7 depicts the values of \tilde{r}_G obtained from the ML method described in Section 5.4.1 for the five pipe segments. It is observed that \tilde{r}_G for a given pipe segment can be well fitted by the following exponential correlation model (Vanmarcke 2010):

$$r_G(\Delta_x, \Delta_y) = \exp\left(-\sqrt{\left(\frac{\Delta_x}{\Delta_{cx}}\right)^2 + \left(\frac{\Delta_y}{\Delta_{cy}}\right)^2}\right) \quad (5.7)$$

where Δ_{cx} and Δ_{cy} are the correlation lengths along the longitudinal and circumferential direction, respectively, and obtained from the curve fitting.

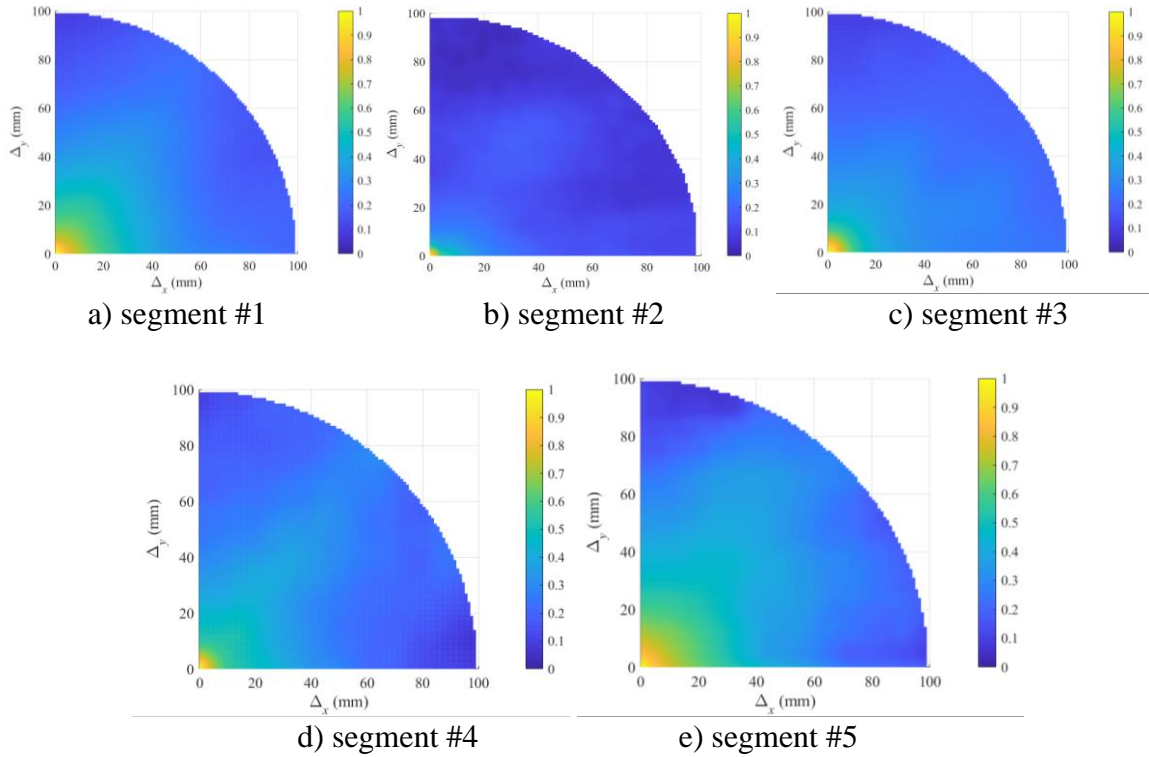
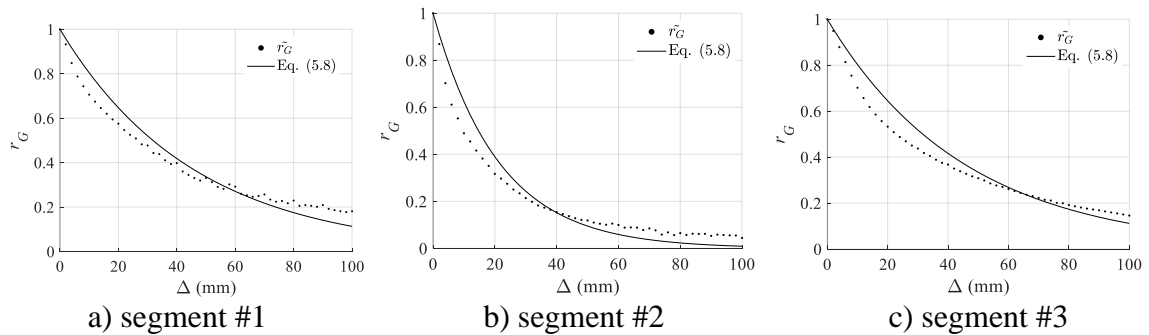


Figure 5.7 Values of \tilde{r}_G for the five pipe segments

It is further observed that Δ_{cx} and Δ_{cy} for a given pipe segment differ only marginally, generally less than 10%. Therefore, Eq. (5.7) is simplified to be the following isotropic exponential model:

$$r_G(\Delta) = \exp\left(-\frac{\Delta}{\Delta_c}\right) \quad (5.8)$$

where $\Delta = \sqrt{\Delta_x^2 + \Delta_y^2}$ and $\Delta_c = (\Delta_{cx} + \Delta_{cy})/2$. As summarized in Table 5.2, the values of Δ_c for the five pipe segments range from 21.2 to 54.7 mm. Figure 5.8 depicts Eq. (5.8) and \tilde{r}_G for the five pipe segments.



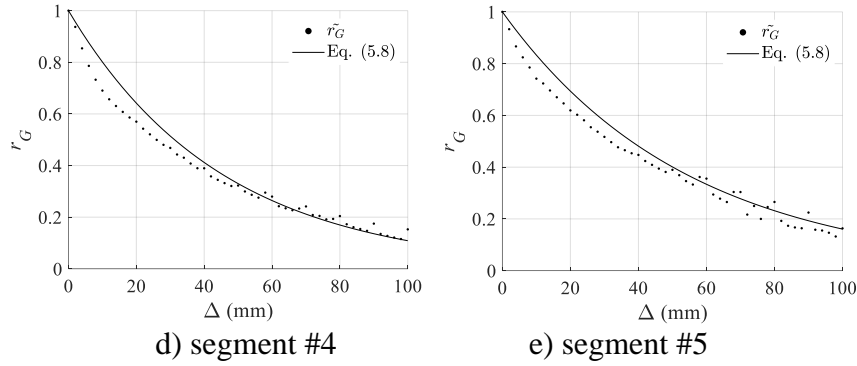
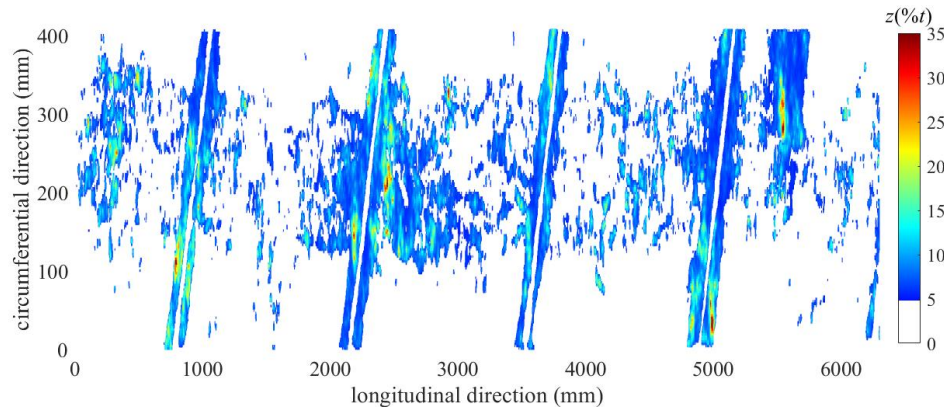


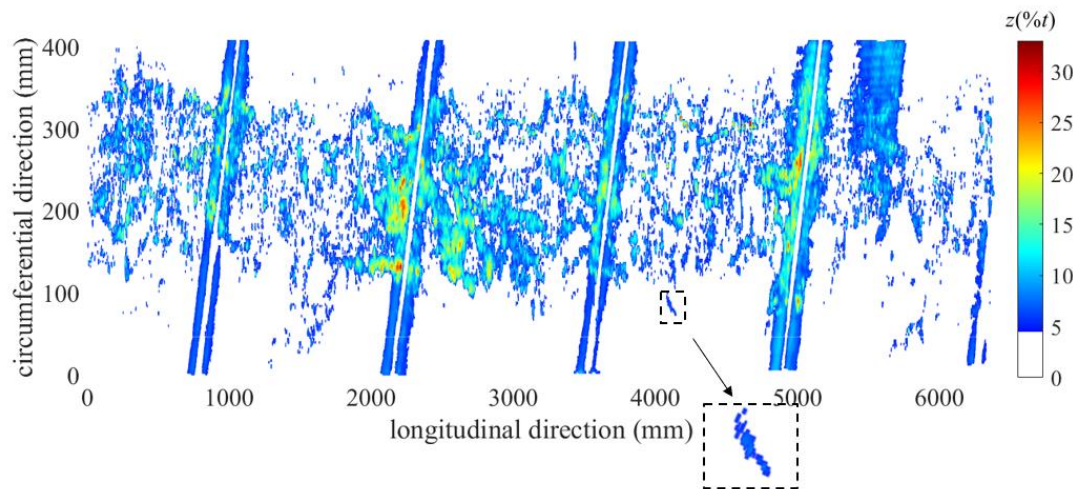
Figure 5.8 Fitting accuracy of Eq. (5.8) for the five pipe segments

5.4.3 Simulated corrosion on pipe surface

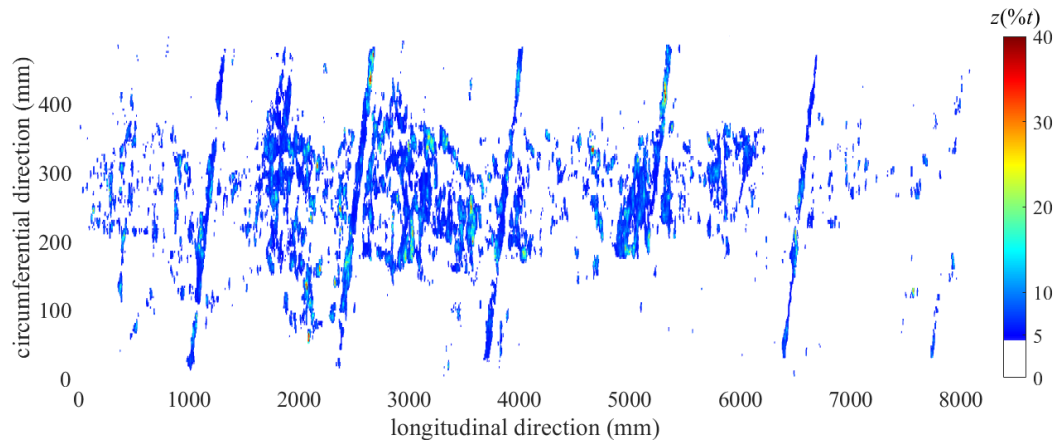
The above-described random field model is used to simulate corrosion on the pipe surface. For illustration, we simulate corrosions on pipe segments #1 and #2. The parameters of the random field model, i.e. m_H , v_H , z_{th} ($= 5\%t$), f_c and r_G , are therefore set to equal the corresponding values for the respective pipe segment. Note that the empirical values of $f_c(x, y)$ are directly employed in the simulation. The simulated corrosion field Z has the same area as that of the scanned surface for each pipe segment: an area of 6400×408 mm for pipe segment #1 and an area of 8100×498 mm for pipe segment #2. To improve the computational efficiency, a grid spacing of 3×3 mm is employed in the simulation. The latent Gaussian random field G is realized using the Karhunen-Loève (KL) expansion and Galerkin method with staircase shape functions (Ghanem and Spanos 1991). Because the size of the latent Gaussian field is much greater than its correlation length (Δ_c), the localized KL expansion method (Panunzio et al. 2018) is employed to reduce the computational cost associated with the eigen decomposition of the covariance matrix. Figures 5.9(a) and 5.9(c) depict single realizations of Z for pipe segments #1 and #2, respectively. For comparison, the scanned surfaces (with the corrosion threshold $z_{th} = 5\%t$ imposed) of pipe segments #1 and #2 are included in Figs. 5.9(b) and 5.9(d), respectively. Figure 5.9 indicates that the simulated corrosion field is similar to the measured field by observation.



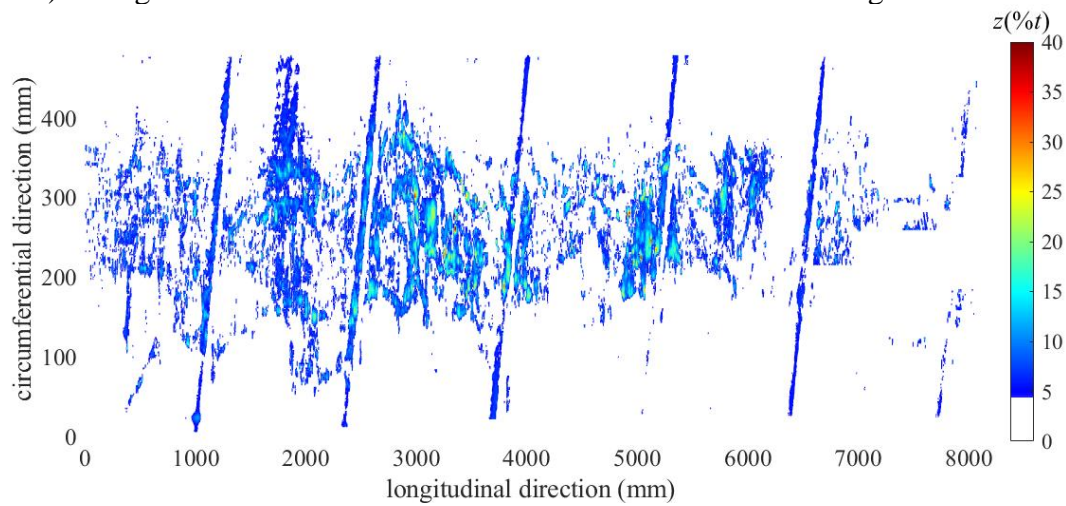
a) A single realization of the random field corrosion model for segment #1



b) scanned corroded surface of segment #1



c) A single realization of the random field corrosion model for segment #2



d) scanned corroded surface of segment #2

Figure 5.9 Comparisons between the simulated and scanned corrosion surfaces of pipe segments #1 and #2

The simulated and measured corrosion fields are more quantitatively compared based on the corrosion anomalies and clusters contained in each field. To make the comparison more meaningful, the grid size in the measured corrosion field is increased from 1×1 mm to 3×3 mm such that it is the same as the grid size in the simulated field. A corrosion anomaly is defined as an “island” of grid points with nonzero corrosion depths, as illustrated in the inset of Fig. 5.9(b). Two or more closely-spaced anomalies then form a cluster based on the so-called interaction rule (Fig. 5.10). In this study, the widely used B31.4 interaction rule (ASME 2019) is adopted to identify corrosion clusters. According to this rule, two corrosion anomalies form a cluster if both of the following two conditions are met: $S_L \leq 1$ inch and $S_C \leq 6t$ (Fig. 5.10), where S_L and S_C denote, respectively, the

longitudinal and circumferential separation distances between the anomalies. Table 5.3 compares the average number of corrosion anomalies and clusters in 100 realizations of the simulated corrosion fields and in the measured fields for pipe segments #1 and #2.

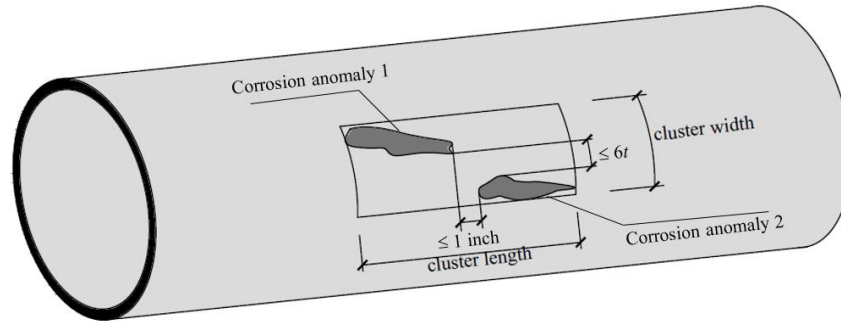


Figure 5.10 Illustration of the 1 inch \times 6t interaction rule

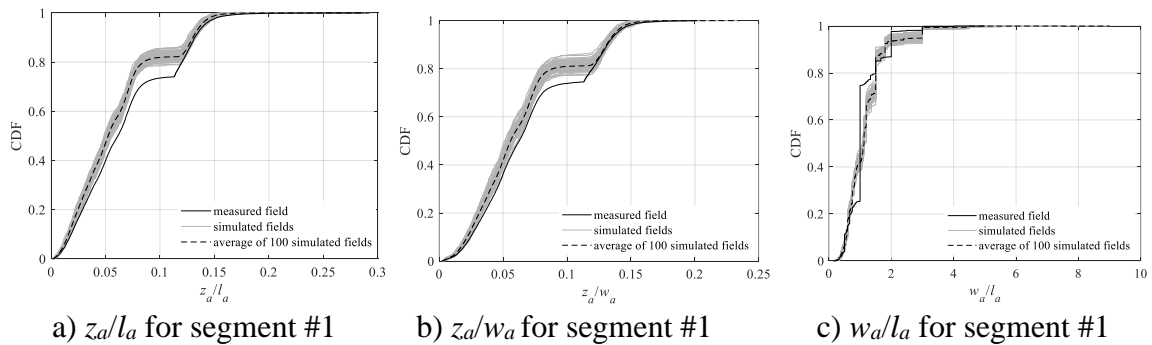
Table 5.3 Comparison between the numbers of corrosion anomalies and clusters contained in the simulated and measured fields of segment #1 and #2

	# of anomalies		# of clusters	
	Measured field	Average of 100 simulated fields	Measured field	Average of 100 simulated fields
Segment #1	2076	1511	28	29
Segment #2	1772	1405	50	75

Let l_a , w_a and z_a denote, respectively, the length, width and maximum depth of a corrosion anomaly; let l_c , w_c and z_c denote, respectively, the length, width and maximum depth of a corrosion cluster. Figure 5.11 depicts the empirical CDFs of z_a/l_a , z_a/w_a and w_a/l_a from the measured corrosion field and 100 realizations of the simulated corrosion fields for the two pipe segments, whereas the empirical CDFs of z_c/l_c , z_c/w_c and w_c/l_c from the measured and simulated corrosion fields for the two pipe segments are depicted in Fig. 5.12. Note that z_a and z_c in Figs. 5.11 and 5.12 are in the unit of mm (i.e. the same as l_a , w_a , l_c and w_c) such that all the ratios are dimensionless. As shown in Figs. 5.11(a), 5.11(b), 5.11(d) and 5.11(e), the CDFs of z_a/l_a and z_a/w_a from the measured fields are slightly on the right side of the corresponding CDFs from the simulated fields, which implies that the measured corrosion field contain more small corrosion pits than the simulated fields. This may be attributed to that the homogenous latent Gaussian field does not fully capture the non-

homogeneity of the actual corrosion field at small length scales. On the other hand, Fig. 5.12 indicates that the characteristics of the corrosion clusters in the simulated fields match well with those in the measured fields. This suggests that the random field model generally captures the characteristics of the corrosion field at larger length scales.

To further compare the measured and simulated corrosion fields, the burst capacities of the two pipe segments at real and simulated corrosion clusters are compared. To this end, the burst capacity of the pipe segment at a given corrosion cluster is computed using the well-known RSTRENG model (Kiefner and Vieth 1989) with the yield strength of the pipe steel assumed to equal 483 MPa (i.e. X70 grade steel). The empirical CDFs of the computed burst capacities corresponding to the clusters on the measured field and 100 realizations of the simulated field for the two pipe segments are compared in Fig. 5.13. Define the corrosion cluster associated with the lowest burst capacity on a pipe segment as the critical cluster. The CDFs of the burst capacities of the critical clusters corresponding to the 100 realizations of the simulated fields are depicted in Fig. 5.14 for both pipe segments, together with the burst capacities of the critical clusters from the measured fields. Figures 5.13 and 5.14 indicate that random field model is capable of generating simulated corrosion clusters corresponding to a range of the burst capacities based on the corrosion measurement data.



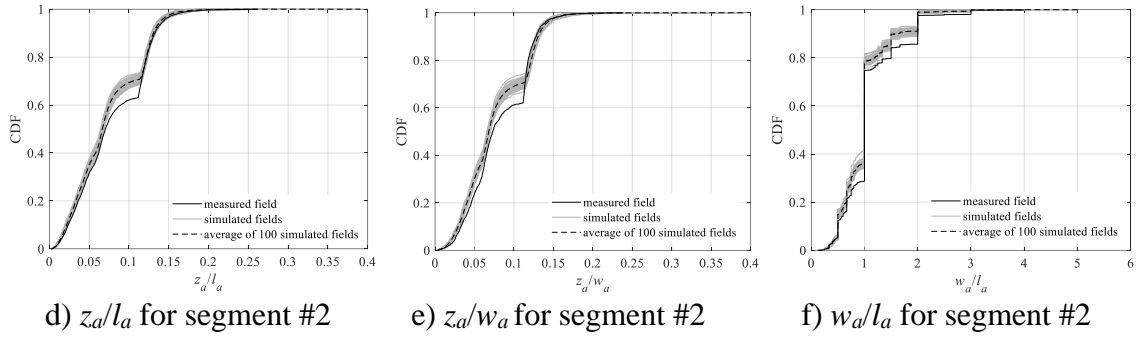


Figure 5.11 Geometric characteristics comparison between the real and simulated corrosion anomalies on pipe segments #1 and #2

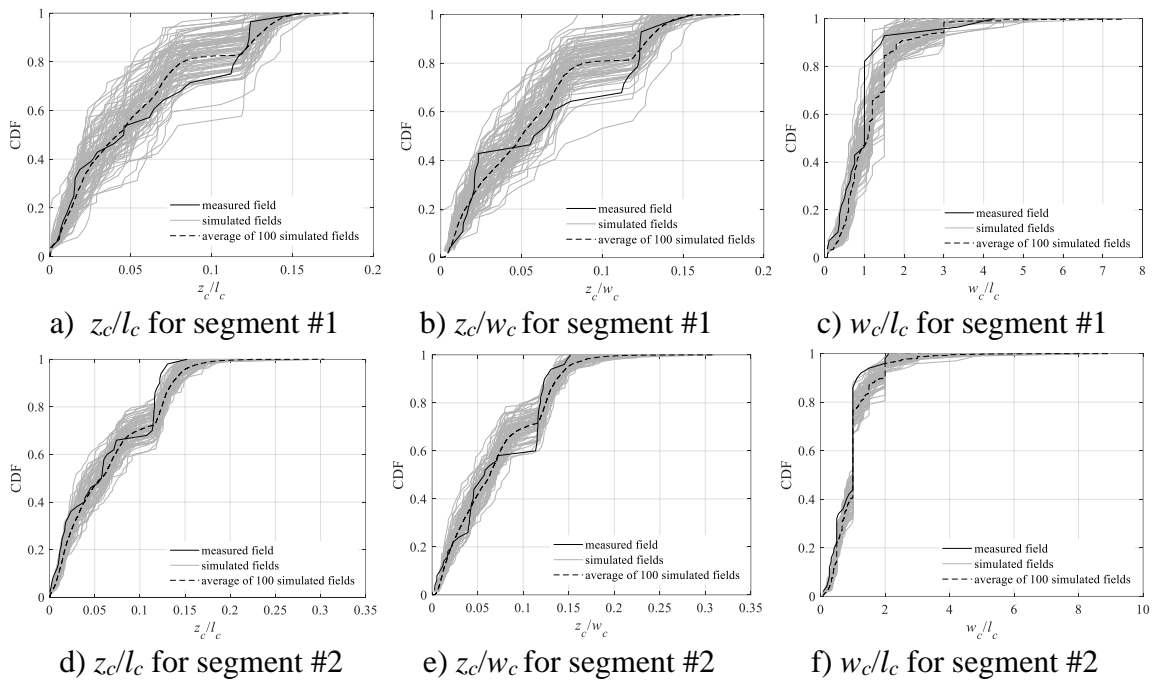


Figure 5.12 Geometric characteristics comparison between the real and simulated corrosion clusters on the pipe segments #1 and #2

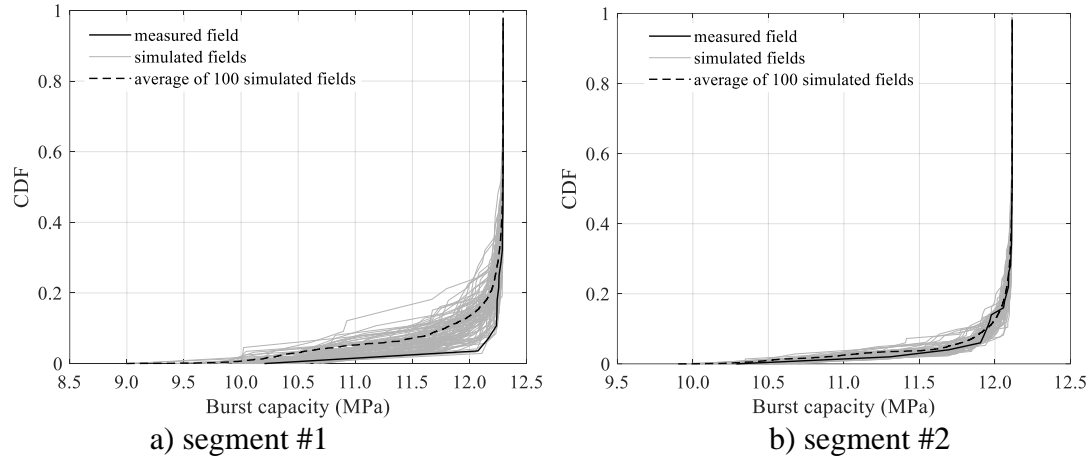


Figure 5.13 Comparison between the empirical CDFs of the burst capacities corresponding to the real and simulated corrosion clusters on pipe segments #1 and #2

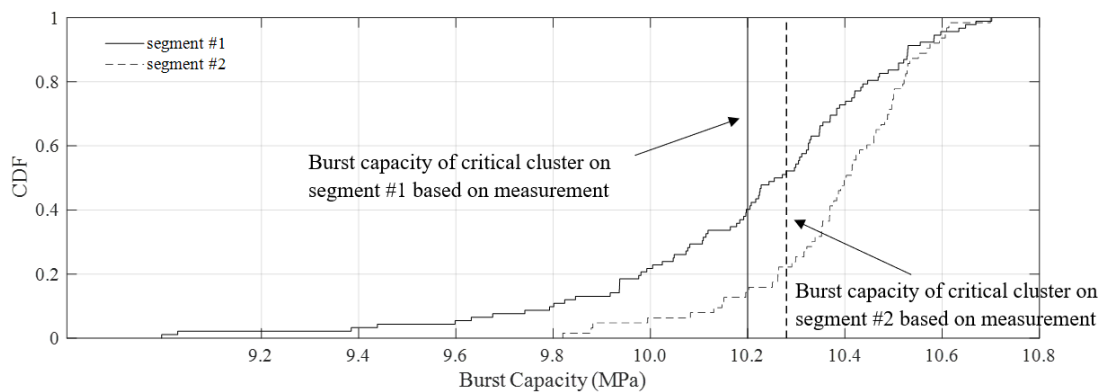


Figure 5.14 Empirical CDF of the burst capacities of critical corrosion clusters corresponding to 100 realizations of simulated corrosion fields for pipe segments #1 and #2

5.4.4 Impact of correlation length

The sensitivity of the simulated corrosion field to the correlation length Δ_c is investigated in this section by considering pipe segment #1. A parametric form of f_c (see Appendix C) for the pipe is developed by fitting the empirical f_c values and employed in the sensitivity analysis. The fitted f_c equation will greatly facilitate the application of the proposed random field model as it eliminates the need to rely on the empirical f_c values to simulate corrosion fields ($H(z)$ and $r_G(\Delta x, \Delta y)$ are both parameterized). Three realizations of Z are

depicted in Fig. 5.15, corresponding to $\Delta_c = 20, 40$ and 60 mm, respectively. Note that the values of m_H and v_H employed in the simulation are the same as those given in Table 5.2 for pipe segment #1. As indicated in Fig. 5.15, the simulated corrosion field contain more individual “pits” for $\Delta_c = 20$ mm, but more corrosion “patches” as Δ_c increases.

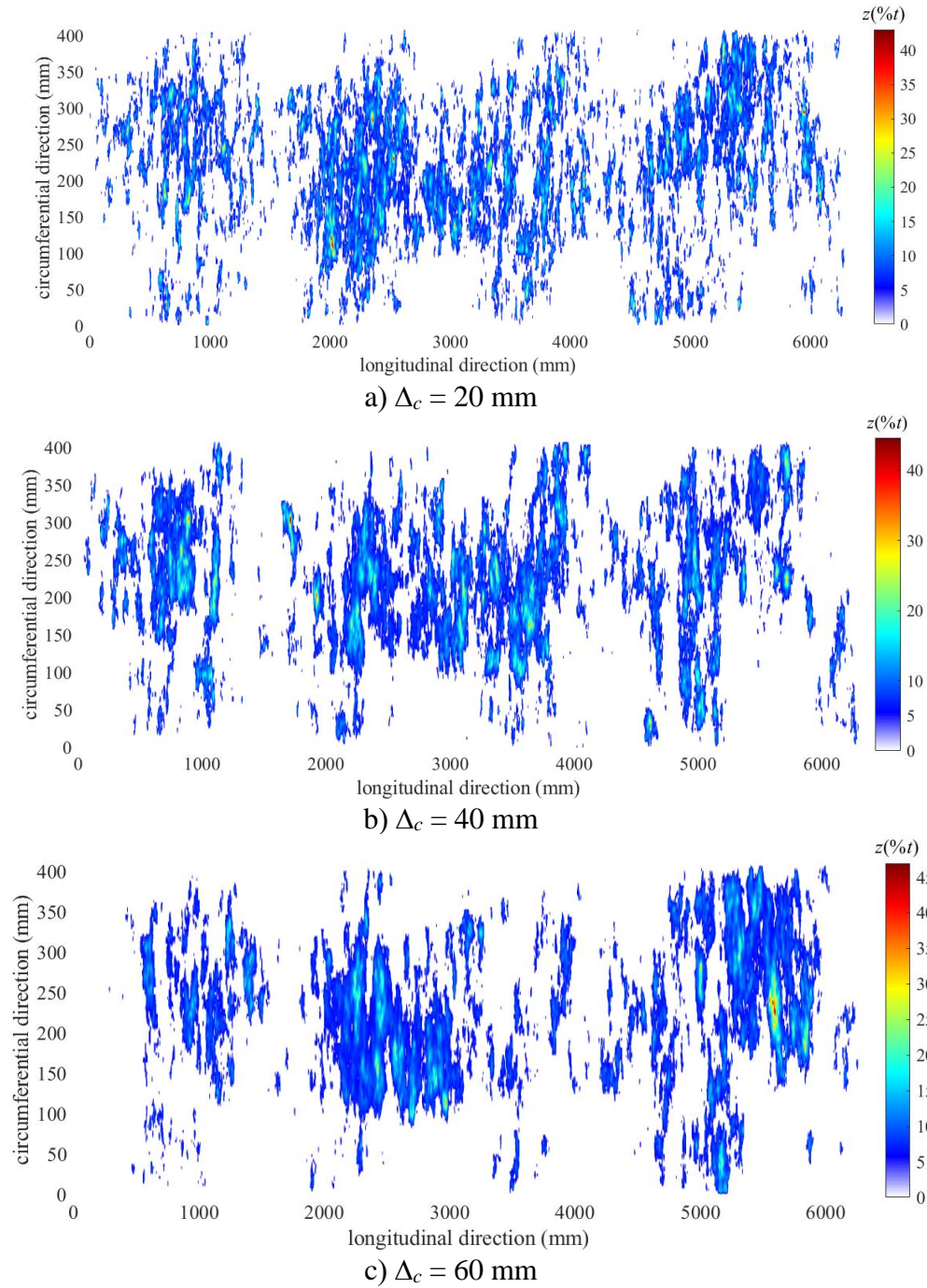


Figure 5.15 Impact of correlation length on the simulated corrosion field for pipe segment #1

5.5 Conclusion

A random field model is developed in this study to simulate the corrosion depth on the external surface of buried oil and gas pipelines based on high-resolution corrosion measurements obtained from pipe segments removed from in-service pipelines. The model employs a latent homogeneous Gaussian random field to characterize the intermingling of corroded and corrosion-free areas on the pipe surface and quantify the nonzero corrosion depth. Similar models have been employed to characterize the spatial distribution of rainfall accumulations within a geographic area. The probability of a given point having nonzero corrosion depth (f_c) is converted to a threshold in the latent Gaussian field. The nonzero corrosion depth is obtained through a transformation between CDF of the corrosion depth and that of the truncated Gaussian distribution. The ML method is proposed to quantify the correlation structure of the latent Gaussian field.

The corrosion measurement data from five pipe segments are used to estimate parameters of the proposed random field model. It is observed that the nonzero corrosion depth can be well fitted by a lognormal distribution with a lower bound of $5\%t$, mean values ranging from 7 to $12\%t$, and COV values ranging from 40 to 70%. It is further observed that an isotropic exponential correlation model is adequate to characterize the correlation structure of the latent Gaussian field, with the correlation length ranging from 20 to 55 mm. Realizations of the proposed model are compared with the corresponding measured corrosion fields in terms of the geometric characteristics of individual corrosion anomalies as well as clusters, and burst capacity of the critical clusters in respective fields. The comparison suggests that the proposed model is able to capture the main characteristics of corrosion on the external surface of naturally-corroded pipelines. Sensitivity analysis of the simulated corrosion field to the correlation length of the latent Gaussian field is also investigated. A parametric expression of f_c as a function of the spatial coordinates is further developed to facilitate the application of the proposed model.

References

Al-Owaisi. S. S., Becker. A. A., Sun. W., Al-Shabibi. A., Maharbi. M. A., Pervez. T., Al-Salmi. H. 2016. An experimental investigation of the effect of defect shape and

- orientation on the burst pressure of pressurised pipes. *Engineering Failure Analysis*, 93: 200 - 213.
- Applus. n.d. Laser scan LPIT (Laser Pipeline Inspection Tool). Available from [https://www.applus.com/es/dam/jcr:aac19a22-9421-4711-b96d-21e99c5438e8/\(N129\)-3D-Laserscan-01282016---NOAM,0.pdf](https://www.applus.com/es/dam/jcr:aac19a22-9421-4711-b96d-21e99c5438e8/(N129)-3D-Laserscan-01282016---NOAM,0.pdf), [accessed 2020-07-18].
- Aryai. V. and Mahmoodian. M. 2017. Spatial temporal reliability analysis of corroding cast iron water pipes. *Engineering Failure Analysis*. 82: 179 - 189.
- AMSE. 2019. Pipeline Transportation Systems for Liquids and Slurries, ASME Code for Pressure Piping, B31. The American Society of Mechanical Engineers, New York, USA.
- Bao. J., Zhang. S., Zhou. W. and Zhang. S. 2018. Evaluation of burst pressure of corroded pipe segments using three-dimensional finite element analysis. In: *Proceedings of the 2018 12th International Pipeline Conference*. Sept. 24 - 28. Calgary, Canada.
- Bell. T. L. 1987. A space-time stochastic model of rainfall for satellite remote-sensing studies. *Journal of Geophysical Research*. 92(8): 9631 - 9643.
- Benjamin. A. C., Freire, J. L. F., Vieira, R. D., Diniz. J. L. C., Andrade, E.Q. 2005. Burst tests on pipeline containing interacting corrosion defects. In: *Proceedings of OMAE2005 24th International Conference on Offshore Mechanics and Arctic Engineering*. June 12 - 17, 2005, Halkidiki, Greece.
- Berrocal. J. V., Raftery. A. E., Gneiting. T. 2008. Probabilistic quantitative precipitation field forecasting using a two-stage spatial model. *The Annual of Applied Statistics*. 2(4): 1170 - 1193.
- Chegeni. B., Jayasuriya. S., Das. S. 2019. Effect of corrosion on thin-walled pipes under combined internal pressure and bending. *Thin-Walled Structures*. 143: 106218.
- Chiodo. M. S. G and Ruggieri. C. 2009. Failure assessments of corroded pipelines with axial defects using stress-based criteria: Numerical studies and verification analyses. *International Journal of Pressure Vessels and Piping*. 86(2-3): 164 - 176.
- CSA. 2019. Oil and gas pipeline systems, CSA standard Z662-19. Mississauga, Canada.
- Garbatov. Y. and Soares. C. G. 2019. Spatial corrosion wastage modeling of steel Plates exposed to marine environments. *Journal of Offshore Mechanics and Arctic Engineering*. 141(3): 031602.
- Ghanem. R. G. and Spanos. P. D. 1991. *Stochastic Finite Elements: A spectral Approach*. Springer-Verlag, New York.

- Htun. M. M., Kawamura. Y. and Ajiki. M. 2013. A study on random field model for representation of geometry of corroded plates and estimation of random properties of their strength. *Journal of the Japan Society of Naval Architects and Ocean Engineers*. 18: 91 - 99.
- Kiefner. J. F. and Vieth. P. H. 1989. A modified criterion for evaluating the remaining strength of corroded pipe. Report Prepared for American Gas Association. PR3 - 805. Columbus, OH, USA.
- Lam. C. and Zhou. W. 2016. Statistical analysis of incidents on onshore gas transmission pipelines based on PHMSA database. *International Journal of Pressure Vessels and Piping*. 145: 29 - 40.
- Lee. G. H., Pouraria. H, Seo. J. K., Paik. J. K. 2015. Burst strength behavior of an aging subsea gas pipeline elbow in different external and internal corrosion-damaged position. *International Journal of Naval Architecture and Ocean Engineering*. 7(3): 435 - 451.
- Li. C., Firouzi. A., Yang. W. 2017. Prediction of pitting corrosion-induced perforation of ductile iron pipes. *Journal of Engineering Mechanics*. 143(8): 04017048.
- Mohd. M. H., Lee. B. J., Cui. Y., Paik. J. K. 2015. Residual strength of corroded subsea pipelines subject to combined internal pressure and bending moment. *Ship and Offshore Structures*. 10(5): 554 - 564.
- Mokhtari. M. and Melchers. R. E. 2019. Next-generation fracture prediction models for pipes with localized corrosion defects. *Engineering Failure Analysis*. 105: 610 - 626.
- Ranji. A. R. 2012. Ultimate strength of corroded steel plates with irregular surfaces under in-plane compression. *Ocean Engineering*. 54: 261 - 269.
- Rasmussen. P. F. 2013. Multisite precipitation generation using a latent autoregressive model. *Water Resources Research*. 49(4): 1845-1857.
- Oliveira. V. D., Wang. B., Slud. E. V. 2018. Spatial modelling of rainfall accumulated over short period. *Journal of Multivariate Analysis*. 166: 129 - 149.
- Panunzio. A. M., Cottreau. R., Puel. G. 2018. Large scale random fields generation using localized Karhunen-Loève expansion. *Advanced Modeling and Simulation in Engineering Science*. 5(20): 1-29.
- Teixeira. A. P. and Soares. C. G. 2008. Ultimate strength of plates with random fields of corrosion. *Structure and Infrastructure Engineering*. 4(5): 363 - 370.
- Vanmarcke. E. 2010. Random fields: analysis and synthesis. World Scientific Publishing Co., Singapore.

- Wang, Q. and Zhou, W. 2019. A new burst pressure model for thin-walled pipe elbows containing metal-loss corrosion defects. *Engineering Structures*. 200: 109720.
- Wilks, D. S. 1998. Multisite generalization of a daily stochastic precipitation generation model. *Journal of Hydrology*. 210(1-4), 178 - 191.
- Yoshida, N. and Yamaguchi, A. 2013. Effect of thickness measurement procedure on stress analysis of pipes with local metal loss. In: *Proceedings of the ASME2013 Pressure vessel and Piping Conference*. Jul. 14 - 18. Paris, France.
- Zhang, S., Yan, J., Shahani, K., Huang, T., Mohammad, A. 2018. A more accurate and precise method for large metal loss corrosion assessment. In: *Proceedings of the IPC2018 12th International Pipeline Conference*. Sept. 24 - 28. Calgary, Canada.
- Zhou, W. and Huang, G. 2012. Model error assessments of burst capacity models for corroded pipelines. *International Journal of Pressure Vessels and Piping*. 99 - 100: 1 - 8.

6 Predictive Accuracy Investigation of Burst Models for Corroded Pipelines Using Finite Element Analysis and Random Field-based Corrosion Simulation Model

6.1 Introduction

Corrosion is one of the major threats to the pipeline safety and integrity (Lam and Zhou 2016). The naturally occurring corrosions are three-dimensional metal loss features of complex morphologies on the external or internal (or both) surfaces of buried pipelines. The corrosion features can be categorized into two types, i.e. individual corrosion anomalies and corrosion clusters consisting of interacting individual anomalies (see Fig. 6.1). The so-called interacting rules (Lamontagne 2002) are used to group closely spaced corrosion anomalies into a corrosion cluster. In the past few decades, various semi-empirical models were proposed to evaluate the burst capacity of corroded pipelines, for example the ASME B31G (ASME 2018), B31G Modified (Kiefner and Vieth 1989), RSTRENG (Kiefner and Vieth 1989), CSA (CSA 2019), DNV (DNV 2017), and PCORRC (Leis and Stephens 1997; Stephens and Leis 2000) models.

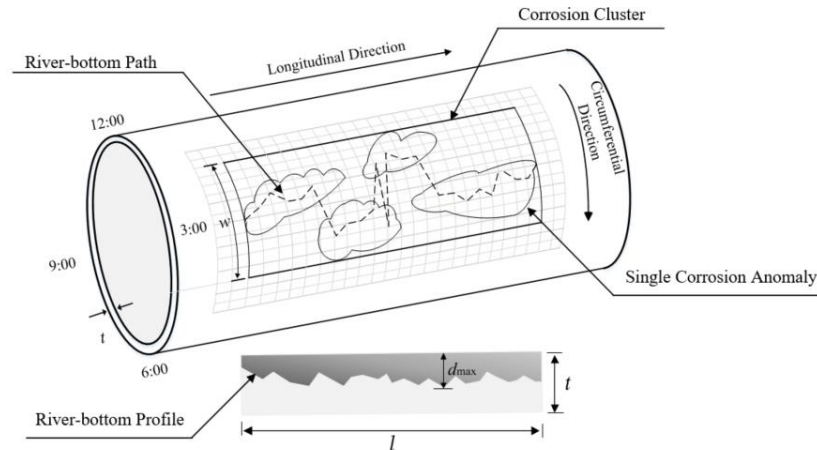


Figure 6.1 Illustration of corrosion anomaly, corrosion cluster, river-bottom path and river-bottom profile

The semi-empirical models can be classified into two levels (ASME 2018), namely Level 1 and Level 2 models. Level 1 models employ the maximum corrosion depth (d_{max}) and length (l) (Fig. 6.1) to evaluate the burst capacity of a corrosion feature; Level 2 models incorporate greater details of the corrosion geometry than Level 1 models, such as the so-

called river bottom profile employed in the CSA and RSTRENG models. As shown in Fig. 6.1, a river bottom path is defined by connecting the maximum corrosion depths at different longitudinal coordinates within a corrosion feature, and the river bottom profile is generated by projecting the river bottom path onto a longitudinal plane perpendicular to the wall thickness direction. Zhou and Huang (2012a) investigated the predictive accuracy of several well-known Level 1 and 2 models by comparing model-predicted burst capacities with the corresponding observed values from a series of full-scale tests of pipe specimens containing naturally-occurring corrosion features. They reported that Level 2 models always achieve higher predictive accuracies than Level 1 models. However, high costs of obtaining naturally corroded full-scale pipe specimens for burst tests greatly limit the number of specimens that can be afforded in a research program.

Alternatively, the finite element analysis (FEA) has proven to be a viable tool to accurately evaluate the burst capacities of corroded pipelines. Bao et al. (2018), Chouchaoui (1993), Cronin (2000) and Pimentel et al. (2020) validated the accuracy of high-fidelity FEA models to evaluate the full-scale burst tests of the specimens containing naturally occurring corrosion features. Bao and Zhou (2020) carried out FEA to investigate the predictive accuracy of different semi-empirical models in terms of different classifications (POF 2016) of the naturally occurring corrosion anomalies. Mokhtari and Melchers (2019) proposed the 3D PCORRC model and validated the accuracy of 3D PCORRC by comparing the model-predicted and FEA-evaluated burst capacities of artificially introduced corrosion anomalies with complex corrosion morphologies.

A random field-based corrosion model is described in Chapter 5 to simulate naturally-occurring corrosions on the external surfaces of buried pipelines. The random field model employs a latent homogeneous Gaussian random field and spatially varying thresholds associated with the latent Gaussian field to capture the intermingling nature of the corroded and corrosion-free areas on the external surface of a pipeline. By combining FEA with the random field-based corrosion model, full-scale burst tests of pipe specimens containing simulated corrosion features resembling naturally-occurring corrosions, referred to as synthetic corrosion features, can be carried out numerically, which leads to significant cost

reduction and great flexibility in selecting test parameters (e.g. geometry of corrosion features).

In this chapter, the predictive accuracy of the modified RSTRENG model (RSTRENG-M) as proposed in Chapter 4 is investigated based on FEA of 120 synthetic corrosion features generated by using the random field-based corrosion model. For comparison, five existing Level 2 semi-empirical models, namely DNV, RSTRENG, CSA, Psqr (Zhang et al. 2018) and CPS (Cronin and Pick 2002), are also applied to the 120 corrosion features. The rest of the chapter is organized as follows: Section 6.2 introduces the above mentioned six Level 2 burst capacity evaluation models; Section 6.3 briefly describes the parameter selection for the random field-based corrosion model and the identification of corrosion clusters from the simulated corroded surfaces, along with the FEA simulation of the synthetic corrosion clusters, and the predictive accuracies of the six burst capacity models and the impact of geometries of corrosion features on the model accuracies are discussed based on the FEA results in Section 6.4, followed by the conclusion in Section 6.5.

6.2 Semi-empirical burst capacity models for corroded pipelines

All the six burst capacity models considered in this study, except for the CPS model, are rooted in the well-known NG-18 equation (Maxey et al. 1972), which expresses the burst capacity of a corroded pipe in terms of the burst capacity of the pristine pipe, projected corrosion area on a longitudinal plane perpendicular to the wall thickness and Folias (bulging) factor. Among the six models, the RSTRENG, CSA, CPS and DNV models calculate the burst capacities by utilizing the river-bottom profile. Although the river-bottom profile is a reasonable representation of the 3D corrosion profile, its two-dimensional nature means that it may miss other important corrosion morphologies. In this regard, the RSTRENG-M model described in Chapter 4 considers the profile of a corrosion feature along each circumferential plane. Zhang et al. (2018) proposed to use multiple plausible profiles, as opposed to a single river bottom profile, to evaluate the burst capacity of a corrosion feature. The details of RSTRENG, RSTRENG-M and CSA models have

been presented in Chapters 2 and 4. The DNV, CPS and Psqr models are briefly described in the following sections.

6.2.1 DNV model

Since all the corrosion features included in this study are corrosion clusters consisting of multiple interacting single corrosion anomalies, the DNV model for interacting anomalies (DNV 2017) is considered in this study. In this model, each of the corrosion anomalies included in a cluster is simplified as a cubic metal loss (Fig. 6.2), which has the same length, width and maximum depth as the corresponding anomaly. To apply the DNV model, one needs to project all the boxes onto a longitudinal plane to generate the projected profile (river-bottom profiles of the boxes enclosing the anomalies). As depicted in Fig. 6.2, if the projections of some corrosion anomalies overlap on the longitudinal plane, they should be treated as a single anomaly, with length equal to the total length and depth equal to the maximum depth of all the overlapped anomalies.

Assume a corrosion cluster contains m corrosion anomalies. Equations (6.1a) and (6.1b) are used to calculate the burst capacity of each single anomaly.

$$P_{b-DNV}^i = \frac{2t\sigma_u}{D-t} \frac{1 - \frac{d_{max,i}}{t}}{1 - \frac{d_{max,i}}{tM_i}} \quad i = 1, 2, 3, \dots, m \quad (6.1a)$$

$$M_i = \sqrt{1 + 0.31 \frac{l_i^2}{Dt}} \quad (6.1b)$$

where P_{b-DNV}^i is the burst capacity of corrosion anomaly i ; $d_{max,i}$ and l_i are the maximum corrosion depth and length of the i^{th} corrosion anomaly; D is the outside diameter of the pipeline; t is the pipe wall thickness, and σ_u is the material ultimate tensile strength.

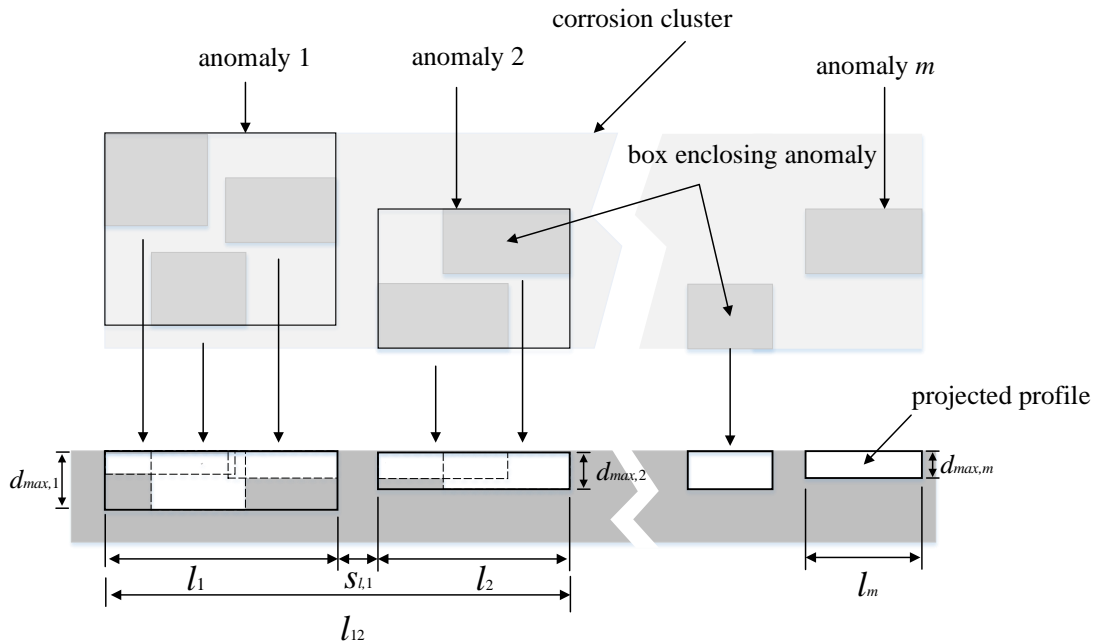


Figure 6.2 Illustration of the DNV model and combined corrosion anomaly

Moreover, the reduction of the burst capacity is considered in the DNV model that adjacent corrosion anomalies should be combined into groups. For example, the anomalies 1 and 2 in Fig. 6.2 are grouped to form a combined corrosion anomaly. The length l_{12} and the effective depth $d_{eff,12}$ of the combined anomaly are

$$l_{12} = l_1 + l_2 + s_{l,1} \quad (6.2)$$

$$d_{eff,12} = \frac{d_{max,1}l_1 + d_{max,2}l_2}{l_{12}} \quad (6.3)$$

where $s_{l,1}$ is the longitudinal spacing between anomalies 1 and 2. Then, the burst capacity of combined anomaly, P_{b-DNV}^{12} , is calculated by replacing l_i and $d_{max,i}$ in Eqs. (6.1a) and (6.1b) with l_{12} and $d_{eff,12}$, respectively. Similarly, the burst capacities of all the combined corrosion anomalies should be calculated. To this end, the burst capacity for the corrosion cluster predicted by DNV model, P_{b-DNV} , is defined as the minimum of the capacities of all the single and combined anomalies.

Note that Eq. (6.1a) is derived from the burst capacity model for the single isolated corrosion anomalies (DNV 2017), in which the corrosion anomalies are treated as the cubic metal losses with length l_i and maximum depth d_i . Hence, the DNV model simplifies the

naturally occurring corrosion features to single or combined corrosion anomalies of cubic shapes.

6.2.2 CPS model

The CPS model considers the burst capacity of a pipe segment containing a corrosion feature, P_{b-CPS} , to be bounded by the burst capacity of a plain (corrosion free) pipe, P_{PP} , as the upper limit and the burst capacity of a pipe containing an axially-oriented infinitely-long groove having the same depth as the maximum depth of the corrosion feature, P_{LG} , as the lower limit. The burst capacity of the feature is then calculated from P_{PP} and P_{LG} with an interpolation parameter g ($0 \leq g \leq 1$) depending on the pipe geometry and corrosion morphology.

$$P_{b-CPS} = P_{LG} + g(P_{PP} - P_{LG}) \quad (6.4)$$

$$P_{PP} = \left(\frac{2+\sqrt{3}}{4\sqrt{3}} \right)^{n+1} \frac{4t}{D} \sigma_u \quad (6.5)$$

$$P_{LG} = \frac{\sigma_{crit}(t-d_{max})}{R_i \sqrt{\frac{3}{4}}} \exp\left(-\sqrt{\frac{3}{4}} \varepsilon_{crit}\right) \quad (6.6)$$

In this study, P_{PP} is evaluated using Eq. (6.5), which is proposed by Zhu and Leis (2012) and has been shown to be highly accurate (Zhou and Huang 2012b). In Eqs. (6.4)-(6.6), d_{max} is the maximum depth of a corrosion feature, and $R_i = D/2 - t$ is the pipe internal radius. n is the strain hardening exponent and can be estimated from an empirical equation proposed by Zhu and Leis (2012) as $n = 0.224(\sigma_u/\sigma_y - 1)^{0.604}$ with σ_y being the steel yield strength. $\sigma_{crit} = \sigma_u e^n$ and $\varepsilon_{crit} = n$ are the true stress and true strain at the point of necking in a tensile coupon test, where e is the base of natural logarithm. The calculation of g involves an iterative procedure and is described in the following.

As shown in Fig. 6.3, the river bottom profile of a corrosion feature is measured at M locations with the measurement resolution equal to Δx along the longitudinal direction. Let x_i and x_{eva} denote the longitudinal coordinates of the i^{th} measurement point and an evaluation point, respectively. Let d_i and d_{eva} denote the corrosion depths of the i^{th} measurement point and the evaluation point on the river bottom profile.

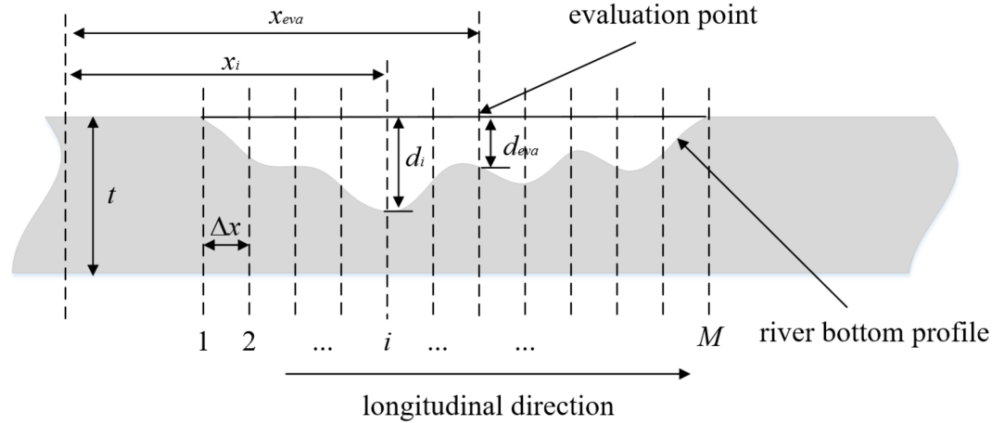


Figure 6.3 Illustration of the CPS model and the determination of the parameter g

Define the parameter g for the evaluation point in Fig. 6.3 as

$$g = \frac{\text{sumWDD}}{\text{MaxWDD}} \quad (6.7)$$

where,

$$\text{sumWDD} = \sum_{i=1}^M \left\{ \text{sech} \left[\frac{x_{eva} - x_i}{\sqrt{D(t - d_{max})}} \right] \left[\left(1 - \frac{d_i}{t} \right) - \left(1 - \frac{d_{eva}}{t} \right) \right] \Delta x \right\} \quad (6.8)$$

The MaxWDD corresponds to the weighted difference of a plain pipe such that d_i ($i = 1, 2, \dots, M$) in Eq. (6.8) is equal to zero.

$$\text{MaxWDD} = \sum_{i=1}^M \left\{ \text{sech} \left[\frac{x_{eva} - x_i}{\sqrt{D(t - d_{max})}} \right] \left[\left(1 - \frac{0}{t} \right) - \left(1 - \frac{d_{eva}}{t} \right) \right] \Delta x \right\} \quad (6.9)$$

In Eqs. (6.8) and (6.9), sech is the hyperbolic secant function. The burst capacity of the corrosion feature should be evaluated at each of the M measurement points on the river bottom points by inserting Eq. (6.7) into Eq. (6.4). The burst capacity of the corrosion feature is defined as the minimum burst capacity of that evaluated at the M measurement points.

6.2.3 Psqr model

While the RSTRENG, RSTRENG-M, DNV and CPS models employ one corrosion profile, e.g. the river-bottom profile, the Psqr model presented in Fig. 6.4 considers multiple (e.g. 500) plausible corrosion profiles depending on the corrosion depths and the circumferential distances between longitudinal neighbouring points. The burst capacity for each of the plausible profiles is calculated by using the effective area method (Eqs. (4.1) and (4.2) in

Chapter 4). The burst capacity of the corrosion feature is defined as a low percentile value (i.e. 5th percentile) of the burst capacities corresponding to all the plausible profiles.

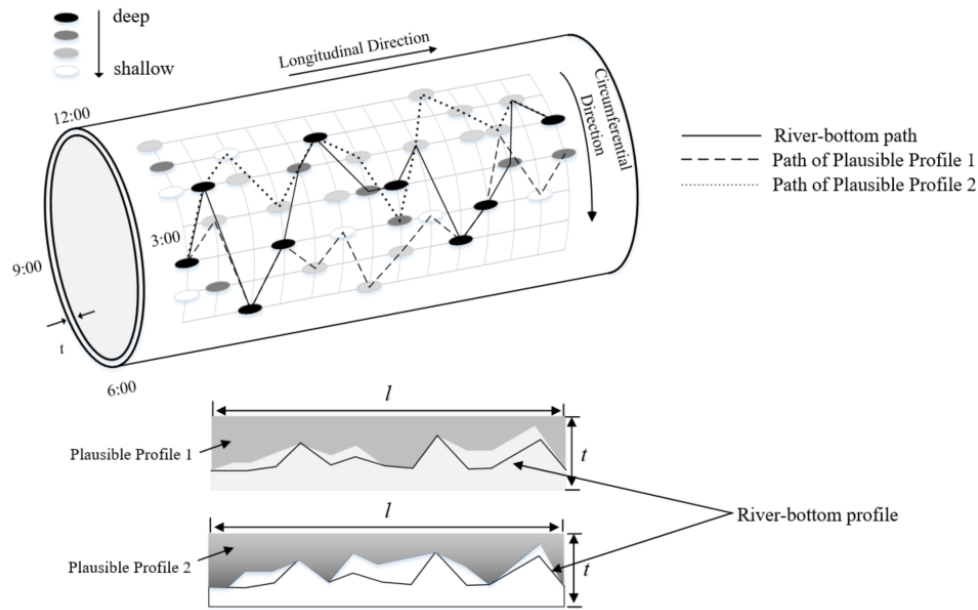


Figure 6.4 Illustration of the plausible profiles and Psqr model

6.3 Generation and FEA of synthetic corrosion features

6.3.1 Generation of synthetic corrosion features

The random field-based corrosion model presented in Chapter 5 is employed to simulate the external surface of a naturally corroded underground pipeline. As shown in Eq. (5.6), the model has 4 parameters, i.e. the mean (m_H) and coefficient of variation (COV) (v_H) of the shifted lognormal distribution, correlation length (Δ_c) and a spatially dependent function ($f_c(x, y)$), which is a function of the longitudinal and circumferential (arclength) coordinates (x, y) of the external pipe surface. The values of m_H , v_H , and Δ_c are estimated from five naturally corroded pipe segments removed from in-service pipelines. Table 6.1 summarizes the ranges of these model parameters presented in Chapter 5. The $f_c(x, y)$ is fitted by a two-dimensional Fourier sine series (Eq. C.1) with the coefficients c_{ij} provided in Table C.1.

Table 6.1 The ranges of the model parameters for the random field corrosion model presented in Chapter 5

Parameter	m_H (% t)	v_H (%)	Δ_c (mm)
Range	7.5 - 12.5	40 - 70	20 - 55

In this study, an example pipeline with the outside diameter and wall thickness assumed to be 508 and 6.35 mm, respectively, is considered. Three different steel grades (i.e. X52, X60 and X70) are considered in the analyses with the corresponding material properties (i.e. yield strength, ultimate tensile strengths and Young's modulus E) listed in Table 6.2. The correlation length of the latent Gaussian field for the random field corrosion model is selected, somewhat arbitrarily, to be 35, 55 and 25 mm for the X52 X60 and X70 steels, respectively. The length (L) and width (W) of the random corrosion field are selected to be 6400 mm and 400 mm, respectively. The values of m_H and v_H corresponding to each realization are randomly selected within the corresponding ranges of m_H and v_H indicated in Table 6.1. The random field is realized on a grid of 2×2 mm (i.e. grid sizes along both the longitudinal and circumferential directions are 2 mm). A total of 120 corrosion surfaces are generated in this study with 40 cases for the X52 pipe, 40 cases for the X60 pipe and 40 cases for the X70 pipe. The maximum corrosion depths (z_{max}) of the 120 simulated surfaces are between 30 and 70% t . The widely used B31.4 (ASME 2019) (see the description in Chapter 5) is applied to the 120 corrosion surfaces to combine the corrosion anomalies in close proximity into clusters. Figure 6.5 illustrates one of the realized random fields, which consists of 1052 corrosion anomalies and 51 corrosion clusters.

The deepest corrosion cluster on each simulated surface is collected and employed in this study. Hence, a total of 120 corrosion clusters are selected for the subsequent burst capacity evaluation with the ranges of the length (l), width (w) and depth summarized in Table 6.2. Figure 6.6 depicts the lengths and widths of all 120 clusters.

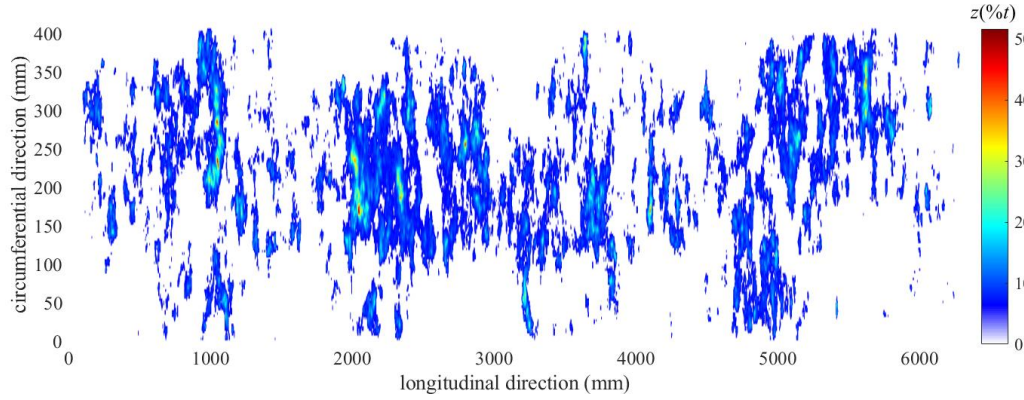


Figure 6.5 A realization of the random corrosion field with $m_H = 8.6\%t$, $v_H = 39.8\%$ and $\Delta_c = 35\text{ mm}$

Table 6.2 Summary of the material and geometrical properties of the corrosion clusters simulated in this study

Steel grade	Material property		Geometric property					Number of clusters	
	σ_y (MPa)	σ_u (MPa)	E (GPa)	D (mm)	t (mm)	l (mm)	w (mm)		d_{max} (%t)
X52	359	455	207	508	6.35	64-584	48-406	30-70	40
X60	415	520				88-492	72-400		
X70	483	565				42-492	24-404		

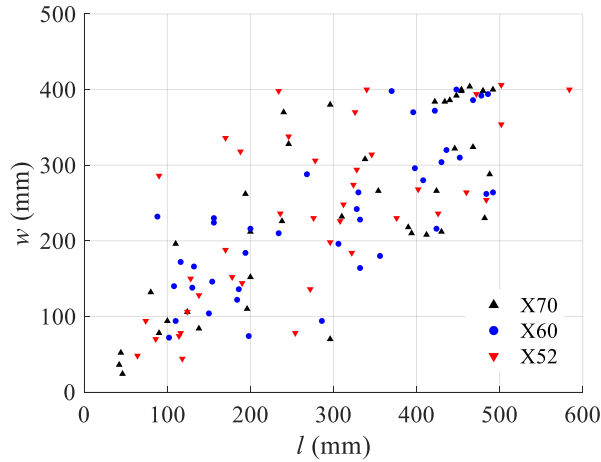
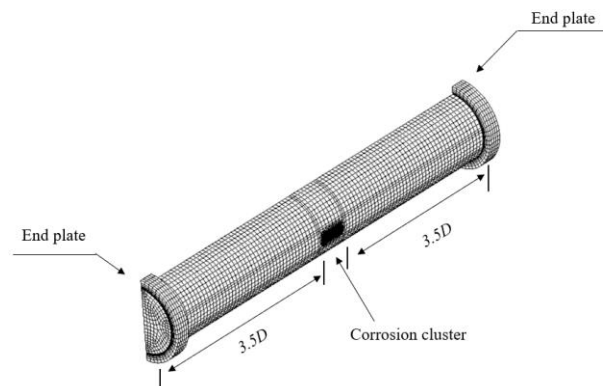


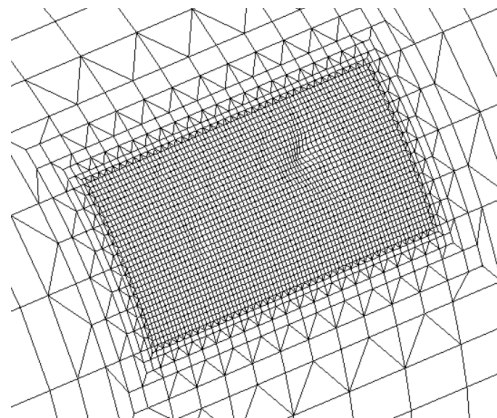
Figure 6.6 Lengths and widths of the 120 corrosion clusters on the pipe segments made by X52, X60 and X70 steels

6.3.2 FEA of synthetic corrosion clusters

Pipe segments containing synthetic corrosion clusters are analyzed by using the commercial FEA software ANSYS (version 16.1). The configuration of the FEA model and the mesh generation have been described in Chapter 3. Based on the convergence analysis, the element size within the corrosion clusters is selected at 2×2 mm and a coarser mesh of 32×32 mm is used to generate the corrosion free region. Four layers of elements are placed along the wall thickness direction to avoid the shear locking. Figure 6.7 depicts one of the FEA models containing the synthetic corrosion cluster as an example. The FEA model consists of around 80,000 nodes and 85,000 elements.



a) configuration of the FEA model



b) corrosion cluster and transition elements

Figure 6.7 Configuration of the FEA model containing a synthetic corrosion cluster

The true stress (σ) - true strain (ε) relationship input in FEA is fitted by the commonly used power-law that

$$\begin{cases} \sigma = E\varepsilon & \sigma < \sigma_y \\ \sigma = K\varepsilon^n & \sigma \geq \sigma_y \end{cases} \quad (6.10)$$

where the strength coefficient $K = \frac{\sigma_u e^n}{n^n}$ and $n = 0.224(\sigma_u/\sigma_y - 1)^{0.604}$ (Zhu and Leis 2012) are calculated based on the σ_y and σ_u values for different steel grades in Table 6.2. By tracking the maximum nodal von Mises stress within the corrosion cluster, the failure criterion described in Chapter 3 is used to predict the burst capacity of the FEA model. The FEA model validation is carried out by comparing the FEA-predicted burst capacities of the critical corrosion clusters of the 14 pipe segments with the capacities observed in the full-scale burst pressure tests, which has been reported in Chapter 3.

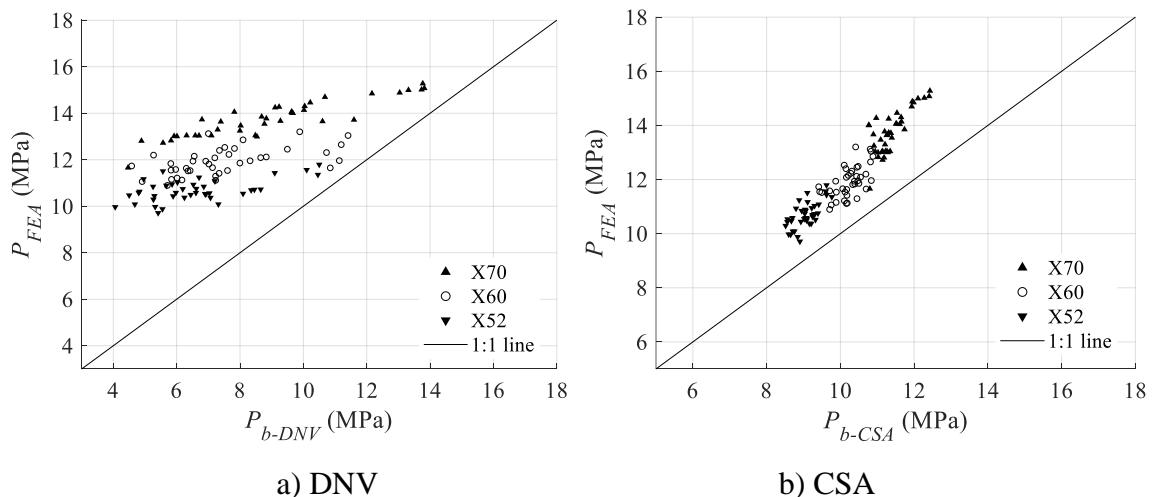
6.4 Investigation of the predictive accuracy based on FEA results

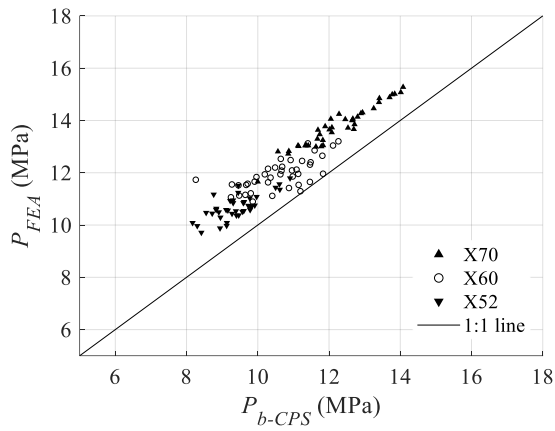
Given the high accuracy of the FEA predictions, the predictive accuracies of all the six semi-empirical models are investigated and compared based on the FEA predicted burst capacities (P_{FEA}). Define P_{b-RST} , P_{b-RSM} , P_{b-Psq} and P_{b-CSA} as the burst capacities predicted by RSTRENG, RSTRENG-M, Psqr and CSA models, respectively. The predicted burst capacities of the 120 corrosion clusters using the six models are depicted in Fig. 6.8, and the mean and COV of the FEA-to-predicted ratios are listed in Table 6.3. In general, all the models are on average conservative compared to the FEA predictions. From Fig. 6.8 and Table 6.3, it is observed that the DNV model is the most inaccurate among the six Level 2 models, i.e. the mean and COV of the FEA-to-predicted ratios for DNV model are 1.67 and 21.6%, respectively. The DNV model is more conservative for larger and deeper corrosion clusters, i.e. the FEA-over-model prediction ratios increases as P_{FEA} decreases. Since the evaluation equations for the DNV model (Eq. (6.1)) is derived from the burst capacity of a single cubic corrosion anomaly, it implies that it is inadequate to simplify irregularly-shaped naturally-occurring corrosion clusters to single or combined corrosion anomalies of cubic shapes as described in section 6.2.1.

The accuracy of the CPS model is also relatively poor as reflected from the mean and COV values of the corresponding FEA-to-model prediction ratios given in Table 6.3. The

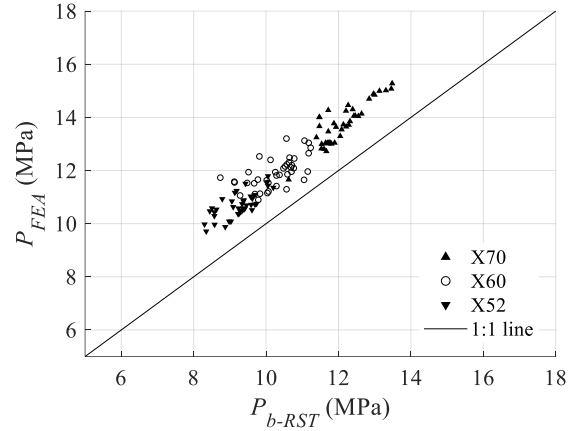
accuracy of the CPS model for the 40 clusters on the X60 steel pipe is lower than that for the clusters on the X52 and X70 pipes: the COV of the FEA-to-predicted ratios of the clusters on X60 pipe is 7.5%, higher than the 5.2% and 3.4% of the clusters on X52 and X70 pipes. It can be attributed to that the correlation length used to simulate the corrosion surfaces on the X60 pipe is greater than those used on the X52 and X70 pipes. A longer correlation length leads to a corrosion surface containing more corrosion “patches” of higher morphological complexity, as opposed to the corrosion “pits” generated when correlation length is short. Similarly, the improvements of RSTRENG-M and Psqr over the RSTRENG model in terms of the predictive accuracy is observed to be most significant for the clusters on the X60 pipe. This suggests that the river-bottom profile may not be adequate to capture the geometric characteristics of corrosion clusters of complex morphology. In this case, it is important to take into account the geometric information along the circumferential direction of the corrosion cluster.

The mean and COV of FEA-to-CSA predicted ratio (1.18 and 4.7%) are generally similar to the RSTRENG model (1.15 and 4.8%). The RSTRENG-M and Psqr models are observed to be the two most accurate models; RSTRENG-M is less biased (smaller mean value of FEA-to-model prediction ratios) and more accurate than the RSTRENG and CSA models for the clusters on all the three pipe materials.

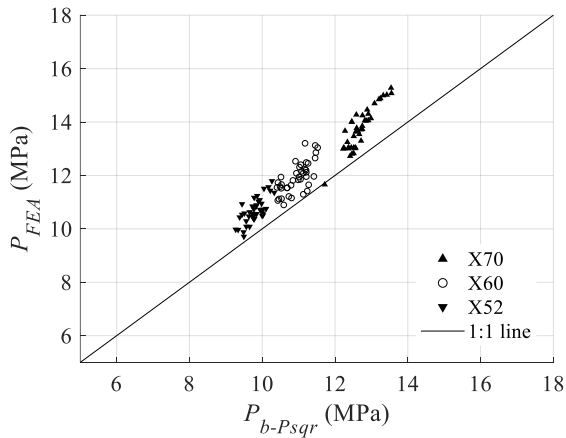




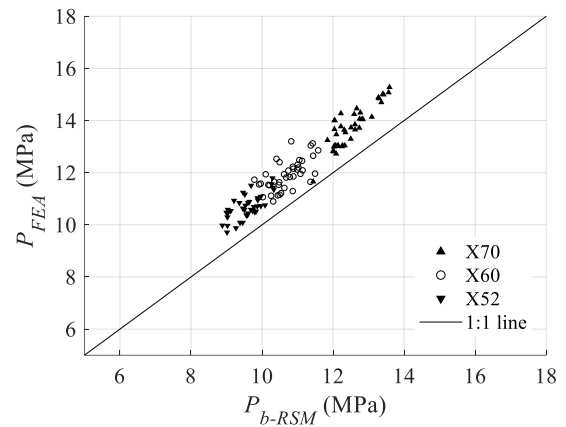
c) CPS



d) RSTRENG



e) Psqr



f) RSTRENG-M

Figure 6.8 Comparison between the FEA and predicted burst capacities in terms of different semi-empirical models based on the 120 synthetic corrosion clusters

Table 6.3 Summary of the basic statistics of the FEA-to-predicted ratios of corrosion clusters on the pipe segments made by different materials

Model		Steel Grade			
		X52	X60	X70	All
P_{FEA}/P_{b-DNV}	Mean	1.70	1.66	1.64	1.67
	COV (%)	20.6	20.2	24.3	21.6
P_{FEA}/P_{b-CSA}	Mean	1.18	1.16	1.20	1.18
	COV (%)	3.9	4.7	4.6	4.7
P_{FEA}/P_{b-CPS}	Mean	1.14	1.13	1.13	1.13
	COV (%)	5.2	7.5	3.4	5.6
P_{FEA}/P_{b-RST}	Mean	1.16	1.16	1.14	1.15
	COV (%)	4.4	6.1	3.3	4.8
P_{FEA}/P_{b-Psq}	Mean	1.09	1.09	1.08	1.09
	COV (%)	3.3	3.7	3.6	3.5
P_{FEA}/P_{b-RSM}	Mean	1.12	1.11	1.10	1.11
	COV (%)	3.7	4.5	3.2	3.8

The impact of the length l and maximum depth d_{max} of the corrosion clusters on the predictive accuracies of the six burst capacity models are investigated as well. Figure 6.9 depicts the mean and COV of the FEA-to-predicted burst capacity ratios for different corrosion depth ranges with the bracketed numbers denoting the number of corrosion clusters used for the calculations. Except for the CPS and DNV models, all the models tend to be less conservative when the maximum corrosion depth increases from 30 to 70% t , while CPS and DNV model are more conservative when they are applied to deeper corrosion clusters. The predictions by all the models have greater variability, i.e. associated with higher COV values of the FEA-to-model prediction ratios, for corrosion clusters with larger d_{max} . The CPS model is the most accurate for the relatively shallow corrosion clusters (i.e. $d_{max} < 40\%t$), which may be attributed to the high accuracy of the burst capacity equation for the pristine pipe (Eq.(6.5)) such that the CPS model performs the best for shallow corrosion clusters as the impact of the corrosion on the burst capacity is relatively small. The accuracy of the CPS model decreases noticeably when the corrosion cluster becomes deeper.

The predictive accuracy of the DNV model deteriorates markedly when applied to the deeper corrosion anomalies, e.g. the mean (COV) of FEA-to-model prediction ratios for

the DNV model increases from 1.3 (13.5%) to 2.1 (23.6%) as the maximum corrosion depth increases from the range of 30 - 40% t to the range of 60 - 70% t . The RSTRENG-M and Psqr models are more accurate than RSTRENG for the deep corrosion clusters as can be clearly observed from Fig. 6.9.

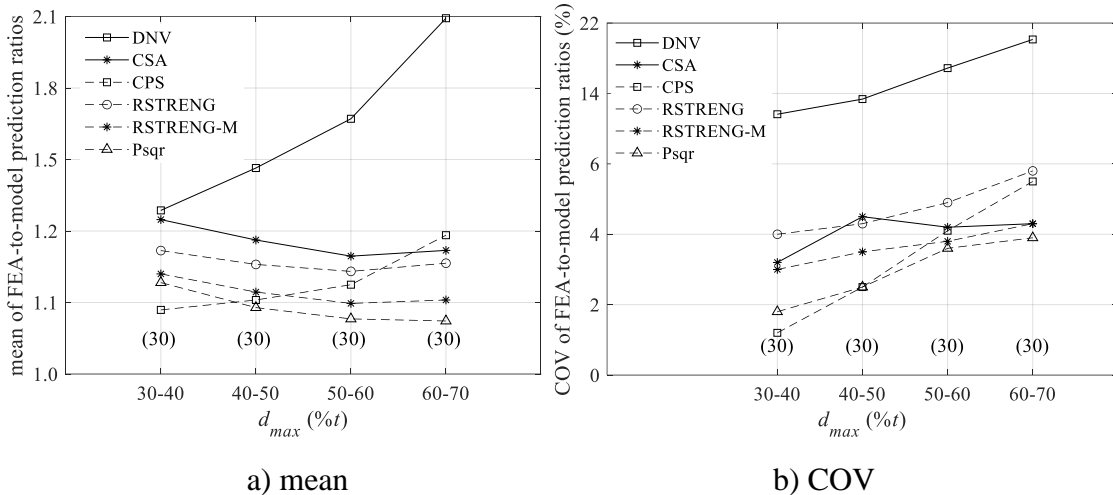


Figure 6.9 Impact of the maximum depths of corrosion clusters on the model accuracy

The effect of the length of the corrosion cluster on the predictive accuracy of the models is presented in Fig. 6.10. The DNV models results in highly conservative predictions for long corrosion clusters (e.g. the average FEA-to-model prediction ratio is higher than 1.52 when the corrosion cluster is longer than 200 mm). The RSTRENG model tends to be more conservative as the length of the cluster increases, while the predictions of CPS and Psqr models are shown to be less conservative as the length increases. The mean value of FEA-to-RSTRENG-M prediction ratios is more or less the same regardless of the corrosion cluster length. No clear trend is observed between the corrosion cluster length and COV values for all the models. On the other hand, the predictive accuracies (mean and COV) of the six models are independent of the corrosion length for lengths greater than 300 mm.

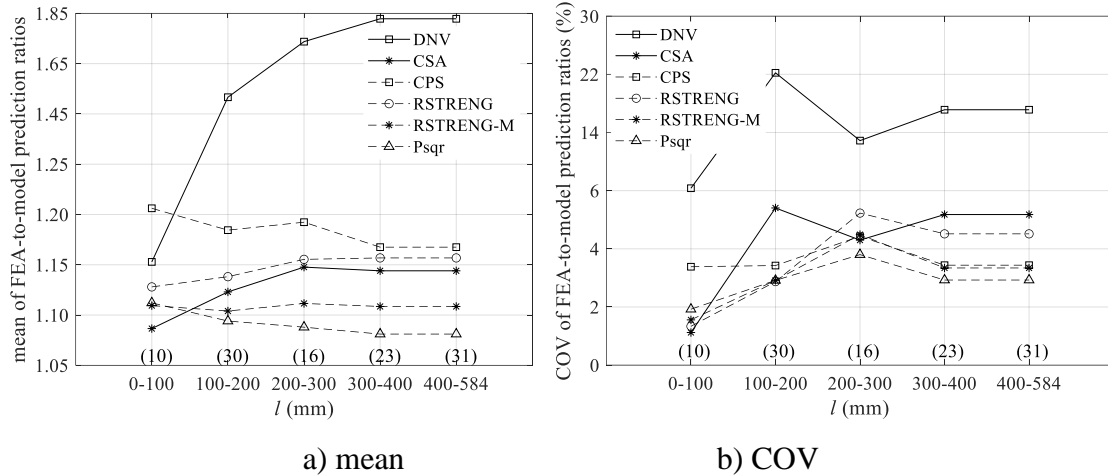


Figure 6.10 Impact of the lengths of corrosion clusters on the model accuracy

6.5 Conclusions

In this chapter, the external corrosion surfaces of buried pipelines are simulated using a random field-based corrosion model. The corrosion anomalies on simulated corrosion surfaces are combined into 120 synthetic corrosion clusters, and the burst capacities of the corrosion clusters are evaluated by using six Level 2 burst capacities models, as well as three-dimensional elasto-plastic FEA. The six burst capacity models are the DNV, CSA, CPS, RSTRENG, RSTRENG-M and Psqr models.

With the FEA-predicted burst capacities considered as the benchmark, the accuracies of the six semi-empirical burst capacity models are evaluated based on the mean and COV of the FEA-to-model predicted burst capacity ratios. It is observed that the predictive accuracy of the DNV model is the poorest among the six models. The RSTRENG-M and Psqr models are the most accurate in that the mean of FEA-to-model prediction ratios equal 1.11 and 1.09, respectively, with the corresponding COV equal to 3.8 and 3.5%, respectively.

The impact of maximum corrosion depths and lengths of corrosion clusters on the model accuracies is also investigated. The results suggest that the RSTRENG, RSTRENG-M, CSA and Psqr models tend to be less conservative with an increasing maximum corrosion

depth, whereas the CPS and DNV models are more conservative for deeper corrosion clusters. The predictive accuracies of all the models decrease (higher COV values) when they are applied to the deeper corrosion clusters. There is no clear dependence of the COVs of FEA-to-predicted ratios on the cluster lengths for all the six models based on 120 FEA results of synthetical corrosion clusters. The mean and COV values tend to be uncorrelated with the corrosion length when the corrosion clusters are longer than 300 mm.

References

- ASME. 2018. Manual for determining the remaining strength of corroded pipelines. Supplement to ASME B31 Code for Pressure Piping. ASME B31G - 2018. New York, USA.
- AMSE. 2019. Pipeline transportation systems for liquids and slurries, ASME code for pressure piping, B31. The American Society of Mechanical Engineers, New York, USA.
- Bao. J., Zhang. S., Zhou. W. and Zhang. S. 2018. Evaluation of burst pressure of corroded pipe segments using three-dimensional finite element analysis. In: Proceedings of the 2018 International Pipeline Conference. Sept. 24 - 28. Calgary, Canada.
- Bao. J. and Zhou. W. 2020. Influence of the corrosion anomaly class on predictive accuracy of burst capacity models for corroded pipelines. *International Journal of Geosynthetics and Ground Engineering*, 6(45).
- Chouchaoui. B. 1993. Evaluating the remaining strength of corroded pipelines. Ph.D. thesis. Waterloo, Canada: Department of Mechanical Engineering, University of Waterloo.
- Cronin. D. S. 2000. Assessment of corrosion defects in pipelines. Ph.D. thesis. Waterloo, Canada: Department of Mechanical Engineering, University of Waterloo.
- Cronin. D. S and Pick. R. J. 2002. Prediction of the failure pressure for complex corrosion defects. *International Journal of Pressure Vessels and Piping*. 79: 279 - 287.
- CSA. 2019. Oil and gas pipeline systems, CSA Standard Z662 -19. Mississauga, Canada.
- DNV. 2017. Corroded Pipelines. DNV-RP-F101 code. Det Norske Veritas. Oslo, Norway.
- Kiefner. J. F. and Vieth. P. H. 1989. A modified criterion for evaluating the remaining strength of corroded pipe. Report Prepared for American Gas Association. PR3 - 805. Columbus, OH, USA.

- Lam. C. and Zhou. W. 2016. Statistical analyses of incidents on onshore gas transmission pipelines based on PHMSA database. *International Journal of Pressure Vessels and Piping*. 145: 29 - 40.
- Lamontagne. M. 2002. Interaction rules - an integral factor. In: *Proceedings of the NACE International Conference Corrosion*. Apr. 7 - 11. Denver, USA.
- Leis. B. N. and Stephens. D. R. 1997. An alternative approach to assess the integrity of corroded line pipe part I: current status; part II: alternative criterion. In: *Proceedings of the 7th International Offshore and Polar Engineering Conference*, May 25 - 30. Honolulu, USA.
- Maxey. W. A., Kiefner. J. F., Eiber. R. J. and Duffy. A. R. 1972. Ductile fracture initiation, propagation, and arrest in cylindrical vessels. Fracture toughness. In: *Proceedings of the 1971 National Symposium on Fracture Mechanics, Part II, ASTM STP 514*. American Society of Testing and Materials: 70 - 81.
- Mokhtari. M. and Melchers. R. E. 2019. Next generation fracture prediction models for pipes with localized corrosion defects. *Engineering Failure Analysis*. 105: 610 - 626.
- Panunzio. A. M., Cottureau. R., Puel. G. 2018. Large scale random fields generation using localized Karhunen-Loève expansion. *Advanced Modeling and Simulation in Engineering Science*. 5(20): 1 - 29.
- Pimentel. J. T., Ferreira. A. D. M., Motta. R. S., Cabral. M. A. F. S., Afonso. S. M. B., Willmersdorf. R. B. et al. 2020. New procedure of automatic modelling of pipelines with realistic shaped corrosion defects. *Engineering Structures*. 221: 111030.
- Pipeline Operators Forum. 2016. Specifications and requirements for in-line inspection of pipelines. Version 2016.
- Stephens. D. R. and Leis. B. N. 2000. Development of an alternative failure criterion for residual strength of corrosion defects in moderate-to high-toughness pipe. In: *Proceedings of the 2000 International Pipeline Conference*. Oct. 1 - 5. Calgary, Canada.
- Zhang. S., Yan. J., Kariyawasam. S., Huang. T., Al-Amin. M. 2018. A more accurate and precise method for large metal loss corrosion assessment. In: *Proceedings of the 2018 International Pipeline Conference. IPC2018*. Sept. 24 - 28. Calgary, Canada.
- Zhou. W. and Huang. G. 2012a. Model error assessments of burst capacity models for corroded pipelines. *International Journal of Pressure Vessels and Piping*. 99 - 100: 1 - 8.

Zhou. W. and Huang. G. 2012b. Model error assessment of burst capacity models for defect-free pipes. In: Proceedings of the IPC2012 International Pipeline Conference. Sept. 24 - 28. Calgary, Canada.

Zhu. X. K. and Leis. B. N. 2012. Evaluation of burst pressure prediction models for line pipes. International Journal of Pressure Vessels and Piping. 89: 85 - 97.

7 Summary, Conclusions and Recommendations for Future Study

7.1 General

This research employs the finite element analysis (FEA) and random field analysis to address five issues regarding the fitness-for-service (FFS) assessment of naturally corroded pipelines. The conclusions drawn from this thesis and recommendations for the future study are given as follows.

7.2 Influence of depth threshold and interaction rule on the burst capacity evaluation of naturally corroded pipelines by using FEA and RSTRENG model

In Chapter 2, both the RSTRENG model and FEA are employed to evaluate the burst capacities of corroded pipelines. The impact of the depth threshold on the predicted burst capacity is investigated by FEA of modified corrosion surfaces of 14 naturally corroded pipe segments that corruptions shallower than different threshold values are removed. The results indicate that applying a corrosion threshold depth of 10% wall thickness to corroded pipe surface causes an insignificant increase of the predicted burst capacity. Hence, 10% t is recommended to identify corrosion anomalies.

The effectiveness of the DNV, 6WT, 3WT, B31.4 and CW interaction rules are investigated by comparing the RSTRENG-predicted and FEA-predicted burst capacities of 54 groups of critical corrosion clusters to that of 54 significant corrosion areas on 14 pipe specimens. The burst capacities of the critical corrosion clusters generated by the CW, B31.4, and 3WT rules can be 5% higher than the burst capacity of the corresponding corrosion area, while the burst capacities of the critical clusters based on the DNV and 6WT rules are always within 3% difference compared to the capacities of the corresponding corrosion surface. The large interacting limits in DNV rule result in large-sized corrosion clusters such that the generated corrosion clusters are time-consuming to analyze. The 6WT corrosion clusters are smaller than the DNV clusters in size, but they are always observed to cover the critical corrosion areas and having the similar burst

capacities to the DNV corrosion clusters. Thus, the 6WT rule is considered as the optimal to generate the corrosion cluster in the practical FFS assessment.

7.3 Impact of corrosion anomaly class on the predictive accuracy of burst capacity models for corroded pipelines

In Chapter 3, the predictive accuracies of B31G, B31G-M, PCORRC, PCORRC-M, Shell92, CSA and RSTRENG models are investigated in terms of the classification of corrosion anomalies. A total of 897 corrosion anomalies are collected from the external surfaces of 16 pipe segments removed from in-service pipelines. Based on the POF classification rule of corrosion anomalies, the 897 corrosion anomalies consist of 46 pin holes, 39 circumferential slotting, 16 circumferential grooving, 52 axial slotting, 42 axial grooving, 601 pitting and 101 general corrosion anomalies. The burst capacities of all the corrosion anomalies are predicted by using the 3D elasto-plastic FEA, which are treated as the benchmark to compare the predictive accuracies of the seven semi-empirical models based on the mean and COV of FEA-to-model predicted ratio of each model.

All the seven models have the similar predictive accuracies when they are applied to the non-general corrosion anomalies, while the models requiring the detailed corrosion profiles lead to more accurate predictions compared to the ones calculating the burst capacity based on the simple inputs for the general corrosion anomalies. The PCORRC model is recommended for non-general classes of anomalies considering its least unbiasedness, and the CSA model is recommended for anomalies in the general class due mainly to its smallest COV of FEA-to-model predicted ratios among all the seven models.

7.4 A modified RSTRENG model to predict the burst capacity for corroded pipelines

Chapter 4 presents a RSTRENG-M model to evaluate the burst capacity of corroded pipelines. As opposed to the river bottom profile employed in the RSTRENG model, the

RSTRENG-M model considers riverbed profile connecting the representative corrosion depths on a series of circumferential profiles. The representative depth at a given circumferential profile of the corrosion feature is the average of the maximum and average depths of the portion of the profile deeper than 10% of the pipe wall thickness. Given the riverbed profile, the effective area method as employed in RSTRENG is applied to evaluate the burst capacity of the corrosion feature. Based on 60 full scale burst test results of corroded pipe segments containing both the naturally- occurring and artificially induced corrosion features collected from 3 publications, the RSTRENG-M model is more accurate than the RSTRENG model and has the similar performance to the Psqr model. Moreover, the RSTRENG-M model is computationally more efficient than the Psqr model.

The RSTRENG-M model also leads to the moderately conservative estimates and lower variability when applied to the simulated ILI reported corrosion features, in which the irregular-shaped corrosion anomalies are replaced by the semi-ellipsoidal metal losses having the same length, width and maximum corrosion depth to the naturally occurring corrosion anomalies. A simple empirical equation between the maximum corrosion depth and the representative corrosion depth on the circumferential profile is fitted based on 30,763 circumferential profiles generated from a total of 667 corrosion clusters on 16 naturally corroded pipe specimens to facilitate the application of the RSTRENG-M model in the context of the ILI reported corrosion profiles.

7.5 A random field model to simulate the naturally corroded external surface of buried pipelines

Chapter 5 proposes a random field model to simulate the external surface of naturally corroded buried pipelines. A spatially correlated latent Gaussian random field and a coordinate dependent function are employed to capture the intermittent characteristics of the corroded and non-corroded areas on the corrosion surfaces. The coordinate dependent function is then converted to a threshold function of the latent Gaussian field. The nonzero corrosion depth is obtained through a transformation between marginal CDF of the

corrosion depth and that of the truncated Gaussian distribution, and the values of the latent field less than the threshold function are set to zero. The marginal distribution of the nonzero corrosion depth and the correlation structures of the latent Gaussian field are determined from five naturally corroded pipe segments measured by the high-resolution laser scanners. A shifted lognormal distribution with a lower bound of $5\%t$ has been observed to fit the distribution of the nonzero corrosion depths on the external surfaces very well. It is further observed that an isotropic exponential correlation model is adequate to characterize the correlation structure of the latent Gaussian field, with the correlation length ranging from 20 to 55 mm. The realized random field is capable of capturing the geometric and mechanical properties of the corrosion anomalies and clusters on the simulated surface.

Combining with FEA, this random field-based corrosion model can greatly facilitate the burst capacity evaluation of naturally corrosion features and reduce the cost for obtaining the naturally corroded pipe segments.

7.6 Predictive accuracy investigation of burst models for corroded pipelines based on FEA of synthetic corrosion features generated by the random field-based corrosion model

In Chapter 6, the burst capacities of 120 synthetical corrosion features generated by the random field-based corrosion model are evaluated by FEA. The maximum corrosion depths of the 120 synthetical corrosion features are between 30 to $70\%t$ with lengths between 42 to 584 mm. Considering the high accuracy of the FEA predictions, the predictive accuracies of DNV, CSA, CPS, RSTRENG, RSTRENG-M and Psqr models are compared based on the mean and COV of the FEA-to-model predicted burst capacity ratios.

The DNV model is the most inaccurate among the six models that the predictive accuracy deteriorates significantly for deep corrosion features. The mean of FEA-to-DNV predicted

ratio increases from 1.3 to 2.1, and COV increases from 13.5 to 23.6%, as the maximum depth range of corrosion features increases from 30 - 40% t to 60 - 70% t .

The RSTRENG-M and Psqr models are the most accurate in that the means of FEA-to-model prediction ratios equal 1.11 and 1.09, respectively, with the corresponding COVs equal to 3.8 and 3.5%, respectively. Both the RSTRENG-M and Psqr models tend to be slightly less accurate for the corrosion features of greater maximum corrosion depths. The CPS model is the most accurate for the shallow corrosion features, while the prediction accuracy decreases for deep corrosion features.

The impact of corrosion feature lengths on the predictive accuracies is also investigated based on the 120 synthetic corrosion features. For long corrosion features, CPS and Psqr are less conservative, while DNV, RSTRENG and CSA are shown to be more conservative. No dependence of the COV of FEA-to-model prediction ratios on the corrosion feature lengths is observed for all the six models.

7.7 Research significance and novelty

Corrosion is a main threat to the integrity of underground transmission pipelines. To deal with the pipeline corrosion, pipeline operators usually carry out the FFS assessment to demonstrate the integrity of pipelines for the continued service. The FFS assessment generally involves the corrosion anomaly identification, corrosion cluster generation and the burst capacity prediction. The existing researches investigate the FFS assessment by using the pipe segments containing the artificially induced corrosion features. However, the geometric differences between the artificial corrosion features and the naturally occurring corrosion features indicate that the artificial corrosion features are not suitable for the investigation of the FFS assessment of corroded pipelines. This thesis helps to improve the FFS assessment by employing the FEA and random field-based corrosion simulation model of naturally corroded pipe segments. The findings of this thesis will directly benefit the pipeline industry with the corrosion anomaly identification, corrosion cluster generation and the improvement of the predictive accuracy of the burst capacity of corroded pipelines. The random field-based corrosion simulation model can be combined

with FEA to generate and analyze the corrosion features in a large quantity to facilitate the proposal and validation of the new semi-empirical models.

7.8 Recommendations for future study

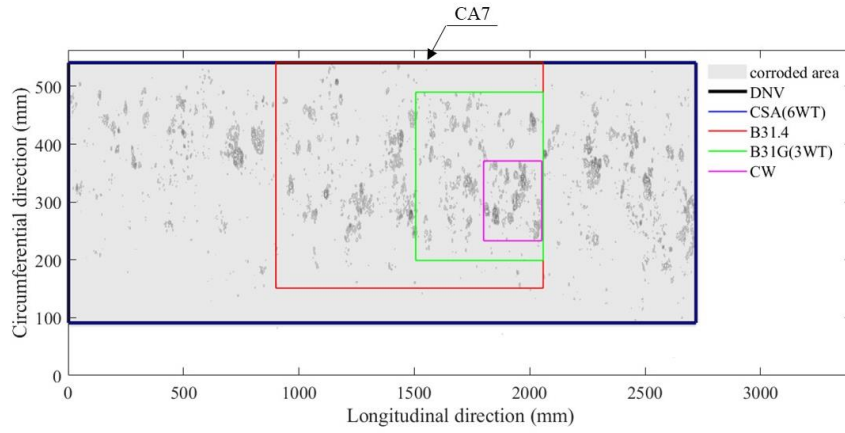
The recommendations for future study are summarized as follows:

1. The prediction accuracy of FEA should be improved if possible. It is observed from the results in this study, as well as some published papers, that the failure criterion might be depending on the pipeline grade steel and the detailed corrosion geometry. It will be a good topic if the FEA simulated burst processes can be compared to a vast amount of full scale burst tests of pipe segments made by different grade steels not only on the burst pressure, but also the strain (e.g. Green-Lagrangian strain) and displacement field.
2. It is worthwhile to employ a new random field-based corrosion model to consider the non-homogeneity of the corroded surface. The correlation structure of the small pits on the scanned surface is supposed to be different from the large sized general corrosions. Besides, the new model may focus only on the critical corrosion clusters, instead of the entire scan surface to improve the simulation efficiency.
3. The RSTRENG-M model has proven to be more accurate than the RSTRENG based on a large amount of full scale burst tests and FEA of pipe segments with the detailed corrosion profiles, whereas the application of RSTRENG-M to the ILI data is only investigated with 14 simulated ILI clusters. The RSTRENG-M model should be validated by more realistic ILI data.
4. The efficiency of the FEA model generation and calculation is still very low when the corrosion clusters are large in size. The computational cost can be reduced by sub modeling technique that the FEA model of the full-sized naturally corroded pipe segment can be divided into two sub models for simultaneous simulation. One sub model simulates the full-sized defect free pipe with coarse mesh density and provides the boundary conditions

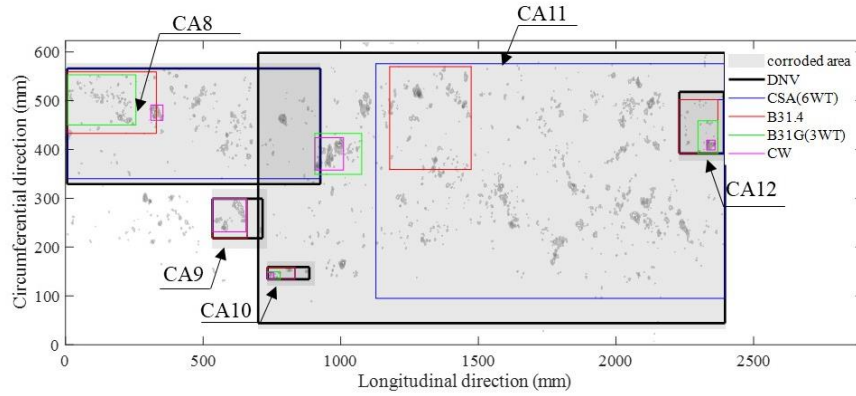
to the other sub model. The second sub model only simulates the corrosion cluster with high mesh density.

Appendices

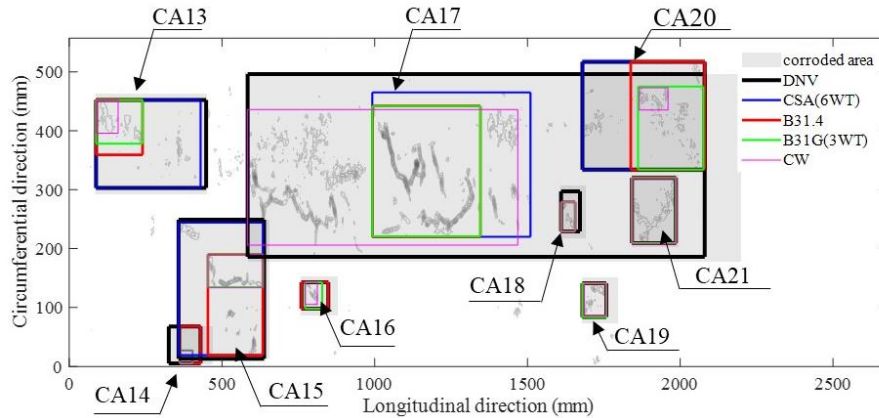
Appendix A Corroded areas and critical corrosion clusters on specimens #2 - #14



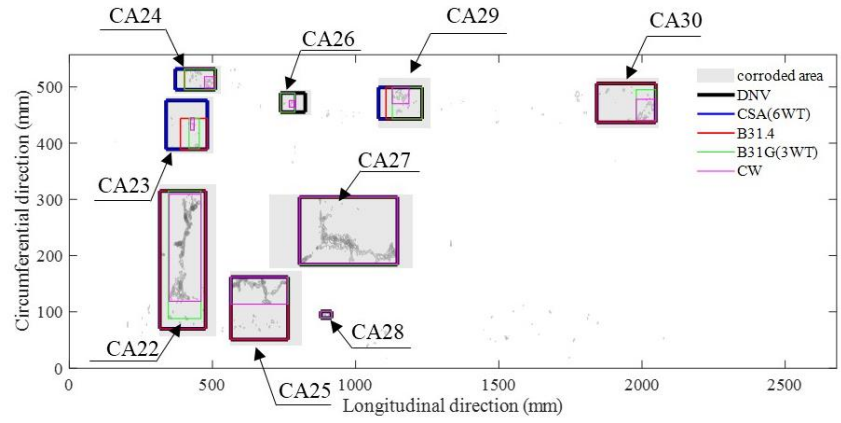
a) Specimen 16-2



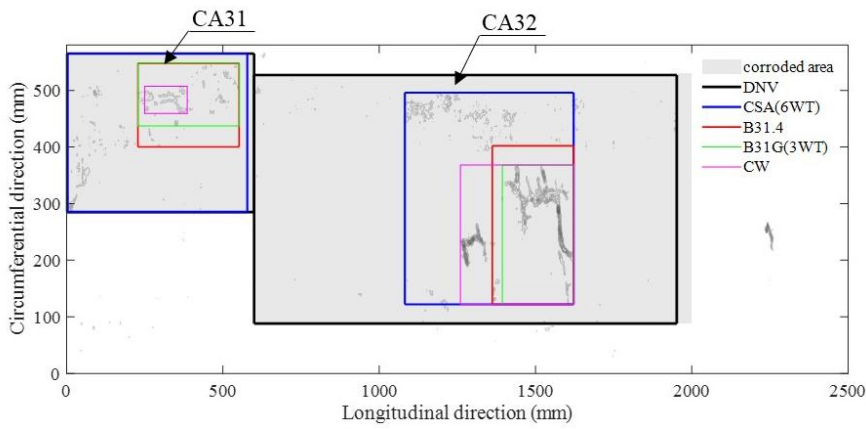
b) specimen 16-3



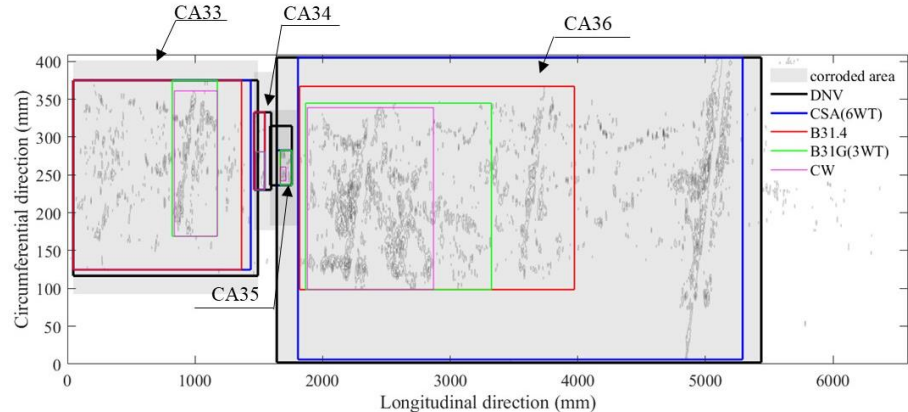
c) specimen 16-5



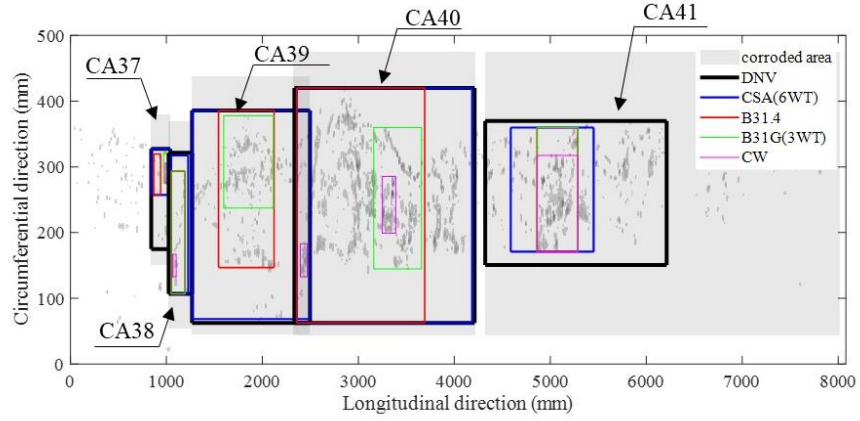
d) specimen 16-6



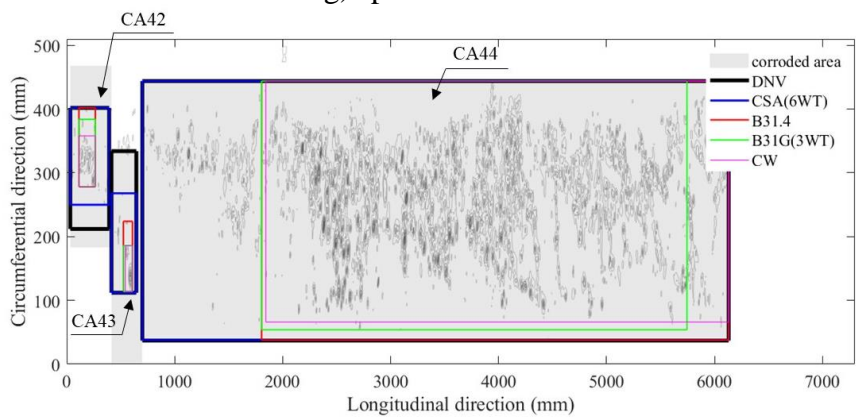
e) specimen 16-7



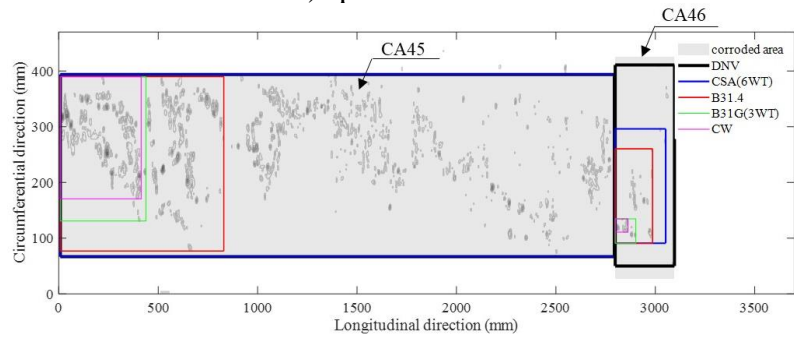
f) specimen 24-1



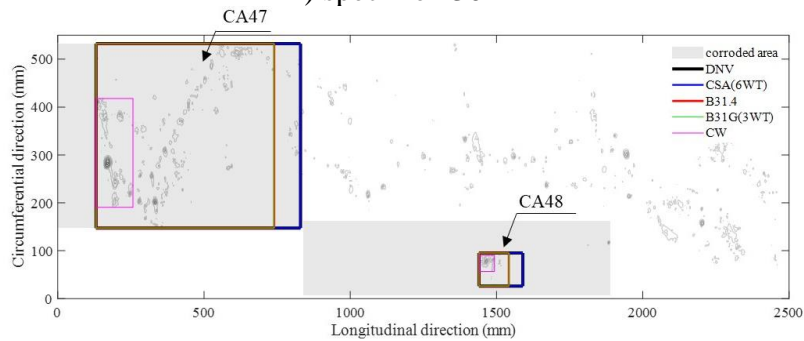
g) specimen 24-2



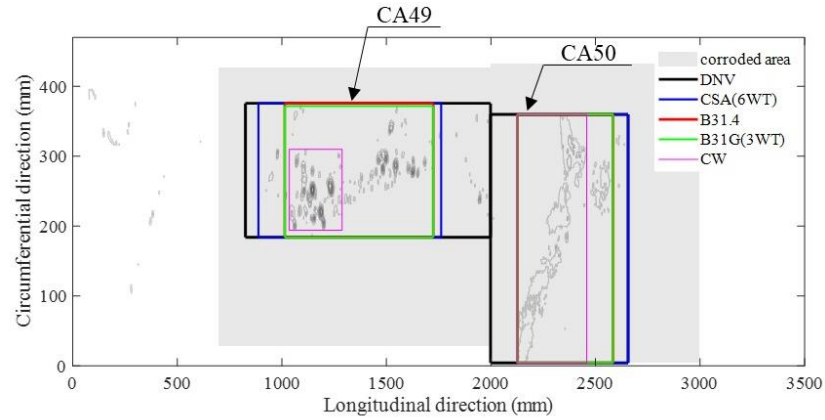
h) specimen 30-1



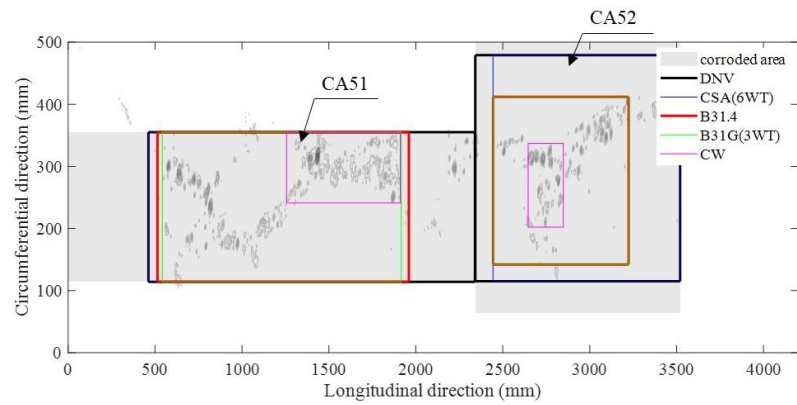
i) specimen 30-2



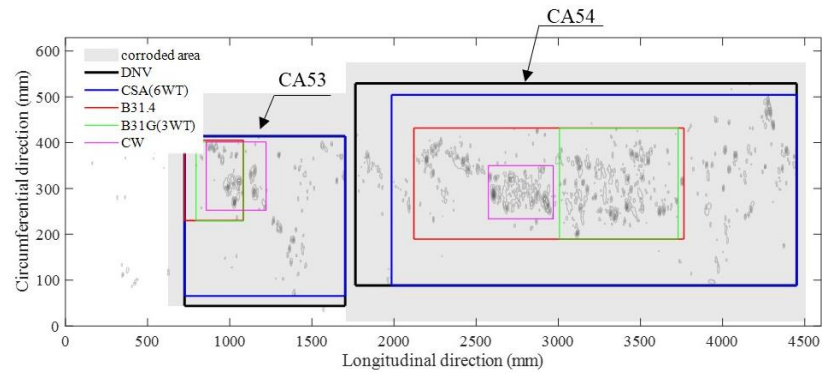
j) specimen 30-3



k) specimen 30-4



l) specimen 30-5



m) specimen 30-6

Figure A.1 Corroded areas on specimens #2 - #14 in Table 2.2 and critical corrosion clusters identified based on different interaction rules

Appendix B Derivation of Eq. (5.4)

If a pair of grid points belong to scenario 1), i.e. $z_1 = z_2 = 0$, its likelihood is the probability of $G_1 \leq g_{0,1}$ and $G_2 \leq g_{0,2}$, where G_1 and G_2 are the standard Gaussian variates with a correlation coefficient of r_G . It follows that the likelihood of $z_1 = z_2 = 0$ is,

$$\Phi_2(g_{0,1}, g_{0,2}, r_G) \quad (\text{B.1})$$

If a pair of grid points belong to scenario 2), i.e. $z_1 = 0$ and $z_2 > 0$, its likelihood is equivalent to that of $G_1 \leq g_{0,1}$ and $G_2 = g_2$, where $g_2 = \Phi^{-1}(F_Z(z_2))$, which can be expressed using the conditional probability as,

$$\Phi\left(\frac{g_{0,1} - r_G g_2}{\sqrt{1 - (r_G)^2}}\right) \phi(g_2) = \Phi\left(\frac{g_{0,1} - r_G \Phi^{-1}(F_Z(z_2))}{\sqrt{1 - (r_G)^2}}\right) \phi\left(\Phi^{-1}(F_Z(z_2))\right) \quad (\text{B.2})$$

The likelihood for scenario 3), i.e. $z_1 > 0$ and $z_2 = 0$, can be similarly derived as

$$\Phi\left(\frac{g_{0,2} - r_G g_1}{\sqrt{1 - (r_G)^2}}\right) \phi(g_1) = \Phi\left(\frac{g_{0,2} - r_G \Phi^{-1}(F_Z(z_1))}{\sqrt{1 - (r_G)^2}}\right) \phi\left(\Phi^{-1}(F_Z(z_1))\right) \quad (\text{B.3})$$

where $g_1 = \Phi^{-1}(F_Z(z_1))$. Finally, if a pair of grid points belong to scenario 4), i.e. $z_1 > 0$ and $z_2 > 0$, its likelihood is equivalent to that of $G_1 = g_1$ and $G_2 = g_2$, which is given by

$$\phi_2(\Phi^{-1}(F_Z(z_1)), \Phi^{-1}(F_Z(z_2)), r_G) \quad (\text{B.4})$$

By considering n_1 , n_2 , n_3 and n_4 pair of points in scenarios 1), 2), 3) and 4) respectively, their corresponding likelihood functions, i.e. Eqs. 5.4(a) – 5.4(d), can be readily obtained from Eqs. (B.1) - (B.4), respectively.

Appendix C Parametric expression of f_c for pipe segment #1

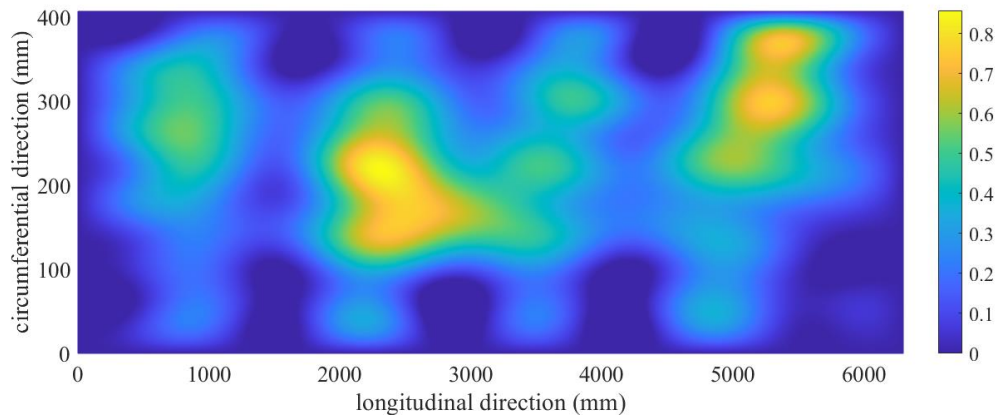
The following equation is found to fit the empirical value of f_c for pipe segment #1 reasonably well:

$$f_c(x, y) = \max\left\{0, \sum_{i=1}^{10} \sum_{j=1}^{10} c_{ij} \sin\left(\frac{i\pi x}{L}\right) \sin\left(\frac{j\pi y}{W}\right)\right\} \quad (\text{C.1})$$

where c_{ij} ($i, j = 1, 2, \dots, 10$) are given in Table C.1. The values of f_c obtained from Eq. (C.1) for pipe segment #1 are shown in Fig. C.1.

Table C.1 Values of c_{ij} in Eq. (C.1)

$c_{ij} (\times 10^{-3})$	j										
		1	2	3	4	5	6	7	8	9	10
i	1	505.8	17.8	97.2	-84.9	84.3	99.4	43.5	86.4	-70.1	-90.5
	2	-71.2	39.7	-108.8	4.1	-70.1	17.0	-23.9	-30.0	71.0	-45.9
	3	-34.0	-44.1	75.9	11.6	27.7	-20.9	-13.9	42.7	-46.0	-18.5
	4	-20.2	6.4	30.5	16.8	-34.1	9.9	-3.4	14.6	28.8	-41.7
	5	6.8	-20.9	28.1	-18.5	19.9	-4.9	6.8	6.8	-14.3	-22.2
	6	21.8	12.0	-17.5	13.2	-2.1	14.0	7.4	-5.3	21.1	-0.2
	7	29.8	5.5	10.1	-15.5	-0.6	-1.4	-0.7	3.8	-9.2	-5.5
	8	18.2	9.3	-11.6	6.0	-8.8	10.9	-2.7	11.6	12.5	-20.8
	9	18.6	-7.9	9.5	-18.1	1.8	-6.7	7.1	6.1	-16.9	0.2
	10	-24.4	11.3	-5.4	9.0	11.5	15.2	-0.8	1.4	9.6	0.5

**Figure C.1 Values of f_c for pipe segment #1 calculated using Eq. (C.1)**

Curriculum Vitae

Name: Ji Bao

Post-secondary Education and Degrees: Jiangsu University of Science and Technology
Zhenjiang, Jiangsu, China
2008-2012 B.Eng.

Shanghai Maritime University
Shanghai, China
2012-2014 M.Eng

Delft University of Technology
Delft, South Holland, Netherlands
2014-2016 M.ESc

Western University
London, Ontario, Canada
2017-2020 Ph.D.

Honours and Awards: Western Graduate Research Scholarship
2017-2020

Related Work Experience Structural Engineer and Stress Analyst
Trifleet Leasing (The Netherlands) B.V.
2015-2016

Teaching Assistant and Research Assistant
Western University
2017-2020

Publications:

Articles in refereed journals:

[1] **Bao. J.**, and Zhou. W. 2020. Influence of the corrosion anomaly class on predictive accuracy of burst capacity models for corroded pipelines. *International Journal of Geosynthetics and Ground Engineering*. 6(45).

[2] Zhou. W. and **Bao. J.** 2020. Uncertainty Quantification of Wall Thickness of Onshore Gas Transmission Pipelines. *Canadian Journal of Civil Engineering*. (accepted on October 3, 2020).

Conferences papers:

- [1] **Bao. J.**, Zhang. S., Zhou. W. and Zhang. S. 2018. Evaluation of burst pressure of corroded pipe segments using three-dimensional finite element analysis. In: Proceedings of the 2018 International Pipeline Conference. IPC2018. Sept. 24 - 28. Calgary, Canada.